2012

Spin Pumping in Lateral Double Quantum Dot Systems

Sabine S. Pelton
University of Central Florida

SPIN PUMPING
IN
LATERAL DOUBLE QUANTUM DOT SYSTEMS

by

SABINE S. PELTON
B.S. University of Texas at Arlington, 2007

A thesis submitted in partial fulfillment of the requirements
for the degree of Master of Science
in the Department of Physics
in the College of Sciences
at the University of Central Florida
Orlando, Florida

Spring Term
2012

ABSTRACT

Electron transport in single lateral quantum dot (QD) and parallel lateral double quantum dot (DQD) systems is modeled using semiclassical rate equations. The Zeeman effect, in conjunction with resonant tunneling, is used to select the spin of electrons involved in transport. We show adiabatic spin pumping by periodic variation of the systems' confining parameters, namely the quantum point contacts (QPCs) dictating the boundaries of the dots, and the gate voltage applied to each dot. The limitations of adiabatic spin pumping are subsequently examined by counting the average spin pumped per cycle when frequency and interdot capacitance are adjusted.

Hi Mom.

ACKNOWLEDGMENTS

Finally, none of this would be possible without the infinite patience and support of my adviser, Dr. Eduardo Mucciolo. You were always willing to help me understand the physics without being patronizing, and always had useful advice for dealing with the machinery of grad school, even though sometimes that advice fell on deaf ears. When I called you from the top of a mountain in Connecticut, you were not only kind, but took care of the business end of finishing this work while I finished hiking. I'm still not sure why you continue to be supportive, and I may never really get it- but whatever your motivations, you have my sincere gratitude and respect. *Best. Adviser. Ever.*

TABLE OF CONTENTS

LIST OF FIGURES

LIST OF TABLES

CHAPTER ONE:
INTRODUCTION

1.1   Spintronics

Our lives are inseparably entwined with semiconductor technology. We stay in touch with friends and loved ones using cell phones, submit important documents via the internet, store our most precious memories electronically, and owe a great deal of our scientific understanding of the world around us to numerical computation performed on clusters. Recognizing the phenomenal utility of consumer electronics, we strive to find faster, smaller, hardier devices with more memory and raw computational ability. So predictable is the thirst for better technology that Moore's law - that the number of transistors on an integrated circuit will double every two years - has held since its proposal in 1965 [1]. However, the size of each transistor cannot continue to shrink indefinitely, nor can the number of transistors per chip increase without reservation. One encounters the definite size limitation imposed by the atom - after all, we cannot build with subatomic particles! - even without considering the decidedly non-classical behavior of electrons already encountered even at sizes just a few orders of magnitude larger than a single atom. Furthermore, one cannot simply pack transistors closer together without considering thermodynamics. To push electrons around inside a device, a potential is applied, resulting in some unavoidable joule heating. This becomes an issue when considering the signal pickup of a transistor can be muddied by thermal broadening, leading to reduced computational ability; above a certain transistor density, it is entirely conceivable that the device simply melt and not perform any computation at all.

The present generation of consumer electronics owes its impressive storage capacity and computational ability to the relatively new field of spintronics. As opposed to traditional devices, which operate solely on charge current, spintronic devices also incorporate electron spin, leading to reduced power requirements for equivalent operations in traditional devices. Readily available devices use spin polarized current, generated by exploiting tunneling magnetoresistance (TMR) (a variation on giant magnetoresistance, or GMR). Other methods for generating spin-polarized current include various types of electron injection and using spin-orbit coupling effects, such as the Rashba effect. [1]

Spin polarized current has certainly allowed devices to shrink and use less power, but in the end, polarized current is still charge current. The same limitations apply as for purely charge based devices. However, using a *pure* spin current- that is, a current which does involve moving charge, just the transportation of spin- would at the very least sidestep some of the thermodynamic issues tied to miniaturization. As an added benefit, electron spin itself makes a very good information carrier, and thus has been suggested as a natural qubit. Naturally, the biggest obstacles between us and purely spin based devices lie in generating a pure spin current and in detecting a pure spin current.

1.1.1 Pure Spin Current

Several methods for generating spin current have been investigated, both theoretically and experimentally. Some take advantage of the material properties the system, hinging on spin-orbit interactions to scatter certain spins more than others [9, 10, 11, 12, 13]; some employ external oscillating fields [14, 15]. A substantial number of schemes follow the work of Thouless [16] by using periodic variation of system parameters to pump electrons through low-dimensional structures (e.g., 1D quantum wires and 0D quantum dots) [17, 18, 19, 20]; spin pumping is achieved when spin degeneracy is broken, usually

---

[1]While the generation of spin polarized current is both useful and interesting, it lies outside the scope of this work. We refer the interested reader to any of a number of review of spintronics, for instance, references [2, 3, 4], or papers directly addressing the systems, such as [5, 6, 7, 8].

with the application of an external field [21, 22, 23, 24, 25, 26, 27, 28]. There are also those which rely on interactions with polarized photons, such as in [29].

The difficulty in detecting spin current lies in the inaccessible geometry of the devices and the the lack of any method for *directly* measuring spin current. Electron injection, using ferromagnetic leads, converts the accumulation of spin at the lead boundary into a voltage signal [30], though coupling ferromagnetic leads and semiconductors presents some some challenges [6, 31]. The spin Hall effect [32] has also proven to be useful in generating spin current [33], with the inverse spin Hall effect allowing spin current to be converted to charge current [34] There are certainly ongoing debates about the best way to even define a spin current [35, 36], as measurement at a boundary does not reflect overall conditions in bulk, whereas detection techniques use spin accumulation and diffusion to determine the magnitude of spin transport. For a more thorough (but still general) review of the mechanisms delineated here, see Ref. [37].

1.2   Outline

In this Thesis, we consider electron transport in single and double lateral quantum dot systems in the sequential tunneling regime. We develop a pumping scheme in which tunneling barriers and gate voltages are varied adiabatically to pump charge from one reservoir to another at zero bias. In the presence of a static in-plane magnetic field, spin degeneracy is lifted and it becomes possible to select the spin of the electron pumped; we attempt to determine a scheme which pumps zero net charge but one $\hbar$ between reservoirs per cycle.

Chapter 1.2 contains a more complete physical description of the DQD system in question, followed by an electrostatic treatment of charging energy, and a review of the Coulomb blockade and Zeeman effect. The phase diagram is introduced as a useful tool for qualitative analysis of the system.

In Chapter 2.5,we provide a quantum mechanical description of the complete dot-reservoir system in the Constant Interaction (CI) model (that is, neglecting exchange interactions). The Interaction Hamiltonian may be used to derive the semiclassical rate equations as well as an expression for electron transition rates. The rate equations are then used to find expressions for current and conductance for the system, and applied to the toy example of one dot with one available energy level for clarity.

In Chapter 3.5, the results of simulations based on the rate equations are presented for one dot and two dot systems, both with and without an applied magnetic field. Occupation probabilities are plotted in the phase space of V_{g1} and V_{g2} for equilibrium and non-equilibrium conditions; in equilibrium it is shown that configurations with equivalent charge are equally likely, hence the rate equations do not completely determine the state of the system. This degeneracy is briefly explored in the context of "switching" behavior. For the DQD system, the total charge pumped per cycle is calculated for a variety of gate voltage and level width parameterizations and pumping frequencies. When considering an applied magnetic field, we also calculate the average spin transferred between reservoirs for each parameterization and frequency.

CHAPTER TWO:
BACKGROUND THEORY

In this Chapter, we provide a brief overview of the construction of a lateral quantum dot, followed by an electrostatic treatment of charging energy. The Coulomb blockade is then discussed in relation to electron transport through a quantum dot system, and finally, the Zeeman effect and its proposed role in spin selection processes is presented.

2.1   Lateral Quantum Dot Construction

As a general description, quantum dots spatially confine electrons to zero dimensions [38]. Here, "zero dimensional" is not meant to be taken in a strict mathematical sense; rather, regions on the order of an electron's Fermi wavelength

$$\lambda_F = \frac{h}{p_F} \tag{2.1}$$

are sufficiently small to allow for quantization of energy levels inside the confining potential, and may be considered low dimensional. This may be physically achieved by first creating a 2DEG at the interface of an AlGaAs-GaAs heterojunction, then strategically depositing conducting strips on the substrate surface. Applying voltage to these contacts acts to create a potential barrier in the 2DEG directly underneath, so that electrons are unable to move freely across the effective barriers. A potential well may be formed by isolating a small region of the 2DEG with such leads. Figure 2.1 shows an SEM image

of two dots in series, and a schematic representation of a parallel double quantum dot structure is given in Fig. 2.2.
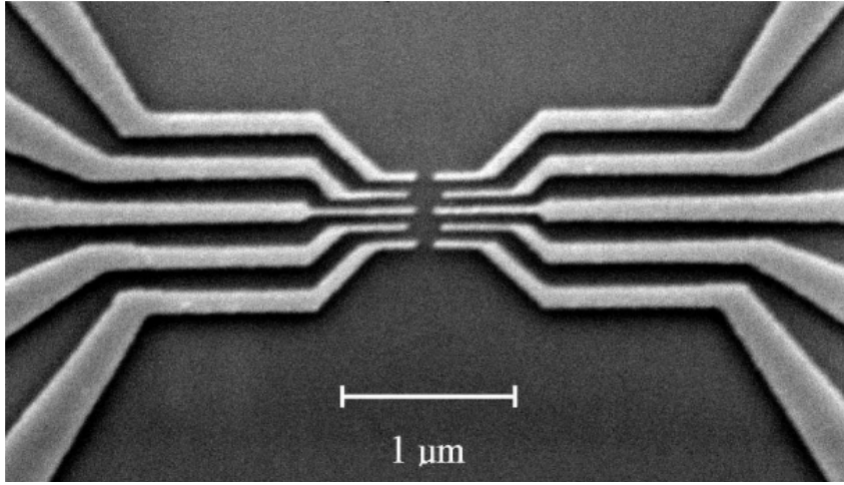
SEM image of two quantum dots in series. Image courtesy of Albert Chang, Duke University.

Figure 2.1: SEM Image of Two Dots in Series

The unconfined 2DEG surrounding the dot, referred to as the "reservoir", contains electron states populated according to

$$f(\varepsilon) = \frac{1}{e^{(\varepsilon-\mu)/k_B T} + 1}. \tag{2.2}$$

The magnitude of the dot-reservoir coupling Γ may be decreased by decreasing the voltage on the outermost conducting strips, pinching the electrons' path from reservoir to dot. To increase coupling, one increases the applied voltage. A gate voltage (V_g) is applied by means of an additional contact directly over the isolated dot area. V_g uniformly adjusts the chemical potential of the dot, thereby raising or lowering its discrete energy levels without affecting level spacing. A charge current can be generated in the presence of a source-drain bias solely by manipulation of V_g; in the absence of a bias it will also become necessary to control the coupling of the dot to each reservoir (see Section 2.3).

2.2   Charging Energy

The total electrostatic energy for a quantum dot system may be found using electrostatics, starting from

$$U = \frac{1}{2}\vec{Q}\mathbf{C}^{-1}\vec{Q},\tag{2.3}$$

in which the system is treated as N conductors with intercapacitances C_{jk} and stored charge Q_j. The schematic representation of a parallel DQD configuration in Fig. 2.2 labels the nodes between dot 1 and dot 2, dot 1(2) and left(right) reservoir, and dot 1(2) and gate voltage source with the appropriate capacitance.

Consider node j, which has total charge Q_j, total capacitance C_{jj}, and electrostatic potential V_j:

$$
\begin{aligned}
Q_j &= \sum_{k=1}^{N} q_{jk} \\
&= \sum_{k=1}^{N} c_{jk}(v_j - v_k).
\end{aligned}
\tag{2.4}
$$

For the entire system, charge follows from

$$\vec{Q} = \mathbf{C}\vec{V}.\tag{2.5}$$

A more thorough derivation may be found in Appendix A. In the literature, one frequently encounters double quantum dots (DQDs) in series configurations [39, 40, 41, 42, 43]. The total energy expressions for parallel and series configurations are nearly identical, but we make several critical distinctions:

- The coupling between dots in series is not just capacitive. It also carries a physical conduction channel which allows tunneling between dots.

  In the parallel configuration considered here, C_m does not represent a real channel, but rather takes into account the electrostatic distortion of dot 1(2) due to the
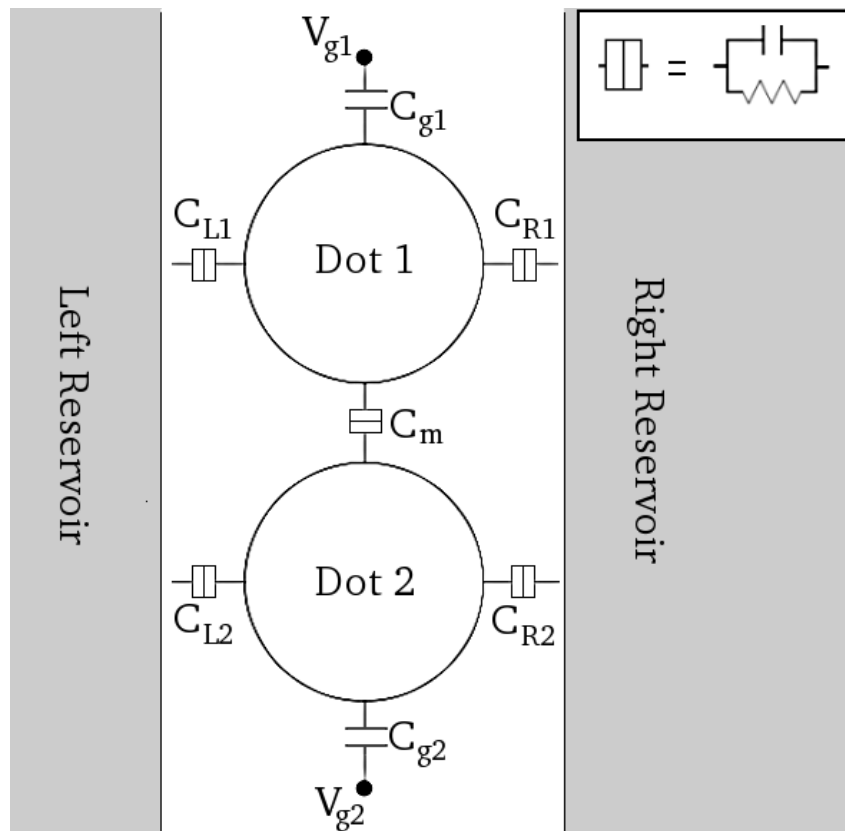
Schematic diagram of quantum dots in parallel.

Figure 2.2: Parallel Double Quantum Dot Schematic

addition or removal of an electron from dot 2(1). We have assumed that dots 1 and 2 are well shielded from each other so that the capacitance C_m is very small. There are several studies addressing physically coupled parallel DQDs, however. These provide interesting insights into cotunneling, Kondo phenomena, and "switching" behavior. See, for example, [44, 45]).

- DQDs in series are often subjected to a source-drain bias to generate current. That is, left and right reservoirs are held at different potentials so that transport is preferred in one direction only.

  Since the goal of this investigation is to create spin current with zero net charge current, the chemical potential of the left and right reservoirs are set equal to each other. For symmetric dots in equilibrium, this allows electrons to move in either direction with equal probability.

- For a parallel configuration, both dots are coupled to both reservoirs, creating two additional capacitances in the expression for charging energy. For the sake of simplicity, the system is assumed to be symmetric, so that $C_{L,1} = C_{R,1} = C_{R,2} = C_{L,2}$ and $C_{g1} = C_{g2} = C_g$. In the case of the gate voltage-dot capacitances $C_{g1(2)}$, the potential V_g and the charge on the node are ideally so large that adding or removing an electron from the dot does not change C_g appreciably.

Using Eqs. (2.3) to (2.5) and the results of Appendix A, the general expression for the total electrostatic energy of the parallel DQD may be obtained:

$$
\begin{aligned}
U(N_1, N_2) &= \frac{1}{2}N_1^2 E_{c1} + \frac{1}{2}N_2^2 E_{c2} + N_1 N_2 E_{cm}^2 \\
&\quad - \frac{1}{|e|}\left[C_{g1}V_{g1}(N_1 E_{c1} + N_2 E_{cm}) + C_{g2}V_{g2}(N_1 E_{cm} + N_2 E_{c2})\right] \\
&\quad + f(V_{g1}, V_{g2}),
\end{aligned}
\tag{2.6}
$$

where $f(V_{g1}, V_{g2})$ represents "background" charges and potentials,

$$f(V_{g1}, V_{g2}) = \frac{1}{|e|^2} \left[\frac{1}{2} C_{g1}^2 V_{g1}^2 E_{c1} + \frac{1}{2} C_{g2}^2 V_{g2}^2 E_{c2} + C_{g1} V_{g1} C_{g2} V_{g2} E_{cm} \right]. \qquad (2.7)$$

The charging (or addition) energy $E_{c1(2)}$ is the energy required to add an electron to the dot,

$$E_{c1(2)} = e^2 \frac{C_{1(2)}}{C_1 C_2 - C_m^2}, \qquad (2.8)$$

where $C_{1(2)}$ represents the total capacitance of dot 1(2), $C_{1(2)} = C_{L1(2)} + C_{R1(2)} + C_{g1(2)} + C_m$. Charging energy is very similar in definition to the electrochemical potential of the dot, which is the energy required to add an electron to dot 1(2) while taking into account the electrons on dot 2(1). This amounts to the difference in electrostatic energy when adding or removing an electron from the system,

$$\mu_1(N_1, N_2) = U(N_1 + 1, N_2) - U(N_1, N_2) \qquad (2.9)$$

$$\mu_2(N_1, N_2) = U(N_1, N_2 + 1) - U(N_1, N_2). \qquad (2.10)$$

Equation (2.8) may be obtained by finding the change in electrochemical potential when adding an electron to dot 1(2),

$$E_{c1} = \mu_1(N_1 + 1, N_2) - \mu_1(N_1, N_2) \qquad (2.11)$$

$$E_{c2} = \mu_2(N_1, N_2 + 1) - \mu_2(N_1, N_2). \qquad (2.12)$$

Finally, E_{cm} is the electrostatic coupling energy of the dots,

$$E_{cm} = e^2 \frac{C_m}{C_1 C_2 - C_m^2}. \qquad (2.13)$$

In parallel DQDs, E_{cm} represents the magnitude of the electrostatic distortion of dot 1(2) due to electrons on dot 2(1). Quantization may be accounted for by including discrete energy levels in the expression for the electrochemical potential of the dots. For example,

the electrochemical potential for adding an electron to level n in the dot is

$$\mu_{i,n} = \mu_i + \varepsilon_n. \tag{2.14}$$

Hence the expression for charging energy, Eq. (2.8), is adjusted by the amount $\Delta\varepsilon$, which is the level spacing of the dot.

$$
\begin{aligned}
E_{c1} &= \mu_{1,m}(N_1 + 1, N_2) - \mu_{1,n}(N_1, N_2) \\
&= \mu_1(N_1 + 1, N_2) - \mu_1(N_1, N_2) + \varepsilon_m - \varepsilon_n \\
&= E_{c1,class} + \Delta\varepsilon. \tag{2.15}
\end{aligned}
$$

It is reasonable to treat dots as no more than tiny systems of conductors, as is shown here, providing that the system remains in a regime which may be characterized by the Constant Interaction (CI) model [46]:

- In the CI model, electron interactions are characterized by a constant capacitance C, which is the sum of all of the system capacitances. Electron interactions are limited to charging, although in the case of very small dots, exchange energy may be taken into account by adding a term to describe spontaneous spin polarization [47]. Tunneling in and out of the dot is typically assumed sequential and incoherent.

- Interactions which cannot be adequately described as electrostatic charging, particularly in the presence of coherent tunneling, are not included in the CI model. Cotunneling, correlation effects within the QD, the Kondo effect etc. can be minimized by allowing only small magnetic fields, negligibly small reservoir bias, and weak dot-reservoir coupling. In addition, these effects tend to be more significant for very small QDs.

Because the dots' physical dimensions are only large enough to accommodate a few electrons, N_1 and N_2 must be small integer numbers. Hence, the discrete nature of charging becomes very apparent and important.

11

2.3 Coulomb Blockade

Electron transport between dot and reservoir is naturally suppressed. This is in part due to the confining potential gates, but even more importantly, by the mismatch between the chemical potentials of the reservoir and the dot. To maximize transmission, the Fermi level of the reservoir must equal change in the dot chemical potential due to the addition of an electron. A change in the dot's chemical potential can be achieved by adjusting V_g. For instance, to increase conductance, V_g is adjusted to suppress the dot's chemical potential beyond the requisite addition energy for the $(N + 1)$th electron, effectively aligning the available $(n + 1)$th dot energy level with the reservoir's Fermi level. At this point there is no charging energy penalty for an electron to move between dot and reservoir, and the conductance peaks [48]. This conduction-suppression behavior is known as Coulomb blockade.

The voltages for which the peaks occur are found by setting Eq. (2.6) equal to itself for N and $N + 1$ electrons. As an example, consider a one-dot system:

$$
\begin{aligned}
U(N) &= U(N+1) \\
eNV_g + \frac{e^2 N^2}{2C} &= e(N+1)V_g + \frac{e^2(N+1)^2}{2C}.
\end{aligned}
\tag{2.16}
$$

Rearranging Eq. (2.16) gives

$$
V_g = \frac{-e}{C}(N + 1/2).
\tag{2.17}
$$

Coulomb blockade oscillations occur any time the charging energy of a system is greater than its thermal energy; that is, $U(N_1, N_2, \ldots, N_n) >> k_B T$ [38, 49]. However, conductance peaks are most readily observed when certain conditions are met:

- Thermal fluctuations must be smaller than both charging energy and level spacing, $k_B T < \Delta\varepsilon,\ E_c$.

- Dots are weakly coupled to the reservoirs, so that electrons are well confined to the dot, $\Gamma \ll \Delta\varepsilon$. When dot-reservoir coupling is large, conductance peaks may become so broad as to be indistinguishable; in addition, other phenomena become important when considering electron transport, especially in the presence of a magnetic field [50, 51, 52].

The last condition is particularly important since delocalization contributes to the formation of coherent and correlated electronic states in what is known as the Kondo effect [53, 54, 55]. It should be noted that the CI model is invalid when describing situations where correlations develop, so that charging energy effects are insufficient to describe electron transport. More specifically, correlation effects appear when T approaches the Kondo temperature [54],

$$ T_K = \frac{\sqrt{\Gamma U}}{2} \exp\left[\frac{\pi\varepsilon_0(\varepsilon_0 + U)}{\Gamma U}\right]. \tag{2.18} $$

In this investigation we will assume that $T \gg T_K$ by choosing Γ sufficiently small and T sufficiently large. This strategy can be also used in real experiments in order to avoid strong correlation effects.

When the Coulomb blockade resonant condition is met, the charging energy cost of adding or removing an electron from the dot is exactly compensated by an external gate voltage, and the dot and reservoir electrochemical potentials become aligned. As a result, the transmission probability approaches a maximum, allowing electrons to move almost freely across the dot, except at the tunneling contacts. In this case, the charging energy can be discarded and a single-level approximation can be used. The transmission probability may be found by treating the dot as a double barrier system and using a standard single-particle scattering matrix formulation [56, 49]. Conductance depends on partial level widths Γ_1 and Γ_2, which in turn depend on the density of states in the reservoirs and the tunneling amplitude t_j of the "incident" or "outgoing" electron, as

given by the Fermi golden rule

$$\Gamma_j = 2\pi \, \nu \, |t_j|^2. \tag{2.19}$$

The amplitude t_j is difficult to estimate without a detailed knowledge of the potential barriers. In addition, since t_j can be tuned at will in most devices, one adopts Γ_1 and Γ_2 as variable phenomenological parameters. For most setups, they vary in the range of tens to hundreds of μV.

From the 2DEG density, one can estimate the number of electrons a dot can typically hold: For a small dot of 100 nm in diameter, a brief calculation yields $N \sim 10$ when the 2DEG density is 10^{11} cm^{-2}.

2.3.1   Stability Diagrams

A number of DQD system properties may be visualized with the use of stability diagrams in which the equilibrium charge states are shown with respect to the gate voltages.

In order to do so, let the pair (N_1, N_2) represent a state with N_1 electrons in dot 1 and N_2 electrons in dot 2. For instance, in a two-dot system, where each dot has only one single-particle energy eigenstate, $N_{1(2)}$ can only take the values 0 or 1. Figure 2.3 shows the four possible system configurations in this case: $(0,0)$, in which both dots are empty; $(1,0)$, in which dot 1 contains 1 electron and dot 2 is empty; $(0,1)$, where dot 1 is empty and dot 2 has one electron; and $(1,1)$, in which both dots contain one electron.
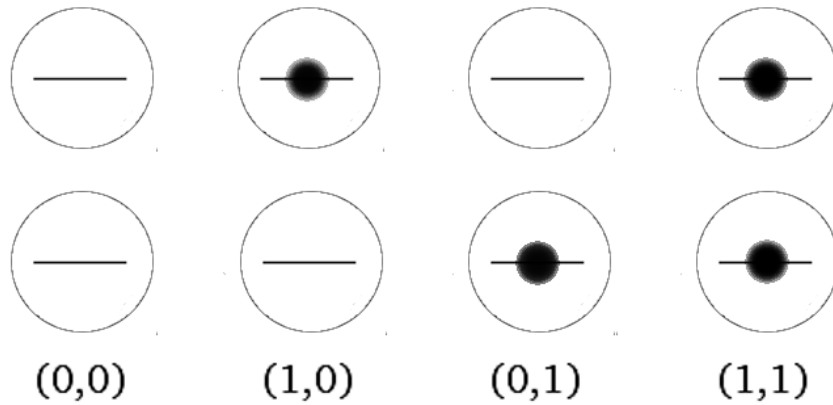
The possible configurations of a two-dot system with one available level each.

Figure 2.3: Possible Configurations for a Two-Dot System

For a given set of gate voltages, the equilibrium charge state may be found analytically by minimizing Eq. (2.6) with respect to the electron numbers. To generate a stability diagram, the equilibrium charge state is found for a range of gate voltages, then plotted in the V_{g1}-V_{g2} phase space, as shown in Figs. 2.4 to 2.6.
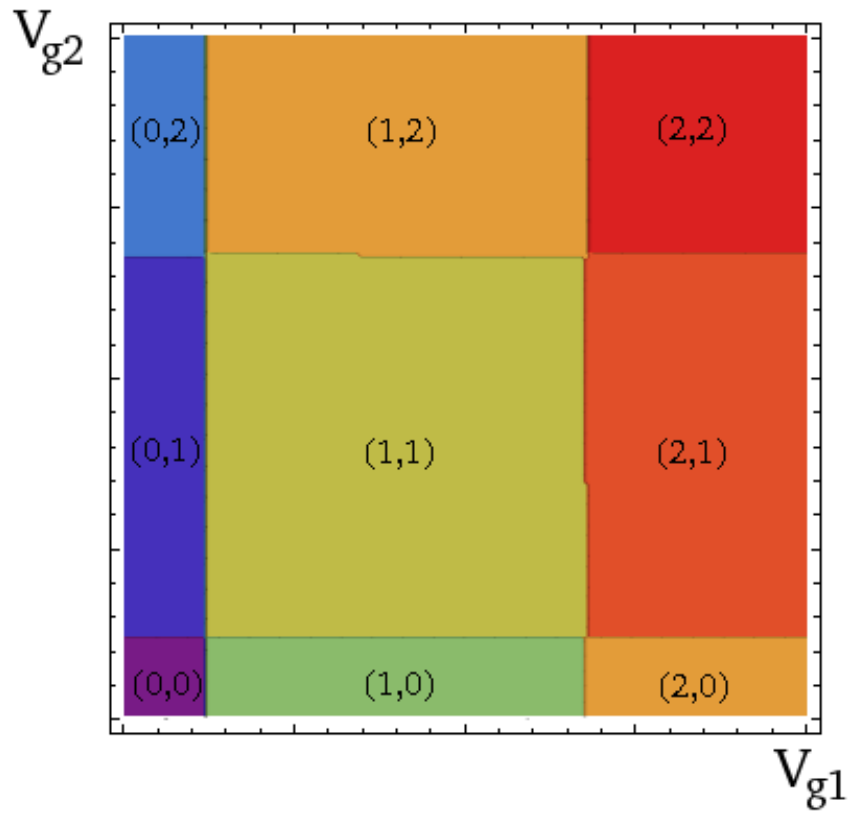
Stability diagram for a DQD system showing up to two electrons per dot. When C_m is very small, the dots behave independently. Notice the four-fold degenerate corners.

Figure 2.4: Stability Diagram for a DQD when $C_m = 0$
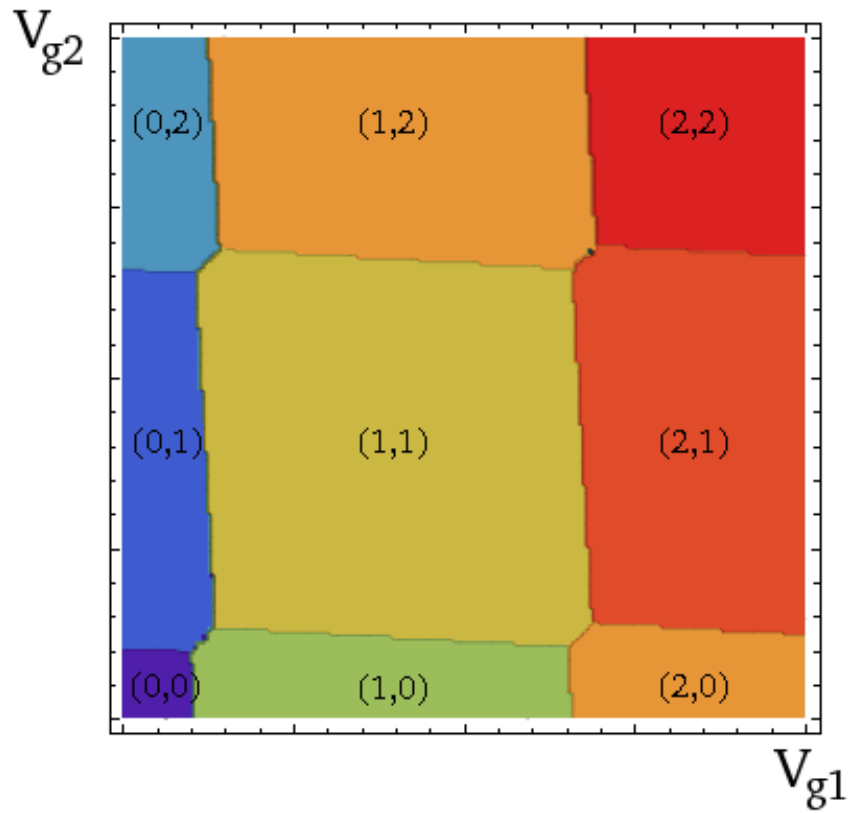
Small but non-negligible interdot coupling, $0 < C_m/C < 1$, causes the regions to distort into hexagons. The distance separating the triple points where three regions meet is E_{cm} and therefore increases with C_m.

Figure 2.5: Stability Diagram for a DQD when $C_m = 0.01C_g$
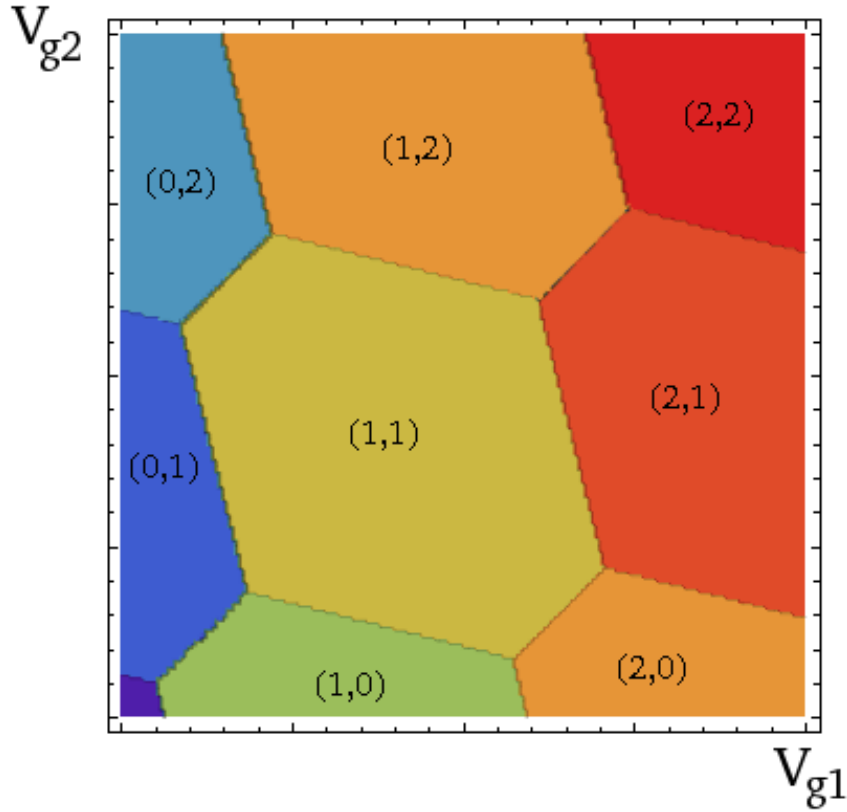
When the interdot coupling becomes very large, $C_m/C \simeq 1$, the regions become maximally distorted as E_c approaches ΔE.

Figure 2.6: Stability Diagram for a DQD when $C_m = 0.1C_g$

The regions become distorted for nonzero interdot coupling, going from rhombic to hexagonal, and earning the stability diagrams the alternate title of "honeycomb diagrams".

For dots in series, conductance resonances occur at triple points in the diagram [39], i.e. an electron may traverse two or more dots in series without penalty. Dots in parallel do not have this constraint, since each dot is connected to each reservoir and is not dependent on the other to provide an available channel for electrons. In this case, conductance peaks occur at all cell boundaries, *except* those between equal net charge regions (for example, (1,0) and (0,1)). See Fig. 2.7.
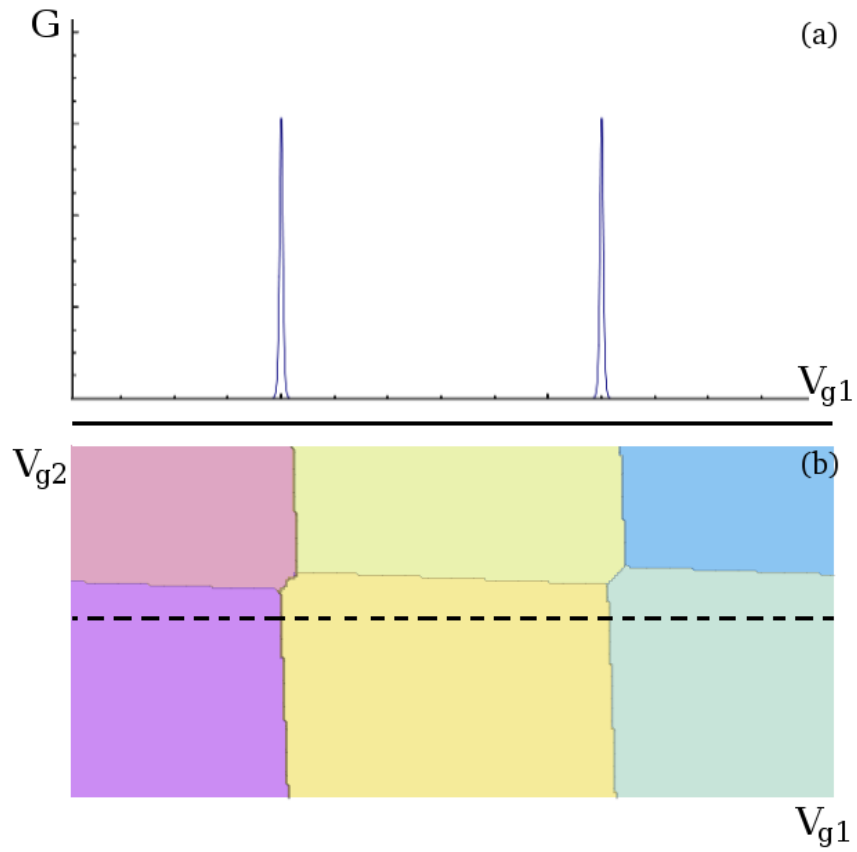
Conductance peaks occur at the boundaries of equilibrium charge regions. The path traced in (a) corresponds to the conductance line in (b).

Figure 2.7: Position of Conductance Peaks in Phase Space
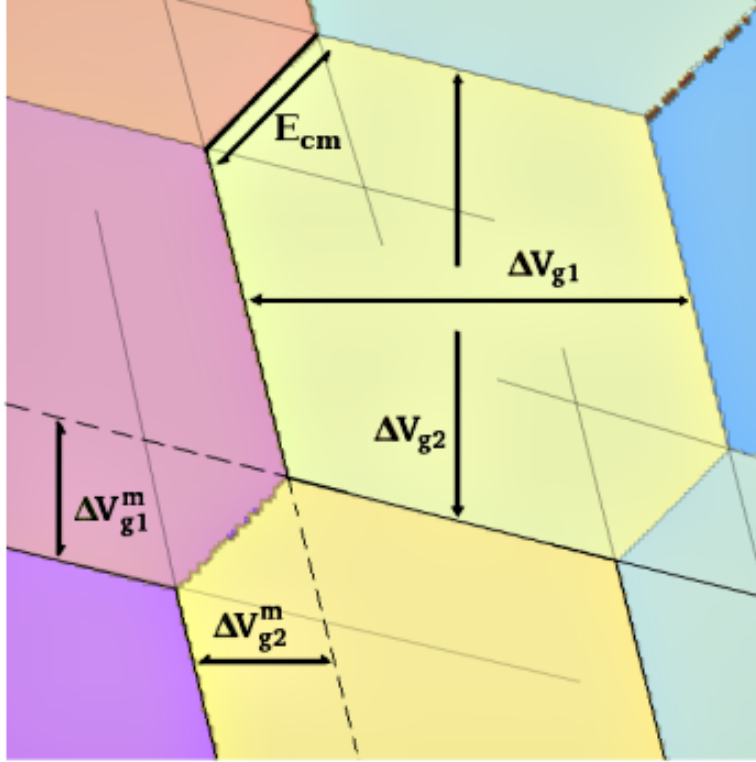
The height of the equilibrium charge region may be used to find the distance between conductance peaks in dot 2 and the width gives the distance between conductance peaks in dot 1. The separation distance of the triple points is conveniently given by the electrostatic coupling energy E_{cm}, which is in turn the shift in conductance peak position due to interdot coupling.

Figure 2.8: Meaning of the Dimensions of Stability Diagram Cells

Some additional useful features of the stability diagram are illustrated in Fig. 2.8. For nonzero interdot coupling, the corner points (as in Fig. 2.4) of an uncoupled system become edges of length E_{cm}, where the width and height of the line with respect to $V_{g1(2)}$ corresponds to a shift in the conductance peak due to interdot coupling ($\Delta V^m_{g1(2)}$). The total width and height of the cell still correspond to the spacing between conductance peaks with respect to V_{g1} and V_{g2}:

$$\Delta V^m_g = \Delta V_g \frac{C_m}{C} = |e| \frac{C_m}{C_g C} \tag{2.20}$$

$$\Delta V_g = \frac{|e|}{Cg} \tag{2.21}$$

2.4 Zeeman Effect

A symmetric two-dimensional parabolic potential well provides a very simple, commonly used representation of small quantum dots (see, for example, [57]). Solutions to this model have degenerate energy levels and an electron orbital structure. In symmetric dots (generally speaking, vertical quantum dots), electrons of opposite spin will share the same energy level unless the exchange energy is larger than the level spacing, in which case consecutive electrons will occupy different orbital levels maintaining the same spin polarization, similarly to Hund's rules in atomic physics [58]. Level filling in (less symmetric) lateral dots is not spin independent, but does follow some spin-dependent filling scheme [59]. Any existing spin degeneracy can be lifted via an external magnetic field through the Zeeman effect. The spin-degenerate energy levels will split according to the familiar formula

$$\Delta E_Z = |g|\mu_B B, \tag{2.22}$$

where the bare Landé gyromagnetic (g) factor for GaAs is $g = -0.44$ [40]. In large, high-density dots, it is possible to enhance the spin-orbit coupling by compressing transversally the 2DEG with a strong in-plane magnetic field [60]. This effect, combined with mesoscopic fluctuations in the dot, can renormalize the g factor. Since our focus is on small dots and low densities, we will neglect this effect and adopt the bare value for g.

In addition, to keep our results applicable to the real world we must impose further constraints on the system:

- If we want to use a fairly weak field, we must use a dot with several if not tens of electrons. Very small dots exhibit a richer energy spectrum: level spacing fluctuates greatly and tends to bunches up in a shell structure, so that the spacing varies substantially from $N = 2$ to $N = 3$, from $N = 6$ to $N = 7$, etc [58]. In addition, correlation effects are more pronounced.

- Large perpendicular fields give rise to level crossing and eventually to Landau levels, so that the chemical potential of the dot "zigzags" [52]. Correlation effects become important in this case as well, making the CI model invalid.

Thus, we will assume that the dot holds in the range of tens of electrons and that the Zeeman field is applied *parallel* to the 2DEG, to avoid any coupling to orbital degrees of freedom.

2.5   Chapter Summary

This chapter reviewed the construction and basic physical principles of lateral quantum dots.

A 2DEG is created using GaAs heterojunctions. Strips of conducting material are deposited on top of the structure in a specific pattern. Voltage is applied to the strips, creating a potential barrier in the 2DEG directly underneath, forming the "dot".

The CI model adequately describes electron transport across a quantum dot, provided that there is small or no reservoir bias, dot-reservoir coupling is small, any applied magnetic field is weak, and the temperature is sufficiently larger than the Kondo temperature. Expressions for charging, addition, and total electrostatic energy were found for systems meeting these conditions. For cases when the level spacing in the dot is on the order of the charging energy, the expressions must be modified to account for quantization.

The Coulomb blockade was discussed as an important consequence of discretization in the dot, as well as the conditions for which conductance oscillations are most readily observed. Stability diagrams, which show equilibrium charge states in the gate voltage phase space, were introduced as a tool for visual inspection of the system.

Finally, the Zeeman effect was reviewed to address the issue of level filling and level degeneracy in quantum dots.

CHAPTER THREE:
THE RATE EQUATION METHOD

Chapter 2 described mostly classical, time-independent phenomena. This chapter will focus on dynamic behavior and the quantum mechanical description of the system. First, the Hamiltonian of the system will be discussed, breaking the total system into dot and reservoir subsystems, and defining an interaction Hamiltonian. In the limit of weak dot-reservoir coupling, the interaction term may be treated as a perturbation, allowing the calculation of electron transition rates using Fermi's golden rule. The time evolution of the state of the dot is then described probabilistically using rate equations. The notation is explained for clarity, and a one-dot, one-reservoir system illustrates the usefulness of the rate equations. Finally, expressions for current and conductance through a quantum dot are derived, then applied to the one-dot example.

3.1 The Hamiltonian

The entire DQD system may be divided into two basic subsystems, that of the dots and that of the reservoirs. Events in both subsystems consist of adding or removing electrons, so the Hamiltonian for each may be conveniently expressed in terms of creation and annihilation operators.

Recall that the reservoir is a 2DEG with a density of states ν. The energy of free electrons in a GaAs 2DEG is assumed spin independent and may be written as

$$\xi_k = \frac{\hbar^2 k^2}{2m^*},\qquad(3.1)$$

23

where k is linear momentum and m^* is effective band mass. The reservoir Hamiltonian can thus be written

$$H_R = \sum_{r=R,L} \sum_{\sigma=\uparrow,\downarrow} \sum_k \xi_k \, \hat{c}^\dagger_{r;k\sigma} \hat{c}_{r;k\sigma}. \tag{3.2}$$

Summation occurs over both reservoirs (denoted by reservoir index r), linear momentum k, and spin σ. Here, $\hat{c}^\dagger_{r;k\sigma}$ and $\hat{c}_{r;k\sigma}$ represent the creation and annihilation operators, respectively.

The Hamiltonian for the dots may be similarly expressed. For simplicity, electrons will be considered non-interacting particles inside a well with single-particle states $\{\psi_p\}$ associated to energies $\{\epsilon_p\}$. Electron-electron interaction is accounted for with the addition of the dot electrostatic energy U. For two identical dots,

$$H_D = \sum_{q=1,2} \sum_p \epsilon_p \, \hat{a}^\dagger_{q,p} \hat{a}_{q,p} + U(\hat{N}_1, \hat{N}_2), \tag{3.3}$$

where $\hat{N}_q = \sum_p \hat{a}^\dagger_{q,p} \hat{a}_{q,p}$ counts the electrons in dot q. This expression is very general, and allows the index p to account for both orbital and spin degrees of freedom.

The interaction Hamiltonian is expressed in the combined subspaces of the dots and the reservoirs,

$$H_I = \sum_{r=R,L} \sum_{q=1,2} \sum_{k,\sigma} \sum_p \mathrm{T}^{r,q}_{k,p} \left(\hat{c}^\dagger_{r;k\sigma} \hat{a}_{q,p} + \hat{a}^\dagger_{q,p} \hat{c}_{r;k,\sigma} \right). \tag{3.4}$$

To continue operating under the assumptions made in Chapter 2, it will be assumed that dot-reservoir coupling is very weak. Here, the magnitude of the interaction is governed by the parameter $\mathrm{T}^{r,q}_{k,p}$, which represents tunneling events' transmission matrix elements (refer to Section 2.3). In the present calculations, it will be assumed that the amplitude of these parameters is independent of k, σ, and p. This is a combination of the so-called wide-band approximation (a brief review of which was given in [61]), and the assumption that states ψ_p do not differ substantially in their overlap with the states in the reservoirs.

Finally, the full Hamiltonian is found by combining Eqs. (3.3), (3.3), and (3.4) to

obtain

$$H = H_D + H_R + H_I. \tag{3.5}$$

3.1.1 Transition Rates

It is possible to treat Eq. (3.4) as a perturbative term since the interaction Hamiltonian describes very weak dot-reservoir coupling. As such, transition rates for transport between the subsystems may be found using Fermi's golden rule,

$$\Gamma_{i \to f} = \frac{2\pi}{\hbar} |\langle f | \tilde{H}_I | i \rangle|^2 \delta(E_i - E_f). \tag{3.6}$$

In Eq. (3.6), we define the initial state $|i\rangle$ and the final state of the system as $|f\rangle$. The Hamiltonian used is the interaction Hamiltonian transformed into the interaction picture,

$$\tilde{H}_I = e^{\frac{it}{\hbar}(H_D + H_R)} H_I e^{\frac{-it}{\hbar}(H_D + H_R)} \tag{3.7}$$

Its effect is to translate one electron from(to) the reservoir to(from) the dot. In coherent transport, the transformation would also lead to a phase shift for transmitted electrons, but we are only considering incoherent, sequential transport. The matrix elements are evaluated by substituting in the Hamiltonians from Eqs.(3.3), (3.4), and (3.2):

$$\langle f | e^{\frac{it}{\hbar}(H_D + H_R)} H_I e^{\frac{-it}{\hbar}(H_D + H_R)} | i \rangle = T_{k,p}^{r,q} e^{\frac{it}{\hbar}(E_f - E_i)}. \tag{3.8}$$

From Eqs. (3.2) and (3.3), the initial and final energies are expressed in terms of the electrostatic energy, level energy ϵ_p, and reservoir energy ξ_k,

$$E_f - E_i = \epsilon_{p,f} - \epsilon_{p,i} + U(N_{1,f}, N_{2,f}) - U(N_{1,i}, N_{2,i}) + \xi_{k,f} - \xi_{k,i}. \tag{3.9}$$

In Eq. (3.9), we may assume that $\xi_{k,f}$ - $\xi_{k,i} \simeq 0$, and drop the last term. The expression is further simplified by referring to Eq. (2.15), and substituting in charging energy E_c for the remaining terms.

Finally, Eqs. (3.8) and (3.9) can be used in Eq. (3.6) to find

$$\Gamma_q^r(E) = \frac{2\pi}{\hbar} \sum_p |\mathrm{T}_{k,p}^{r,q}|^2 \delta(E - E_c). \tag{3.10}$$

In the wide band approximation, the transmission matrix elements $\mathrm{T}_{k,p}^{r,q}$ can be taken as independent of energy level.

3.2   Rate Equations

In equilibrium, the distribution of state probabilities for a QD system may be found using statistical mechanics. However, when describing system dynamics, it is necessary to use a non-equilibrium approach. Electron dynamics in quantum dot systems is commonly described using rate equations (otherwise known as master equations), which are valid provided that Γ_q^r is smaller than the relaxation rate of confined electrons $1/\tau_d$, dot level spacing, and interaction energy [62]. Here, τ_d is the average dwell time of an electron in the dot. The equations do not describe ballistic electron transport; rather, solutions are probability distributions of dot states.

In this Section, the general form of the rate equations is introduced. In order to dispel confusion over notation, and to provide a meaning for each term in the equation, this general form will then be used to find the set of equations for a single dot. A variety of simple dot configurations have been explored elsewhere in the literature (for example, [63, 64]), so it is not necessary to include a derivation here. However, in the interest of completeness, a density matrix based approach has been included as Appendix B.1.

The *static* nonequilibrium probability distribution of dot states can be found from

stationary solutions of the rate equations [48]:

$$
\begin{aligned}
\frac{\partial}{\partial t}P(\{n_i\}) = & -\sum_p P(\{n_i\})\delta_{n_p,0}[\Gamma_p^l f(E^{i,l}(N) - E_F) + \Gamma_p^r f(E^{i,r}(N) - E_F)] \\
& -\sum_p P(\{n_i\})\delta_{n_p,1}\{\Gamma_p^l[1 - f(E^{i,l}(N) - E_F)] + \Gamma_p^r[1 - f(E^{i,r}(N) - E_F)]\} \\
& +\sum_p P(\{(n_1, ..., n_{p-1}, 1, n_{p+1}, ...)\})\delta_{n_p,0} \\
& \times\{\Gamma_p^l[1 - f(E^{i,l}(N+1) - E_F)] + \Gamma_p^r[1 - f(E^{i,r}(N+1) - E_F)]\} \\
& +\sum_p P(\{(n_1, ..., n_{p-1}, 0, n_{p+1}, ...)\})\delta_{n_p,1} \\
& \times[\Gamma_p^l f(E^{i,l}(N-1) - E_F) + \Gamma_p^r f(E^{i,r}(N-1) - E_F)]. \quad\quad (3.11)
\end{aligned}
$$

Despite its obtuse notation, Eq. (3.11) can be understood heuristically by examining each term. On the left-hand side, we wish to find the rate of change of the probability of state $(\{n_i\})$. $(\{n_i\})$ translates readily to the notation of Sections 2.3.1 and 3.1: n_i is the number of electrons occupying energy level $i = 0, 1, ..., p$ in the dot, and may take values 0 or 1. On the right hand side, the rate is equal to the total probability that other states will evolve into $(\{n_i\})$, minus the total probability that $(\{n_i\})$ will evolve into a different state.

In its most basic formulation, the odds of such an evolution depends on the existence of an electron (or empty level) in the reservoir which satisfies the condition for resonant tunneling. The probability that state k in reservoir r, with energy ξ_k, is occupied is just the Fermi function,

$$
f(\xi_k) = \frac{1}{e^{\beta\xi_k} + 1}. \quad\quad (3.12)
$$

It follows then that the probability that level k is $unoccupied$ is $1 - f(\xi_k)$.

This must be multiplied by the probability that a state in the dot exists and is able to accept (donate) the electron in question. Hence, the evolution of the system into $P(\{n_i\})$ is given by the sum of the probabilities of all states $(\{(n_1, ..., n_{p-1}, 1, n_{p+1}, ...)\})\delta_{n_p,0}$ and $(\{(n_1, ..., n_{p-1}, 0, n_{p+1}, ...)\})\delta_{n_p,1}$ which can gain (lose) one electron to become $(\{n_i\})$, by

the probability that the appropriate electron (hole) is available in the reservoir, $f(\xi_k)$ $(1 - f(\xi_k))$.

3.2.1   Example: A Single Dot

We apply the general form of the rate equations, Eq. (3.11), to the system of one dot with two available energy levels and two reservoirs.
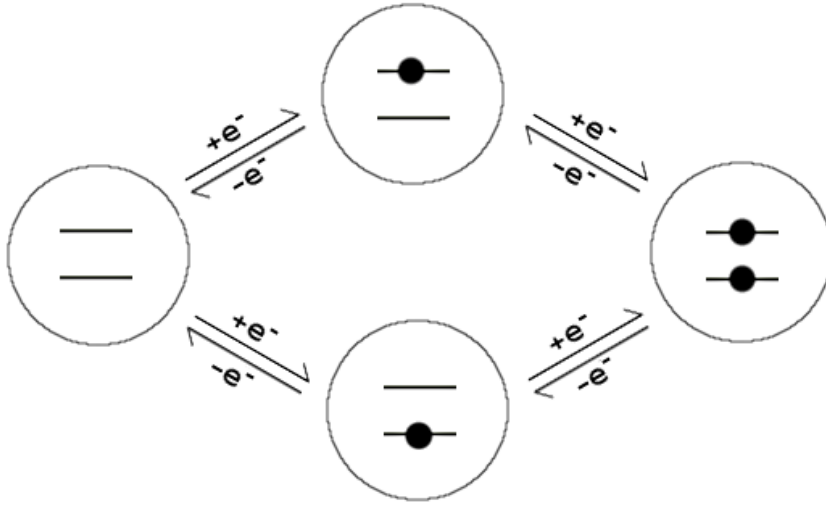
The possible transitions for a dot with two available energy levels. The arrows drawn between dot configurations represent events where an electron is added to (removed from) the dot.

Figure 3.1: Possible Transitions for a Single Dot System

Figure 3.1 shows the possible first-order transitions for a dot with two available energy levels. For instance, if the initial state is $(\{n_p\}) = (0,0)$, the dot may evolve into states $(1,0)$ or $(0,1)$. This knowledge, combined with Eq. (3.11), is used to write the time evolution of $P(0,0)$ as

$$
\begin{aligned}
\frac{\partial}{\partial t}P(0,0) &= -P(0,0)[\Gamma_1^l f(E^{i,l}(0) - E_F) + \Gamma_1^r f(E^{i,r}(0) - E_F) \\
&\quad + \Gamma_2^l f(E^{i,l}(0) - E_F) + \Gamma_2^r f(E^{i,r}(0) - E_F)] \\
&\quad + P(1,0)\{\Gamma_1^l[1 - f(E^{i,l}(1) - E_F)] + \Gamma_1^r[1 - f(E^{i,r}(1) - E_F)]\} \\
&\quad + P(0,1)\{\Gamma_2^l[1 - f(E^{i,l}(1) - E_F)] + \Gamma_2^r[1 - f(E^{i,r}(1) - E_F)]\}. (3.13)
\end{aligned}
$$

28

Equation (3.13) can be simplified since the wide band approximation (as mentioned in Section 3.1) allows Γ to be independent of k, p, and σ, so that $\Gamma_{2(1)}^{l(r)} = \Gamma_{1(2)}^{r(l)} = \Gamma$. Furthermore, the reservoirs are assumed to be symmetric, $f(E^{i,l}(N) - E_F) = f(E^{i,r}(N) - E_F)$. With these substitutions, Eq. (3.13) becomes

$$
\begin{aligned}
\frac{\partial}{\partial t} P(0,0) &= -P(0,0)\, 2\Gamma[f(E^{i,l}(0) - E_F) + f(E^{i,r}(0) - E_F) \\
&\quad + P(1,0)\, 2\Gamma[1 - f(E^{i,l}(1) - E_F)] \\
&\quad + P(0,1)\, 2\Gamma[1 - f(E^{i,l}(1) - E_F)].
\end{aligned}
\tag{3.14}
$$

To solve Eq. (3.14), equations for $P(1,0)$, $P(0,1)$, and $P(1,1)$ must also be found:

$$
\begin{aligned}
\frac{\partial}{\partial t} P(1,0) &= -P(1,0)\, 2\Gamma[f(E^{i}(1) - E_F) - (1 - f(E^{i}(1) - E_F)) \\
&\quad + P(0,0)\, 2\Gamma[f(E^{i}(0) - E_F)] \\
&\quad + P(1,1)\, 2\Gamma[1 - f(E^{i}(2) - E_F)].
\end{aligned}
\tag{3.15}
$$

$$
\begin{aligned}
\frac{\partial}{\partial t} P(0,1) &= -P(0,1)\, 2\Gamma[f(E^{i}(1) - E_F) - (1 - f(E^{i}(1) - E_F)) \\
&\quad + P(0,0)\, 2\Gamma[f(E^{i}(0) - E_F)] \\
&\quad + P(1,1)\, 2\Gamma[1 - f(E^{i}(2) - E_F)].
\end{aligned}
\tag{3.16}
$$

$$
\begin{aligned}
\frac{\partial}{\partial t} P(1,1) &= -P(1,1)\, 2\Gamma[2 - (f(E^{i}(2) - E_F) + f(E^{i}(2) - E_F)) \\
&\quad + P(1,0)\, 2\Gamma[f(E^{i}(1) - E_F)] \\
&\quad + P(0,1)\, 2\Gamma[f(E^{i}(1) - E_F)].
\end{aligned}
\tag{3.17}
$$

The evolution of the system is *almost* completely characterized with these four, coupled, homogeneous differential equations.

In Eqs. (3.14)-(3.17), $(\{n_i\})$ may be equivalently written as $(n_1, n_2, ..., n_p, ...)$. The value of n_p may be either 1 or 0, where 1 indicates that level p is occupied, and 0

indicates that level p is unoccupied. A system with multiple dots can be indexed as $(\{n_i\}) = (\{n_i\}_{q=1})(\{n_i\}_{q=2})...(\{n_i\}_q)$; hence for two dots, $(\{n_i\}) = (\{n_i\}_{q=1})(\{n_i\}_{q=2})$. When considering spin, we will let all odd p refer to spin down electrons, and all even p refer to spin up electrons. Since no interdot or second order events are considered, transitions like $(1, 0) \leftrightarrow (0, 1)$ and $(0, 0) \leftrightarrow (1, 1)$ do not appear in the set of equations given by Eq. (3.11).

3.2.2 Solutions for Coupled Differential Equations

In the notation of Eq. (3.3), the total number of possible configurations for a given system is 2^s, where

$$s = \gamma i q, \tag{3.18}$$

q is the number of dots, i is the total number of levels per dot, and γ is the degeneracy of the dot energy levels.

The rate equations for a system may be written as either a set of 2^s coupled homogeneous differential equations, or, using the condition $\sum P(\{n_i\}) = 1$, $2^s - 1$ coupled inhomogeneous differential equations. In theory, the equations may always be solved analytically, but only in the case of extremely small systems with time-independent coefficients is this practical. For every additional degree of complexity of the system, the number of coupled differential equations doubles, and the number of coefficients (constant or otherwise) increases to the square of its previous value.

Overall, the biggest challenge presented in modeling QD systems did not concern numerical integration, but rather the entry of 2^{2s} coefficients, some of which were time dependent. However, the latter is not as informative, so the code which generated the coefficient matrix is given in Appendix D.1, and the code which set up the system of differential equations is given in Appendix D.2. The algorithms used by `NDSolve` (Mathematica's numerical differential equation solving function) are presented as Appendix A.2.

3.3   Current

In describing current through a quantum dot, one must address the statistical nature of transport. The current through the left dot-reservoir lead is expressed as [62]

$$I_l = -e \sum_p \sum_{\{n_i\}} \Gamma_p^l P(\{n_i\}) \{\delta_{n_p,0} f(E^{i,l}(N) - E_F) - \delta_{n_p,1}[1 - f(E^{f,l}(N) - E_F)]\}. \quad (3.19)$$

Current through the right lead is written in a similar manner as Eq. (3.19), although with the opposite sign and different subscripts.

We therefore adopt the convention (see Fig. 3.2) that contributions to left current are positive for electrons entering the dot, and negative for electrons entering the left reservoir; contributions to current through the right lead are positive for electrons leaving the dot and entering the right reservoir and negative for electrons entering the dot from the right.
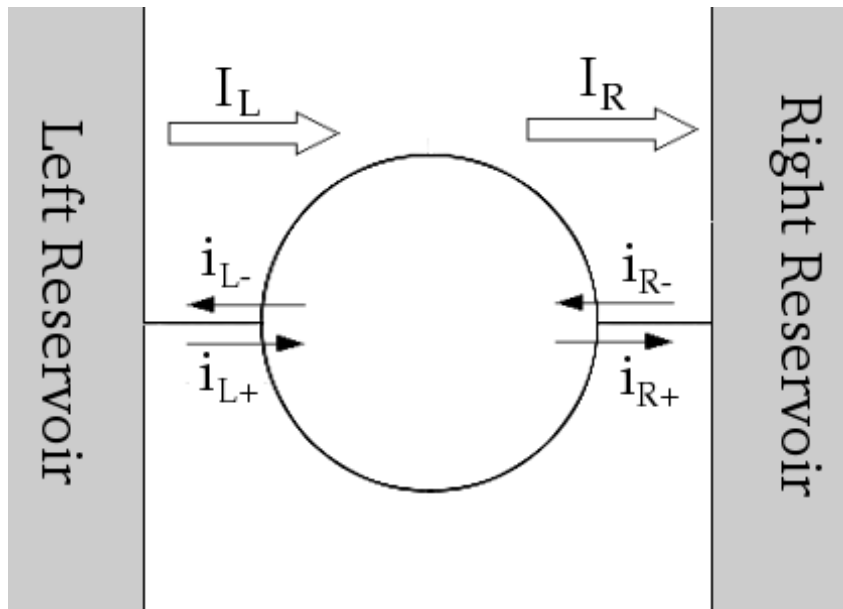
Electrons entering the dot from the left reservoir constitute i_{L+}, and electrons leaving the dot for the left reservoir constitute i_{L-}. The total current through the left lead, I_L, is the sum of i_{L+} and i_{L-}. Similarly, positive contributions to the current through the right lead are given by i_{R+}, and negative contributions by i_{R-}.

Figure 3.2: Current Direction Convention in a Quantum Dot

31

The total current through one lead, as in Eq. (3.19), can be split into the sum of positive and negative contributions, i.e.

$$i_{l+} = -e \sum_p \sum_{\{n_i\}} \Gamma_p^l P(\{n_i\}) \{\delta_{n_p,0} f(E^{i,l}(N) - E_F) \tag{3.20}$$

$$i_{l-} = e \sum_p \sum_{\{n_i\}} \Gamma_p^l P(\{n_i\}) \delta_{n_p,1} [1 - f(E^{f,l}(N) - E_F)]\}. \tag{3.21}$$

Similar expressions can be found for current through the right lead.

Finally, the accumulated charge on the dot can be found by integrating the sum of the right and left currents with respect to time:

$$Q_{net} = \int dt (I_L + I_R). \tag{3.22}$$

At zero bias and for $\Gamma_L = \Gamma_R$, no charge should accumulate on the dot. If $\Gamma_L \neq \Gamma_R$, some charge may accumulate temporarily, but for $t \to \infty$ the net charge should still be zero.

3.3.1 Example: Current for a Single Dot

The compact notation of Eq. (3.19) lends itself to confusion. For clarity, we continue the example from Sec.3.2.1 of a single dot with two levels by writing expressions for current. Using Eq. (3.20), the left current is given by the electrons moving into the dot,

$$i_{L+} = -e\,\Gamma_L[2P(0,0)f(E^{i,l}(0) - E_F) \\ + P(1,0)f(E^{i,l}(1) - E_F) + P(0,1)f(E^{i,l}(1) - E_F)], \tag{3.23}$$

minus the contributions of electrons leaving the dot for the left reservoir,

$$i_{L-} = -e\,\Gamma_L[(P(1,0)(1 - f(E^{f,l}(1) - E_F)) \\ + P(0,1)(1 - f(E^{f,l}(1) - E_F)) + 2P(1,1)(1 - f(E^{f,l}(2) - E_F))]. \tag{3.24}$$

We have dropped the index p in Γ_L since we are assuming (as is appropriate in the wide band approximation) that transmission rate is independent of energy. The total left current is then

$$
\begin{aligned}
I_L &= i_{L+} - i_{L-} & (3.25)\\
&= -e\,\Gamma_L[2P(0,0)f(E^{i,l}(0) - E_F) - 2P(1,1)(1 - f(E^{f,l}(2) - E_F))\\
&\quad + P(1,0)[f(E^{i,l}(1) - E_F) - (1 - f(E^{f,l}(1) - E_F)]\\
&\quad + P(0,1)[f(E^{i,l}(1) - E_F) - (1 - f(E^{f,l}(1) - E_F)]]. & (3.26)
\end{aligned}
$$

For the right current, i_{R+} contains the terms describing electrons moving from the dot to the right reservoir, and i_{R-} contains the terms for electrons leaving the right reservoir and entering the dot. The final expression is

$$
\begin{aligned}
I_R &= i_{R+} - i_{R-} & (3.27)\\
&= +e\,\Gamma_R[2P(0,0)f(E^{i,r}(0) - E_F) - 2P(1,1)(1 - f(E^{f,r}(2) - E_F))\\
&\quad + P(1,0)[f(E^{i,r}(1) - E_F) - (1 - f(E^{f,r}(1) - E_F)]\\
&\quad + P(0,1)[f(E^{i,r}(1) - E_F) - (1 - f(E^{f,r}(1) - E_F)]]. & (3.28)
\end{aligned}
$$

3.4   Conductance

QD systems are frequently modeled as a macroscopic electronic circuits [39, 54, 65]. The analogy is so ubiquitous that one would expect conductance to follow, as usual,

$$
G = I/V_{bias}. \tag{3.29}
$$

While Eq. (3.29) does describe conductance for a QD system, it holds only in the limit that $V_{bias} \to 0$ (linear regime).

Classically, electrons cannot traverse the dot-reservoir barrier, so junctions are modeled as capacitors. Quantum mechanically, however, electrons can tunnel through the barriers such that conductance across the dot is a function of the barrier potential. The conductance may be calculated by starting with the Landauer formula [56],

$$G = \frac{2e^2}{h}\overline{\mathbb{T}}(E).\tag{3.30}$$

In Eq. (3.30), $\overline{\mathbb{T}}(E)$ is the transmission function, expressible in terms of the number of propagating modes of a contact M, and the average probability of transmission across the contact $\mathbb{T}$, or alternatively the trace over the transmission coefficient matrix as defined in Eq. (3.4):

$$\begin{align}
\overline{\mathbb{T}}(E) &= M\mathbb{T}(E)\tag{3.31}\\
&= \sum_p \sum_q T_{pq}(E).\tag{3.32}
\end{align}$$

In systems with multiple conducting channels, conductance between channels p and q can be expressed as

$$G_{pq} = \frac{2e^2}{h}\int \overline{\mathbb{T}}_{pq}(E)\left(\frac{-\partial f_0}{\partial E}\right)dE,\tag{3.33}$$

where $f_0(E)$ is the equilibrium Fermi function.

At low temperatures, we note that $-\partial f_0/\partial E \simeq \delta(E_F - E)$, so that conductance is

$$G_{pq} = \frac{2e^2}{h}\overline{\mathbb{T}}_{pq}(E_F).\tag{3.34}$$

For finite temperature, when the resonance condition in Eq. (2.16) is met, Eq. (3.33) is

$$G_{pq} = \frac{2e^2}{h}\int \frac{\overline{\mathbb{T}}_{pq}(E)}{4k_BT\cosh^2(\frac{E_F-E}{2k_BT})}dE,\tag{3.35}$$

the familiar result for conductance found in the literature.

In Section 3.1.1, it is shown that the transmission matrix elements are related to the transition rates Γ. Working in the wide band approximation at finite temperature, we allow Γ to be independent of energy, so that conductance near a Coulomb Blockade resonance is

$$G = \frac{\Gamma_1 \Gamma_2}{\Gamma_1 + \Gamma_2} \frac{1}{4k_B T \cosh^2\left(\frac{\varepsilon - \mu}{2k_B T}\right)}. \tag{3.36}$$

The desired final form for conductance should account for non-coherent transport in the linear regime across both dot-reservoir leads, including charge quantization and the exclusion principle. A derivation may be found in part in [56], and in its entirety in [61, 66]. The result is [48]

$$G(E_F) = \frac{e^2}{k_B T} \sum_p \frac{\Gamma_1^p \Gamma_2^p}{\Gamma_1^p + \Gamma_2^p} \sum_N P_{eq}(N) F_{eq}(E_p|N)[1 - f(E_p + U(N) - U(N-1) - E_F)], \tag{3.37}$$

where

$$P_{eq}(N) = \sum_{\{n_i\}} \delta_{N, \sum_i n_i} \tag{3.38}$$

and

$$F_{eq}(E_p|N) = \frac{1}{P_{eq}(N)} \sum_{\{n_i\}} P_{eq}(\{n_i\}) \delta_{n_p, 1} \delta_{N, \sum_i n_i}. \tag{3.39}$$

Finally, current can be calculated from by back substitution of Eq. (3.37) into Eq. (3.29),

$$I = \frac{e^2 V_{bias}}{k_B T} \sum_p \frac{\Gamma_1^p \Gamma_2^p}{\Gamma_1^p + \Gamma_2^p} \sum_{\{n_i\}} P_{eq}(\{n_i\}) \delta_{n_p, 0} f(E_p + U(N+1) - U(N) - E_F), \tag{3.40}$$

where we take the limit $V_{bias} \to 0$.

3.5 Chapter Summary

This chapter reviewed the formulation of the rate equations, starting with the construction of the Hamiltonian for a dot-reservoir system. For weakly coupled dots, the interac-

tion term in the Hamiltonian was be treated as a perturbation. Fermi's golden rule was subsequently used to calculate transition rates for electrons moving from dot to reservoir (and vice versa).

Next, the rate equations were presented in compact notation and the individual terms of the equations were examined. The rate equations were used to generate expressions for the current and conductance of a quantum dot. As an instructive example, the rate equations and expressions for current and conductance were applied to the system of a single quantum dot with one reservoir.

CHAPTER FOUR:
RESULTS AND DISCUSSION

In this Chapter, numerical simulations based on the theoretical framework of Chapters 1.2 and 2.5 will be presented in two parts. The first part explores stationary attributes of the quantum dot systems, namely equilibrium probability distributions. The second part is devoted to dynamical phenomena, and comprises the main result of this research.

4.1   Stationary Results

In this Section, numerical and analytical solutions of a test case are compared in order to verify that the results are consistent. The next-most-complicated case of two coupled dots with no applied magnetic field was analyzed in the same manner. The appearance of a degenerate region between equivalent charge states indicates that the rate equations do not completely describe the system. The phenomenon is also seen in a system which has an applied magnetic field. Finally, conductance is calculated for both spin degenerate and spin split systems then plotted in the gate voltage phase space.

4.1.1   Single Dots: A Test Case

Before approaching more complex systems, it was necessary to examine the validity of the results obtained with the rate equation method and to establish a working regime. A system composed of a single quantum dot with one available energy level and coupled

to two reservoirs at zero bias provided a suitable test model, since its rate equations may be solved analytically. Numerical and analytic results were then be compared in order to determine the accuracy of the code.

Using the general form for the rate equations [Eq. (3.11)], and the initial conditions $P_0(t = 0) = 1$, $P_1(t = 0) = 0$ (that is, the dot contains no electrons), analytic solutions are

$$P_0(t) = 1 - f(E) \left[1 - e^{-\Gamma t} \right], \tag{4.1}$$

$$P_1(t) = f(E) \left[1 - e^{-\Gamma t} \right]. \tag{4.2}$$

A comparison of Eqs. (4.1) and (4.2) to numerically calculated data shows perfect agreement (Fig. 4.1). The energy level of the dot was chosen somewhat arbitrarily, as were the values for $\Gamma_{L(R)}$ and capacitances. The only criteria in choosing these values were those dictated in Chapter 2; i.e., that charging energy is in the neighborhood of level spacing, and that system temperature and $\hbar\Gamma$ are much smaller.

The data obtained in this simulation (Fig. 4.1) reflects the equilibrium probabilities of the system. To calculate each data point, the applied gate voltage and initial conditions were specified, and integration of the rate equations occurred for a total time interval much longer than the relaxation time of the system. Because of this, solutions do not reflect the state of the system at any previous time. In this limit, the electrostatic treatment of quantum dots (as given in Chapter 2) is perfectly valid.
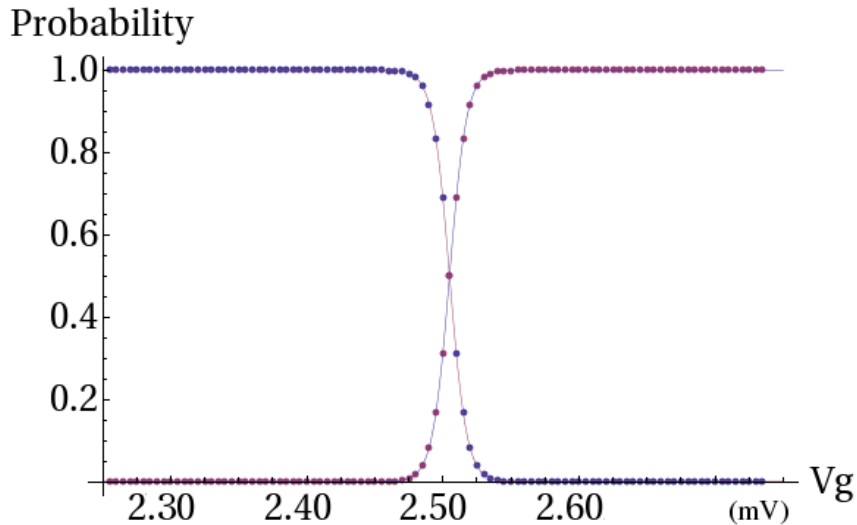
State probabilities for a single quantum dot with one available energy level, as functions of the gate voltage. Solid lines represent analytical solutions [Eqs. (4.1), (4.2)], whereas numerical data is represented by points. The blue line is the probability P_0 (no electrons in the dot), and purple represents the probability P_1 (one electron in the dot). Here, gate voltage is swept adiabatically such that the system is fully relaxed for each value of V_g. Scaling corresponds to $\Delta\epsilon = 1$ meV, $E_c = 1.5$ meV, $k_B T = 10^{-2}$ meV, and $\hbar\Gamma = 5 \times 10^{-3}$ meV.

Figure 4.1: Stationary Probabilities for One Dot

The obtained probabilities can be used in calculating current and conductance for the system via Eqs. (3.19) and (3.29) or (3.36). In equilibrium, with no applied bias, the left and right currents should be equal and opposite, with a line shape identical to that of conductance, which is shown in Fig. 4.2. In the limit $T \to 0$, the conductance peak takes the Breit Wigner (Lorentzian) form for resonant tunneling. Since we will not be working in the thermodynamic limit, all of our calculations show thermal broadening.
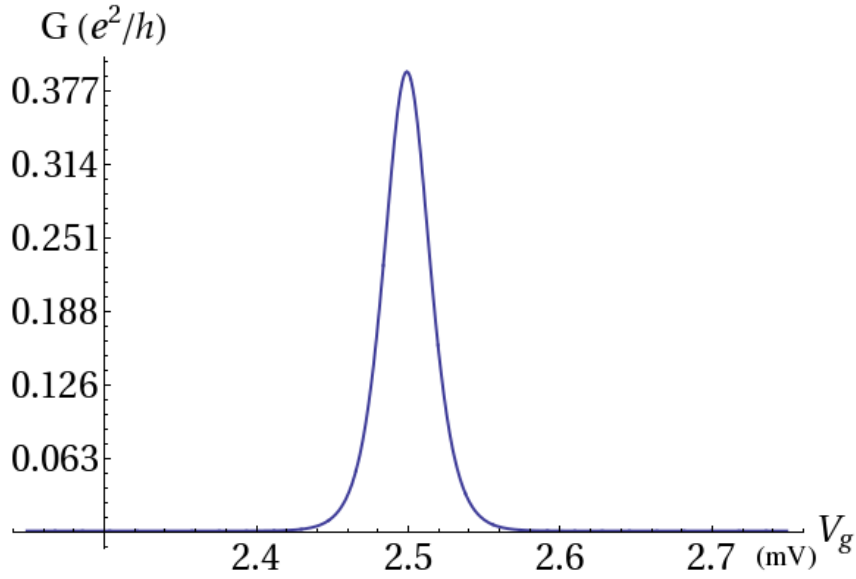
Conductance peak in the resonant tunneling regime. Scaling corresponds to $\Delta\epsilon = 1$ meV, $E_c = 1.5$ meV, $k_B T = 10^{-2}$ meV, and $\hbar\Gamma = 5 \times 10^{-3}$ meV.

.

Figure 4.2: Conductance Across One Dot

To evaluate the relaxation time, a small segment of code was inserted into the program which halted numerical integration when the initial state probability ($P_0(t = 0) = 1$) became sufficiently small. The total number of time steps was returned, which was translated as the transition time of the system.

This method is easy to use, and useful as a guide when constructing time-dependent variables, but introduces some uncertainty in any subsequent calculations requiring the solutions to the rate equations. The magnitude of the introduced error depends on the given exit condition. For instance, accuracy to within 0.01% requires the program to halt evaluation when the probability of the initial state reaches $P_0(t) = 0.0001$. Further calculations may be assumed to propagate this 0.01% uncertainty, in addition to any other introduced uncertainties (for instance, those introduced by the numerical integration algorithm- see Appendix A.2).

4.1.2 Coupled Dots with One Degenerate Level Each

The equilibrium charge state probabilities, stationary current, and transition rates of a system of two coupled dots in parallel with one available energy level each is explored in this Section. This configuration provides the basis for the spin-split system considered in the next Subsection. Here, it will be assumed that energy levels are singly occupied, so that the spin degeneracy of the system does not lead to any Hund shell filling rules, and that the spin of any given electron may be up or down with equal probability.

The four possible configurations for this system are shown in Fig. 2.3 and are detailed in Sec. 2.3.1. The rate equations governing the non-equilibrium state probabilities are nearly identical to Eqs.(3.14) - (3.17), since both interdot transitions and intradot transitions are not considered; we only need to index two additional Γs to account for the two additional leads. We also distinguish between the two dots by indexing the argument of the Fermi function. As an example, Eq. (3.13) becomes

$$
\begin{aligned}
\frac{\partial}{\partial t}P(0,0) \;=\; & -P(0,0)[(\Gamma_1^l + \Gamma_1^r)f(E_1^i(0) - E_F) + (\Gamma_2^l + \Gamma_2^r)f(E_2^i(0) - E_F)] \\
& +P(1,0)\{(\Gamma_1^l + \Gamma_1^r)[1 - f(E_1^i(1) - E_F)])]\} \\
& +P(0,1)\{(\Gamma_2^l + \Gamma_2^r)[1 - f(E_2^i(1) - E_F)]]\},
\end{aligned}
\tag{4.3}
$$

where $\Gamma_{1(2)}^{l(r)}$ now indicates a transition between dot 1(2) and the left(right) reservoir. Similarly, the subscript of $E_{1(2)}^{i(f)}$ [given by Eq. (2.15)] denotes that dot 1(2) was involved in an interaction with a reservoir. E_F does not need an index as it is assumed that the left and right reservoirs are held at the same chemical potential.
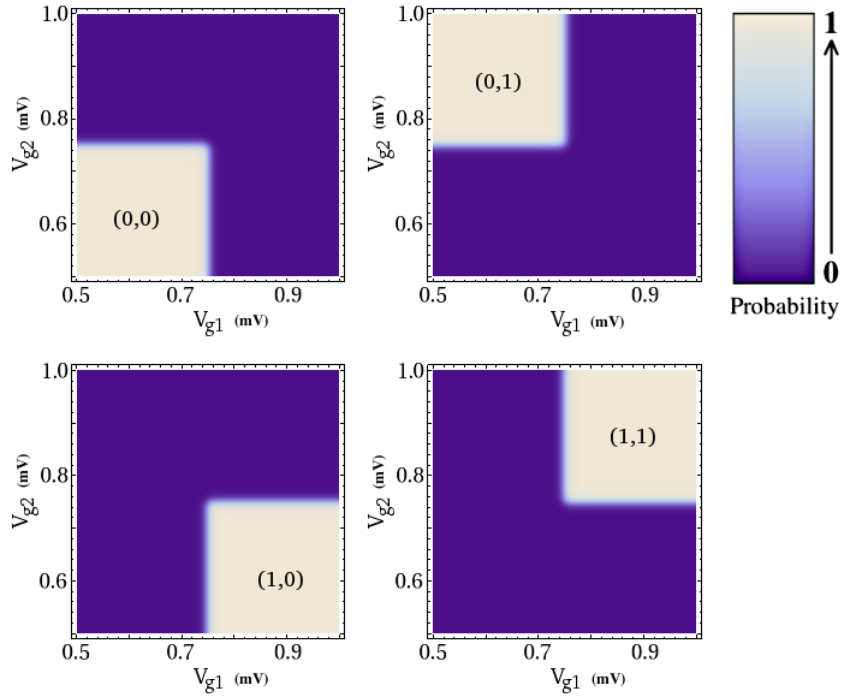
State probabilities for a double dot system where each dot has one available energy level. Interdot coupling is zero. V_{g1} lies on the horizontal axis, and V_{g2} lies on the vertical axis. Scaling corresponds to $\Delta\epsilon = 1.2$ meV, $E_c = 1.25$ meV, $k_B T = 10^{-2}$ meV, and $\hbar\Gamma = 5 \times 10^{-3}$ meV.

Figure 4.3: Stationary Probabilities for a DQD when $C_m = 0$

Solutions to this system were found numerically. Figures 4.3, 4.4, and 4.5 show stationary solutions to the rate equations when the interdot coupling is negligible, small, and relatively large, respectively.
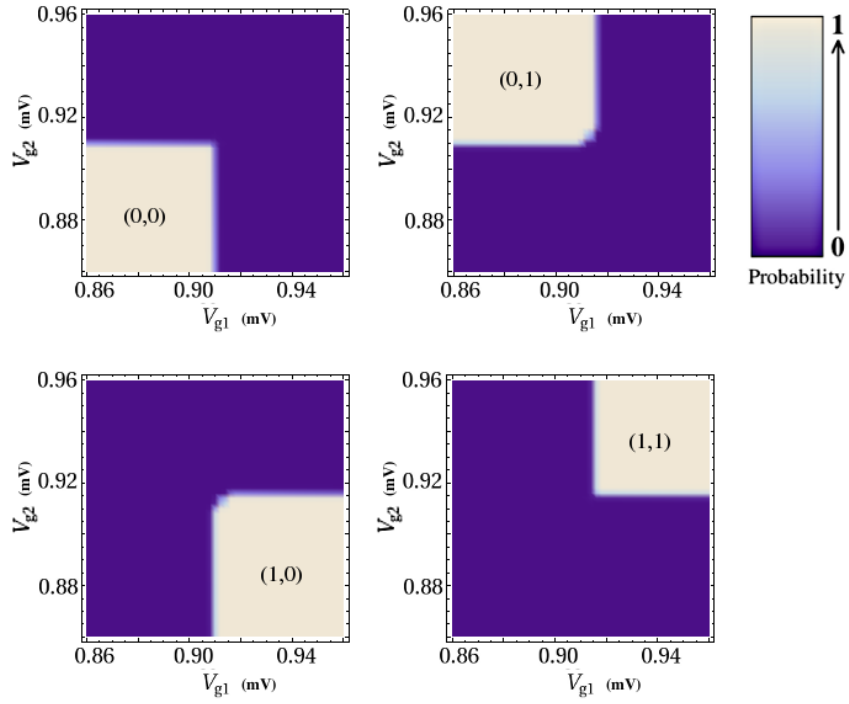
State probabilities for a double dot system where each dot has one available energy level. Interdot coupling is small but not negligible, $C_m = 0.01$. V_{g1} lies on the horizontal axis, and V_{g2} lies on the vertical axis. Scaling corresponds to $\Delta\epsilon = 1.2$ meV, $E_c = 1.237$ meV, $k_B T = 10^{-2}$ meV, and $\hbar\Gamma = 5 \times 10^{-3}$ meV.

Figure 4.4: Stationary Probabilities for a DQD when $C_m = 0.01 C_g$
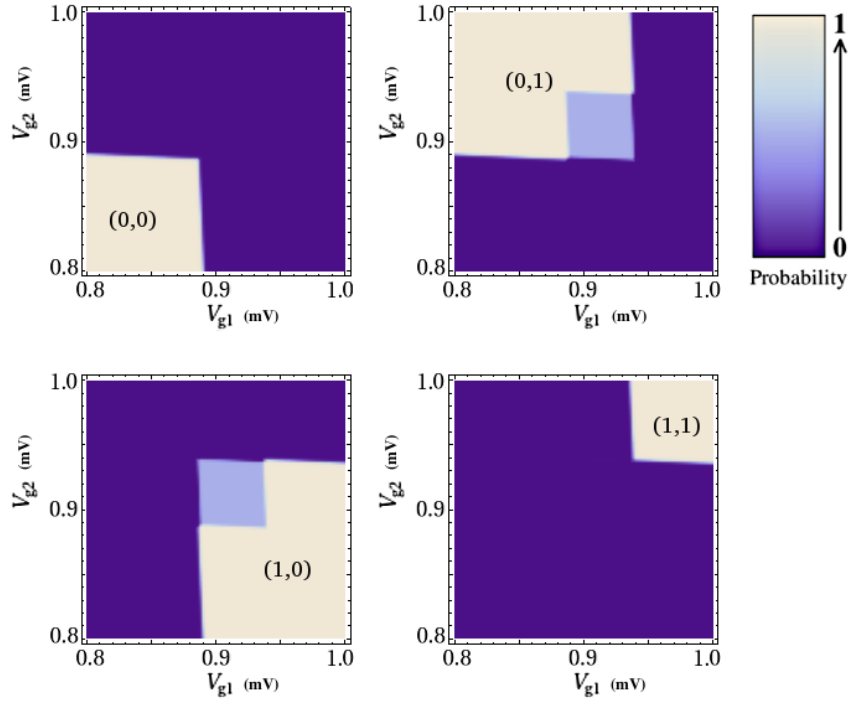
State probabilities for a double dot system where each dot has one available energy level. Interdot coupling is relatively large, $C_m = 0.1C_g$. V_{g1} lies on the horizontal axis, and V_{g2} lies on the vertical axis. The small rhombic region shared by P(1,0) and P(0,1) corresponds to probability 1/2 for both configurations. Scaling corresponds to $\Delta\epsilon = 1.2$ meV, $E_c = 1.146$ meV, $k_BT = 10^{-2}$ meV, and $\hbar\Gamma = 5 \times 10^{-3}$ meV.

Figure 4.5: Stationary Probabilities for a DQD when $C_m = 0.1C_g$
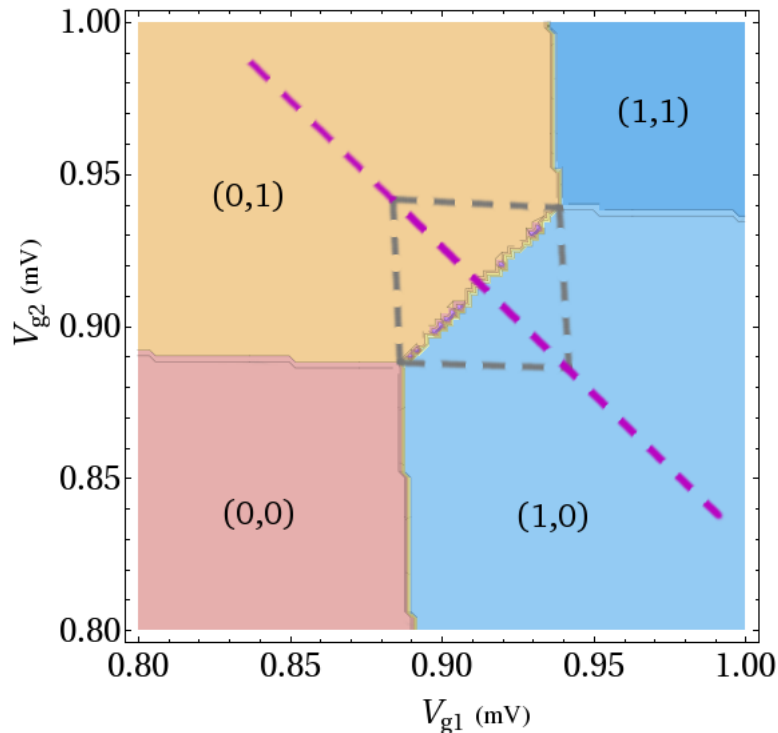
The stability diagram for coupled dots with one available energy level each. The boundary between the equal charge regions (1,0) and (0,1) lies along the line $V_{g1} = V_{g2}$ for symmetric dots. Shown in magenta is the general path in phase space used in investigating hysteretic behavior in coupled dots (Figs. 4.7a and 4.7b), $V_{g1} = -V_{g2} + const$.

Figure 4.6: Stability Diagram for Coupled Dots with One Level Each

Degenerate Regions

In Figures 4.5 and 4.4, there exists a small rhombic region where the probabilities of equal charge states overlap in phase space. For time intervals outside the relaxation time of the system (in other words, in the adiabatic regime), the rate equations do not completely determine the state of the system, and the equal charge configurations are equally probable for gate voltages corresponding to those in the degenerate region. When gate voltage is varied at a rate $\Delta t^{-1} = \tau_d^{-1}$, the system's memory allows one state to remain dominant even in the vicinity of $V_{g1} = V_{g2}$. The boundaries of the overlap area can be found by extending the lines $U(1,1) = U(1,0)$, $U(1,1) = U(0,1)$, $U(1,0) = U(0,0)$, and $U(0,1) = U(0,0)$ past $V_{g1} = V_{g2}$ (see Figs. 2.8 and 4.6).

In this region, the total energy of the dots is the same. For systems which allow interdot tunneling, the area represents the set of gate voltages for which an electron is delocalized over both dots. This phenomena can be explored as a mechanism for "switching" behavior in dots, since the size of the region can be externally controlled by adjusting the gate voltages.

The hysteretic behavior of the dots is investigated here pumping back and forth along the line $V_{g2}(t) = -V_{g1}(t) + const.$ for a variety of time step sizes. Coarse graining is used when deriving the rate equations, where it is assumed that the dwell time of electrons on a dot, τ_d, follows $\tau_d \gtrsim \Gamma^{-1}$, and that the confining potential varies slowly. The rate equation method can be expected to break down when the rate of change of the gate voltage, Δt^{-1}, is comparable to Γ. Results are plotted in Figs. 4.7a and 4.7b. The limitations of the model are immediately apparent, with the transition from $P(10) \to P(01)$ sharply defined when $\Delta t^{-1} << \Gamma$. The calculated probabilities appear to have some memory as $(\Delta t \Gamma)^{-1}$ increases, indicating a breakdown of the rate equation method as it is employed here. In this context, the calculated probabilities should not be taken as reliable indicators of the system configuration during a single cycle, but could be interpreted as the mean probability over the course of several cycles, as long as $\Delta t \sim \tau_d$. Systems with fast-varying coefficients are perhaps better treated using a non-equilibrium Green's function approach, such as the Keldysh or Kubo formalisms.

The presence of the degenerate region in the adiabatic limit presents problems when trying to determine the best set of parameters for charge and spin pumping. More complex systems have even more overlapping equal probability regions, and show the same hysteretic behavior. The effect does not seem to be merely an artifact of the rate equation method but is rather due to the discrete nature of the system; the lines simply correspond to where levels (1,0) and (0,1) are in resonance with the reservoir Fermi levels. Similar constructs appear in Coulomb blockade "diamonds" for systems under bias (see, among many others, Ref. [67]). The hysteretic nature of charging also seems to manifest in electron transport in large arrays of QDs [68], and could possibly provide an explanation
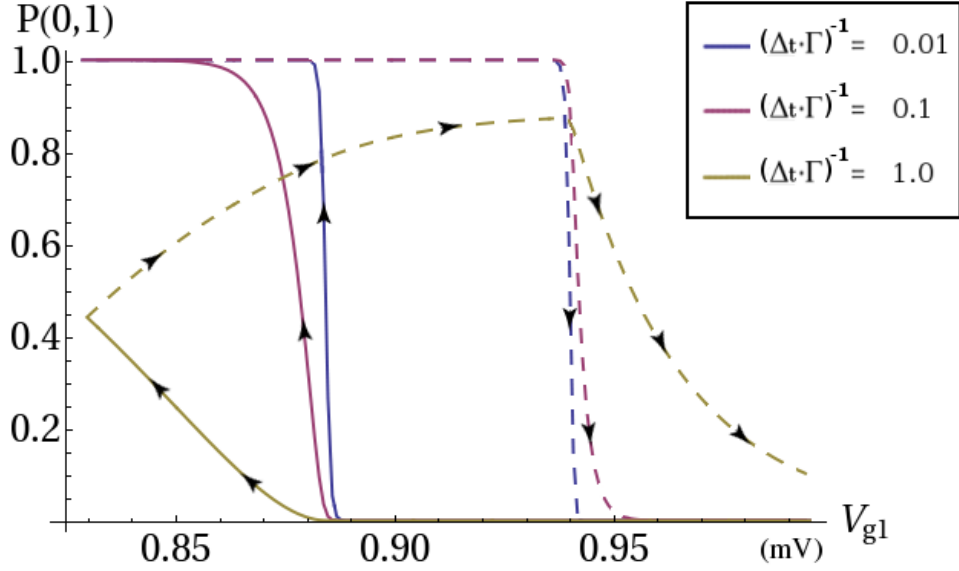
(a) Hysteresis for P(0,1)
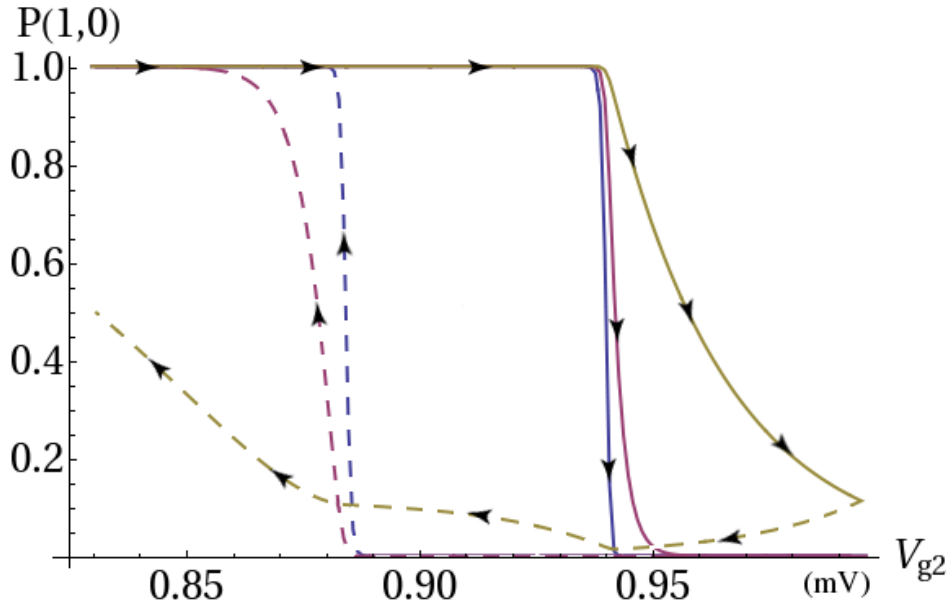
(b) Hysteresis for P(1,0)

(a) Probability for state (0,1), plotted with respect to V_{g1}, where $V_{g1} = -V_{g2}$. (b) Probability for state (1,0), plotted with respect to V_{g1}, where $V_{g1} = -V_{g2} + constant$. The arrows indicate the direction of increasing time. Scaling corresponds to $\Delta\epsilon = 1.2$ meV, $E_c = 1.237$ meV, $k_B T = 10^{-2}$ meV, and $\hbar\Gamma = 5 \times 10^{-3}$ meV.

Figure 4.7: Switching Behavior in Parallel DQDs

for discrepancies in charging behavior between systems with different numbers of dots, as in Ref. [69].

Stationary Current Through Coupled Dots

Stationary current and conductance through each dot may be found in the same manner as in Sec. 4.1.1. Since current must be calculated with respect to one node at a time, there are four quantities to consider for two coupled dots: right and left current through the top dot, and right and left current through the bottom dot. We will consider the current through the left lead of the top dot.

Figure 4.8a shows the left current through the top dot when $C_m = 0$. The peak occurs, as expected, when the resonance condition is met [Eq. (2.16)] and conductance is maximized. In Fig. 4.8b, the normalized conductance (G/G_{max}) for the top dot has been plotted in the phase space of V_{g1} and V_{g2}. So that we may qualitatively examine the effects of thermal broadening, Figure 4.8a has been plotted for $k_B T = 10^{-2}$ meV, whereas in Fig. 4.8b, values were calculated with $k_B T = 10^{-3}$ meV.

(a) Current for Decoupled Dots
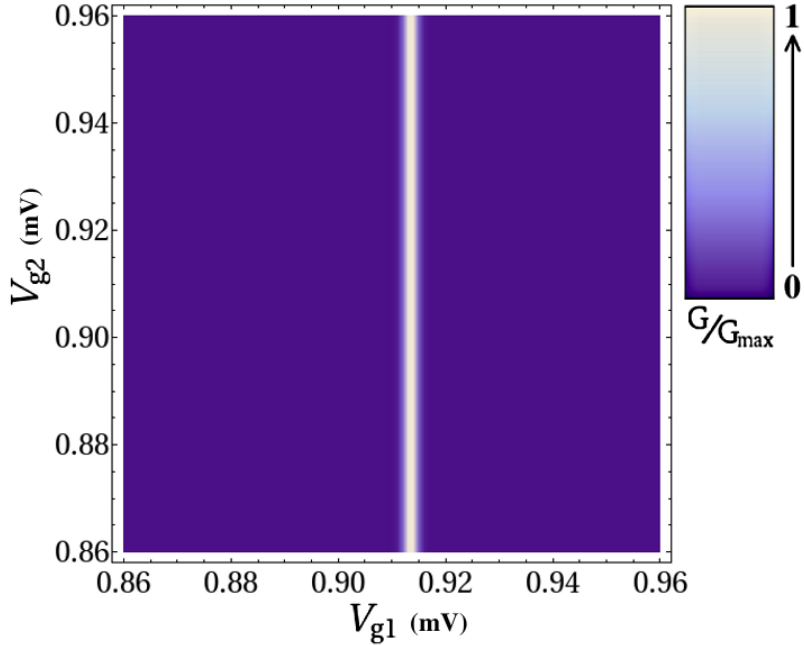
(b) Conductance for Decoupled Dots

(a) Stationary current through the left lead of the top dot when $C_m = 0$, plotted as a function of V_{g1}. Here, V_{g2}=0.8 mV is held constant, and $k_B T = 10^{-2}$ meV. (b) Conductance as calculated through the top dot when $C_m = 0$, plotted as a function of gate voltages. Here, $k_B T = 10^{-3}$ meV. Otherwise, scaling for both corresponds to $\Delta\epsilon = 1.2$ meV, $E_c = 1.25$ meV, and $\hbar\Gamma = 5 \times 10^{-3}$ meV.

Figure 4.8: Current and Conductance in Decoupled Dots

Figure 4.9 shows the left current through the top dot when C_m is relatively large, $C_m = 0.1C_g$. Current was calculated for a range of V_{g1}, while the gate voltage applied to

the bottom dot was held constant at $V_{g2} = 0.91$. This choice of parameters, which allows the examination of current at the boundaries of the degenerate region, is represented by the dashed magenta line in the inset. The slight asymmetry in the current peaks when moving from (0,1) to the central region, as compared to the current when moving from the degenerate region to (1,0), is the result of choosing a value for V_{g2} which corresponds to the equilibrium charge configuration $(1, 0)$. In this case electrostatic distortion of dot 1 from dot 2 suppresses the conductance of the leads connected to dot 1, decreasing the current. For comparison, the conductance when $C_m = 0.1 C_g$, shown in the phase space of V_{g1} and V_{g2} in Fig. 4.10, was calculated using Eq. (3.29). The conductance is highest at the interfaces (0,0)→(1,0), and (0,1)→(1,1), with local maxima bordering the degenerate region and states (1,0) and (0,1).We note that the dots are not directly coupled, so that the transition from (0,1) to (1,0) does not represent an electron hopping between the dots. Rather, this result could be interpreted as the current due to cotunneling, in which one dot is evacuated as the other dot simultaneously gains an electron, thus accounting for the difference in the magnitude of the currents in Figs.4.8a and 4.9.
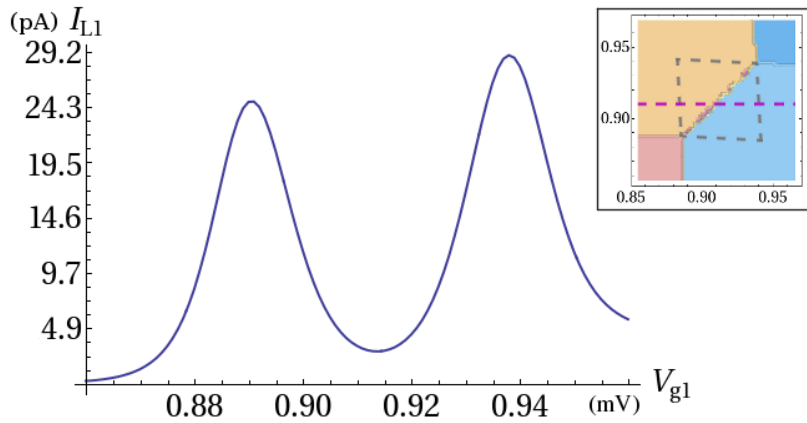
Stationary left current through the top dot when $C_m = 0.1 C_g$, plotted as a function of gate voltage V_{g1}. The gate voltage of the bottom dot, V_{g2}, has been held constant at $V_{g2} = 0.91$ mV, in order to examine current at the boundaries of the degenerate region, as shown in the inset. The dashed gray lines represent the boundaries of the degenerate regions. The dashed blue line indicates the the path in phase space of the gate voltages used to calculate stationary left current. Scaling corresponds to $\Delta\epsilon = 1.2$ meV, $E_c = 1.146$ meV, $k_B T = 10^{-2}$ meV, and $\hbar\Gamma = 5 \times 10^{-3}$ meV.
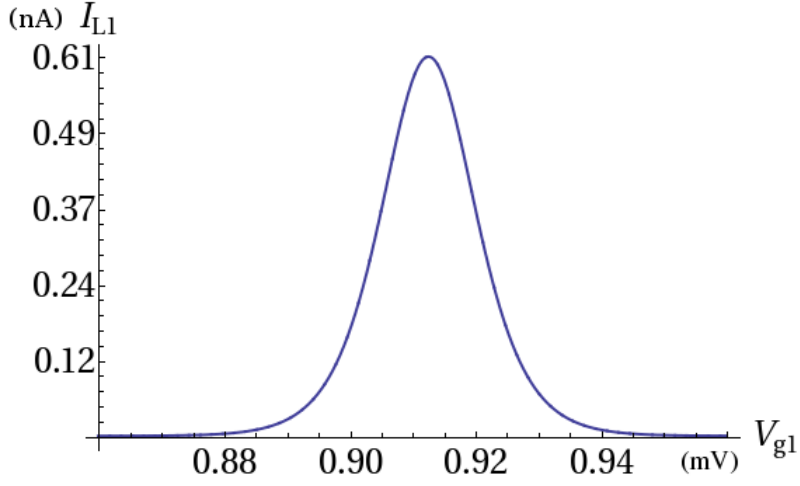
Figure 4.9: Stationary Current for Coupled Dots
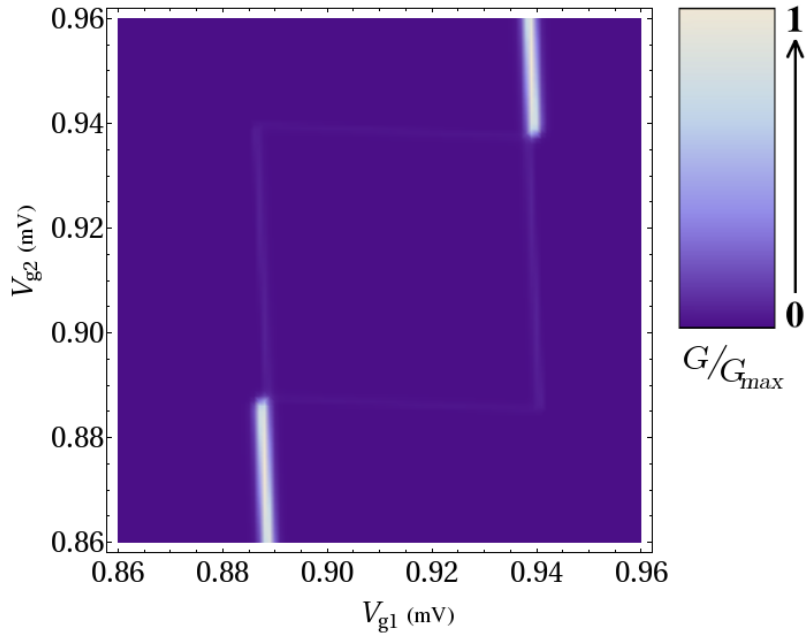
Conductance for the top dot with $C_m = 0.1C_g$, expanded to show features across the degenerate region. Values are found in the stationary regime. Scaling corresponds to $\Delta\epsilon = 1.2$ meV, $E_c = 1.146$ meV, $k_B T = 10^{-2}$ meV, and $\hbar\Gamma = 5 \times 10^{-3}$ meV.

Figure 4.10: Conductance for Coupled Quantum Dots

4.1.3   Coupled Dots with Spin Splitting

In Sec. 2.4, the Zeeman effect was introduced as a means of selecting the spin of electrons tunneling into or out of a dot. When a magnetic field is applied in the plane of the 2DEG, the degeneracy of the dot's energy levels is broken, and the charging energy [Eq. (2.15)] must be corrected with the Zeeman energy, $\Delta E_Z = |g|\mu_B B$ [Eq. (2.22)]. We wish to have $\Gamma < \Delta E_Z < \Delta E$, and using $g = -0.44$ for GaAs leads to values around $\Delta E_Z \simeq 25$ μeV per Tesla, so we restrict the magnitude of the applied magnetic field . The new expression for charging energy reads

$$E_c = E_{c,classical} + (\epsilon_m \pm \Delta E_Z) - (\epsilon_n \pm \Delta E_Z). \tag{4.4}$$

In Eq. (4.4), in addition to accounting for discrete energy levels, the charging energy also includes a correction for spin splitting. Since we are working in the CI model, no further

corrections are needed.

In a two dot system with two non-degenerate energy levels per dot, there are 16 possible system configurations. The indices previously used to indicate the number of occupied levels per dot may also be used to denote the spin of the electrons. In this case, there are four indices ($\{n_i\}$), which will be written as ($N_{1\downarrow}N_{1\uparrow}, N_{2\downarrow}N_{2\uparrow}$). The first(last) two indices give the number of spin down and spin up electrons in dot 1(2), respectively. In Fig. 4.11, the probabilities in equilibrium are shown with respect to gate voltages for four states, with small but non-negligible C_m ($C_m = 0.01\ C_g$ and $\Delta E_Z = 0.05$ meV. As with the configuration of Sec. 4.1.2, in Fig. 4.11, degenerate regions form between states with the same charging energy. A similar configuration exists for states (11,00), (11,10), (10,10), and (10,00); those states with equivalent charge (but not necessarily spin), i.e. (10,10), (10,01), (01,10), and (01,01), share a more complex area in phase space. Geometrically, the boundaries of the region may be sketched as before, by extending the boundaries of other state probability regions. In this limit, where the running time of the code is very large, numerical solutions converge to classical probabilities.

Stationary Spin Current Through Coupled Dots

We consider the current through the left lead of the top dot in the presence of an applied magnetic field, taking care to distinguish between the spins of the electrons. The current may be written

$$I_{L1} = I_{L1\uparrow} + I_{L1\downarrow}, \tag{4.5}$$

with

$$I_{L1\uparrow} = i_{L1\uparrow+} + i_{L1\uparrow-} \tag{4.6}$$

$$I_{L1\downarrow} = i_{L1\downarrow+} + i_{L1\downarrow-}, \tag{4.7}$$

where the direction convention is the same as in Eqs.(3.24) and (3.23).
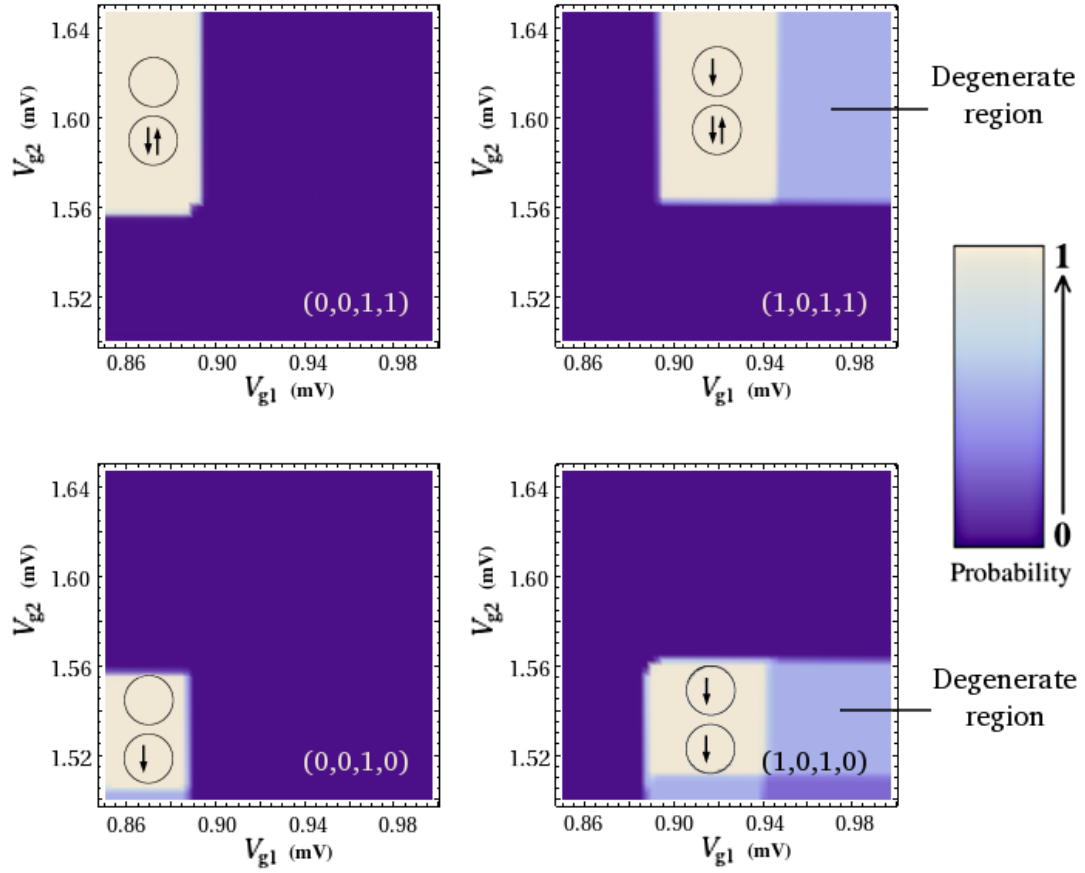
Probabilities for a two-dot system with spin splitting in equilibrium. Dark blue indicates low probability, whereas white or very light blue indicates high probability. States (00,11), (10,11), (10,10), and (00,10) are shown here, where a diagram of the system configuration, similar to those in Fig. 2.3, has been superimposed over each high-probability region The size of the degenerate areas is determined by the strength of the in-plane magnetic field. Scaling corresponds to $\Delta\epsilon = 1.2$ meV, $E_c = 1.237$ meV, $k_B T = 10^{-3}$ meV, $\hbar\Gamma = 5 \times 10^{-3}$ meV, and $\Delta E_Z = 0.05$ meV.

Figure 4.11: Stationary Probabilities for a DQD with Spin Splitting

In the absence of a field, it is reasonable to assume $I_{L1\uparrow} = I_{L1\downarrow}$, but in this case, Zeeman splitting allows the spin of the electrons to be selected via the gate voltage. In Fig. 4.12a, the normalized conductance of spin-down electrons in the left lead of the top dot is plotted in the phase space of V_{g1} and V_{g2} where the interdot coupling is $C_m = 0.01C_g$. Figures 4.12b- 4.12d show the normalized conductance of spin-up electrons in the left lead of the top dot, and for spin-down and spin-up electrons in the left lead of the bottom dot. Calculations have been made at lower temperature ($k_B T = 10^{-3}$ meV) to show the features of the system more clearly.

4.2   Dynamic Results

In recent years, there has been a considerable amount of interest in using quantum dots to generate charge or spin current (among others, [22, 70, 71, 72, 73, 74]). A number of the proposals use open dots and a pulsed confining potential to move charge, and some propose elaborate setups to generate spin currents [75, 76].

Given the results of Sec. 4.1.2, one might be tempted to increase the dot-lead coupling in order to speed up the pumping cycle while holding the value of $\Delta t\Gamma$ constant. However, doing so would necessarily decrease electron dwell time τ_d. When $\Gamma \sim \tau_d^{-1}$, transport is no longer dominated by sequential tunneling, current is not quantized, and coherent effects become more important. A number of papers address just such systems [67, 77].

We will attempt to increase the net current through a dot at zero bias by parameterizing the magnitude of the dot-reservoir coupling in addition to the gate voltage. Specifically, Γ^l and Γ^r can be varied out of phase with each other so that the lead favored for electron tunneling alternates, while the choice of parameterization for gate voltage depends on the particular configuration of the system and the desired outcome of the pumping cycle.

In this Section, both charge and spin pumping will be explored in the semiclassical approximation by simultaneously manipulating of dot-reservoir coupling constants and
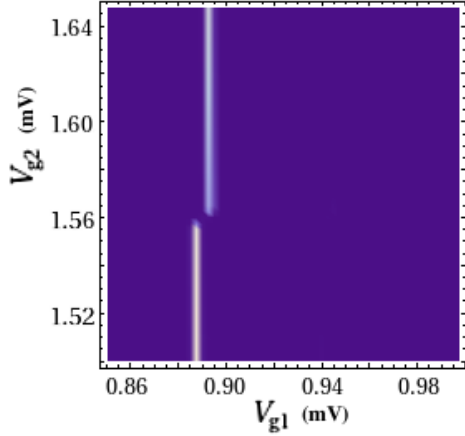
(a) Spin Down, Left Lead, Dot One   (b) Spin Up, Left Lead, Dot One
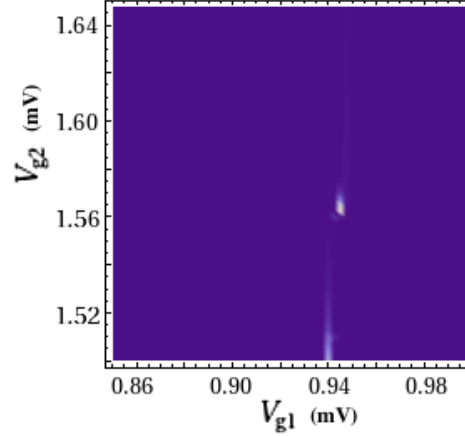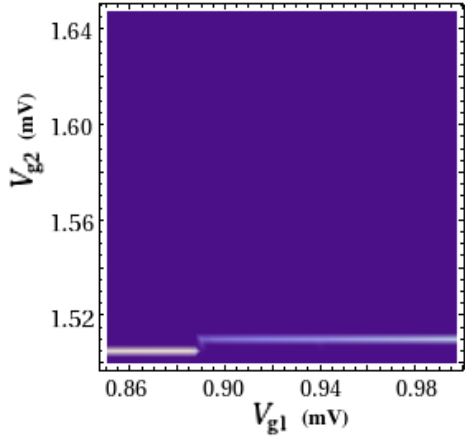
(c) Spin Down, Left Lead, Dot Two   (d) Spin Up, Left Lead, Dot Two
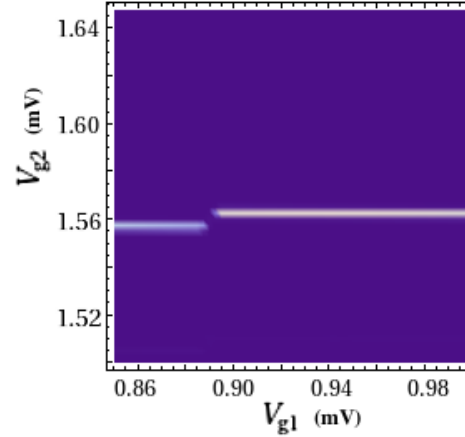
(a) The normalized conductance of spin-down electrons in the left lead of the top dot in the region of (00,10), (00,11), (10,10), and (10,11) is plotted with respect to gate voltages, with interdot coupling $C_m = 0.01Cg$. (b) Normalized conductance of spin-up electrons in left lead of the top dot. (c) Normalized conductance of spin-down electrons in left lead of the bottom dot. (d) Normalized conductance of spin-up electrons in left lead of the bottom dot. Scaling corresponds to $\Delta\epsilon = 1.2$ meV, $E_c = 1.237$ meV, $k_B T = 10^{-3}$ meV, $\hbar\Gamma = 5 \times 10^{-3}$ meV, and $\Delta E_Z = 0.05$ meV.

Figure 4.12: Spin Resolved Conductance

gate voltages. First, relationships between transition rates, dot-reservoir coupling Γ, and the sweep rate of the gate voltages will be discussed. We will then take advantage of the ability to externally control the coupling between each dot and reservoir to push electrons in a specific direction, as opposed to the application of a reservoir bias. Finally, using the stability diagram of the system as a guide, we will attempt to parameterize the gate voltages in such a way that one complete cycle results in a zero net charge current while generating a non-zero spin current.

4.2.1   Single Dots

A single dot may operate as an electron pump in the linear regime by parameterizing the gate voltage and the dot-reservoir coupling coefficients, where the choice of parameterizations directly influences the efficiency of the pump.

The frequency of the cycle may be determined by estimating the dwell time of an electron on the dot using mean values for the dot-lead coupling coefficients and dot electrostatic energy, assuming variations are small and occur relatively slowly. From Sec. 4.1.2, the pumping frequency should be smaller than the inverse dwell time of the electron on the dot, or

$$\omega < \frac{1}{\tau_d}. \tag{4.8}$$

Apart from maintaining a reasonably slow pumping frequency, the choice of parameterizations is arbitrary. Table 4.1 compares the average charge pumped per cycle, $\langle Q \rangle$, for three different sets of parameterizations. Each case used the same pumping frequency and the initial conditions $P(0) = 1$ and $P(1) = 0$, and each resulted in a different average pumped charge per cycle. Current through either lead fluctuates over the course of one cycle since the probability for each state takes a finite amount of time to evolve, although the total charge moved per cycle generally remains constant. A poor choice of parameters may actually inhibit the ability of the dot to pump electrons in the adiabatic limit; in Fig. 4.13 the average charge pumped per cycle is plotted with respect to pumping frequency

Table 4.1: Comparison of the Charge Pumped for Various Parameterizations

	$\Gamma_L(t)$	$\Gamma_R(t)$	$V_g(t)$	$\langle Q \rangle$
(A)	$\Gamma + \delta\Gamma\cos(\omega t)$	$\Gamma - \delta\Gamma\cos(\omega t)$	$V_g + \delta V_g\cos(\omega t)$	0.249
(B)	$\Gamma + \delta\Gamma\cos(\omega t)$	$\Gamma - \delta\Gamma\cos(\omega t)$	$V_g + \delta V_g\sin(\omega t)$	0.296
(C)	$\Gamma + \delta\Gamma\mathrm{sgn}(\cos(\omega t))$	$\Gamma - \delta\Gamma\mathrm{sgn}(\cos(\omega t))$	$V_g + \delta V_g\sin(\omega t)$	0.344

For three different parameterizations of gate voltage and dot-lead coupling in a single quantum dot, the average charge pumped per cycle for $\omega = 1.5$ GHz, is calculated. The charge pumped is also dependent on the rate at which voltage is varied; one may optimize the system for a given parameterization by estimating the electron dwell time using root mean square values for $\Gamma_R(t), \Gamma_L(t)$, and $V_g(t)$. Scaling corresponds to $\Delta\epsilon = 1$ meV, $E_c = 1.5$ meV, $k_BT = 10^{-2}$ meV, and $\hbar\Gamma = 5 \times 10^{-3}$ meV, with $\delta\Gamma = 2 \times 10^{-3}$ meV$/\hbar$.

for each of the three parameterizations shown in Table 4.1. In case A, represented by the blue line, the average charge pumped per cycle is largest for large ω, indicating that the current in this case is a non-equilibrium effect, and should be considered the result of an effective dot-lead bias. A phase shift of $\pi/2$ in $V_g(t)$ is more conducive to charge transport (cases B and C, shown with the magenta and tan lines, respectively). In cases B and C, we can compare the charge pumped per cycle with the function for $\Gamma(t)$; the square wave of C is slightly more conducive to transport than the sinusoidal wave of B.

We failed to pump integer numbers of electrons for any parameterization, and so were unable to generate a quantized current. At higher frequencies, current is roughly proportional to ω, but in the adiabatic limit the average charge pumped saturates for sufficiently small frequencies; the particular value of $\langle Q \rangle$ is determined in part by the choice of parameterizations. Realistically, thermal and shot noise prevent the generation of quantized current even with the best of parameterizations [78, 79].
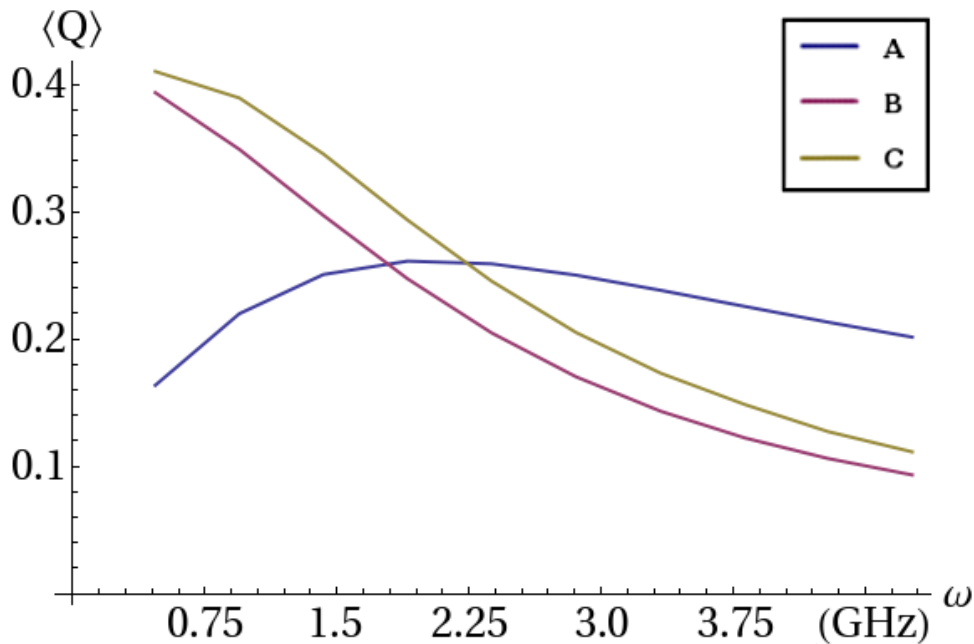
Average charge pumped per cycle versus pumping frequency for the parameterizations in Table 4.1, with the blue line corresponding to case A, the purple line corresponding to case B, and the tan line corresponding to case C. Scaling corresponds to $\Delta\epsilon = 1$ meV, $E_c = 1.5$ meV, $k_BT = 10^{-2}$ meV, and $\hbar\Gamma = 5 \times 10^{-3}$ meV, with $\delta\Gamma = 2 \times 10^{-3}$ meV$/\hbar$.

Figure 4.13: Charge Pumped Per Cycle for Various Parameterizations

With level degeneracy of a single dot broken by an in-plane magnetic field, it is possible to generate a completely polarized spin current comparable to the charge current in the degenerate case, where the spin polarization is

$$P_\sigma = \frac{N_\uparrow - N_\downarrow}{N_\uparrow + N_\downarrow}. \tag{4.9}$$

We allow $V_g(t)$ to oscillate about the energy required for the transition $(0,0) \to (0,\downarrow)$, $V_0 = \epsilon_\downarrow + U(1) - U(0)$. All electrons contributing to current have spin down, regardless of the pumping frequency, when the variation δV is smaller than the Zeeman energy. If $\delta V > \Delta\epsilon$, $V_g(t)$ will periodically match the energy required for spin up electrons to tunnel; in this case, the current will be completely polarized only for sufficiently small ω (Fig. 4.14).
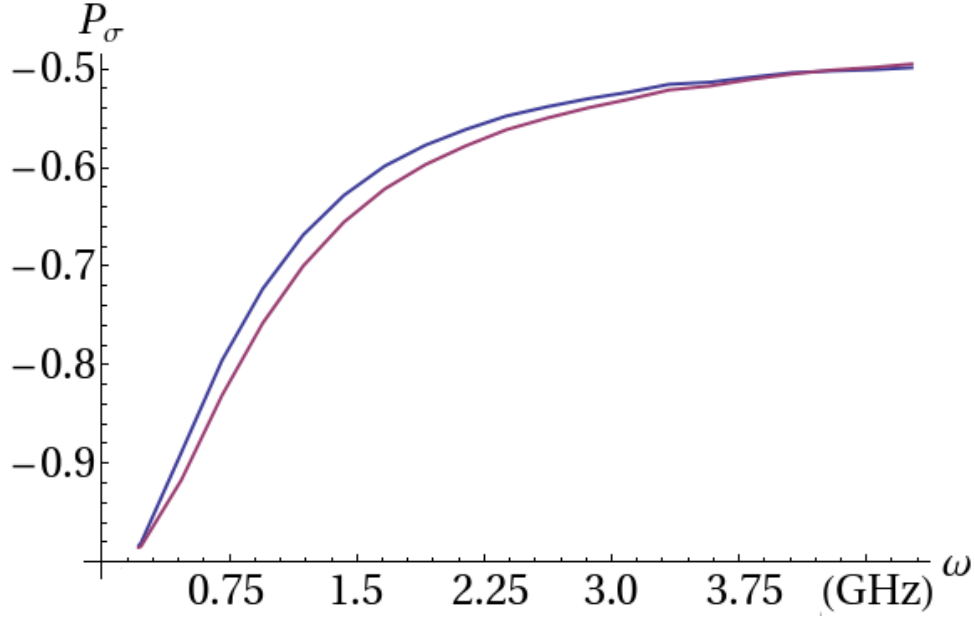
Polarization of the current through the left (blue) and right (purple) leads of the single dot when $\delta V > \Delta\epsilon$. When $\delta V < \Delta\epsilon$, current is completely polarized for any ω, $P_\sigma = -1$. Scaling corresponds to $\Delta\epsilon = 1$ meV, $E_c = 1.5$ meV, $k_B T = 10^{-2}$ meV, and $\hbar\Gamma = 5 \times 10^{-3}$ meV, with $\delta\Gamma = 2 \times 10^{-3}$ meV$/\hbar$.

Figure 4.14: Current Polarization Versus Pumping Frequency

Single Dot Spin Filter

The non-equilibrium behavior of the $(\uparrow, 0)$ and $(0, \downarrow)$ states could be exploited by using a single dot as a "spin turnstile, in a scaled down version of the DQD spin pump. To do so, the parameterizations for $V_g(t)$ and $\Gamma_{L(R)}(t)$ allow spin up electrons to move from left to right, and spin down electrons to move from right to left (Fig. 4.15),

$$V_g(t) = V_0 + \delta V (\cos(2\omega t - \pi/2) + \sin(\omega t + \pi/4)) \tag{4.10}$$

$$\Gamma_L(t) = \Gamma_0 - \delta\Gamma \text{sgn}(\cos(\omega t + \pi/4)) \tag{4.11}$$

$$\Gamma_R(t) = \Gamma_0 + \delta\Gamma \text{sgn}(\cos(\omega t + \pi/4)). \tag{4.12}$$

The change in angular momentum in each lead using these parameterizations is shown in Fig. 4.16. Oppositely polarized currents of equal magnitude exist for sufficiently high

59

frequency. The energy levels in the dot act as separate conduction channels, even while working in the wide band approximation. The advantage to this approach is the relative physical simplicity of the system; instead of four QPC and two gate voltage signals to control, one must only parameterize the signals for two QPCs and one "plunger". One could alternatively allow multiple conduction channels in the leads for better control over tunneling events. This would still require four parameterizations for $\Gamma^{l(r)}(t)$, but is still potentially useful when space is at a premium. Admittedly, the Markovian approximation used in deriving the rate equations is inapplicable when describing "fast" events, but the model can be interpreted as describing the statistical behavior of the system over the course of many cycles.
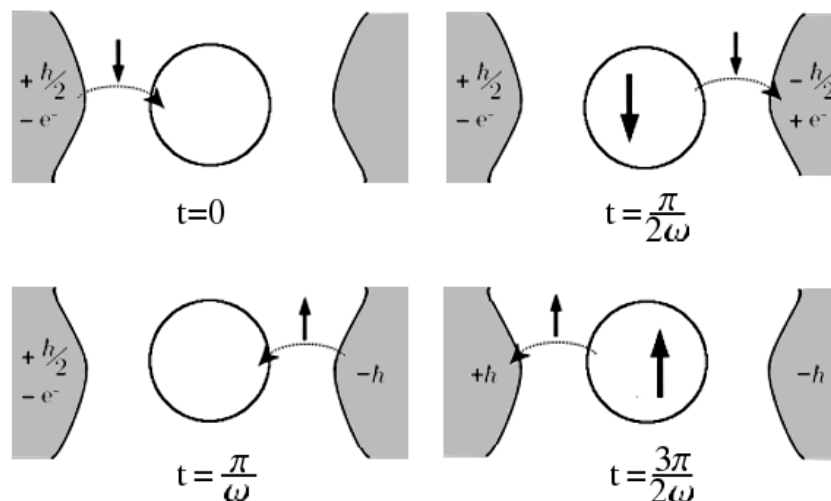
One cycle of the proposed single dot spin pump.

Figure 4.15: Spin Turnstile Schematic
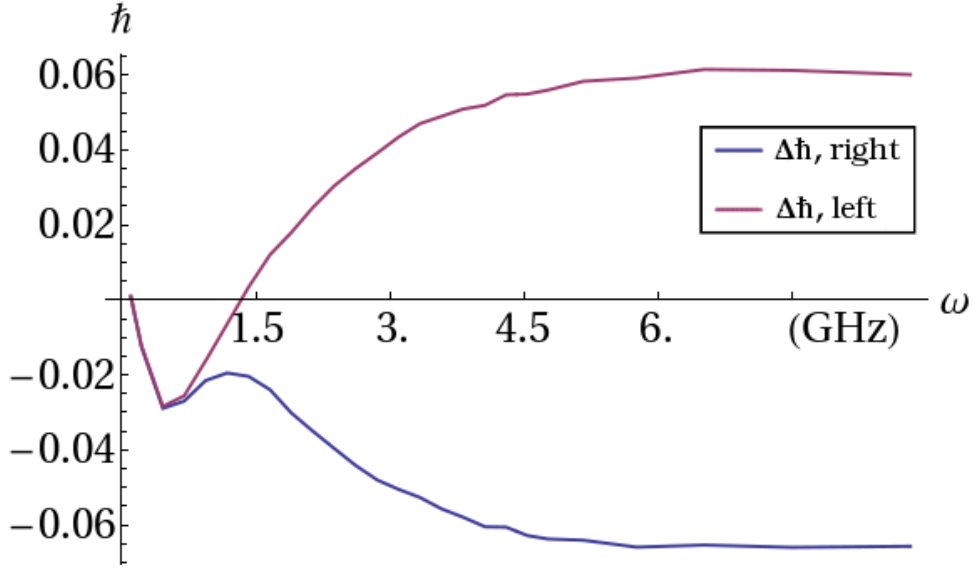
The change in spin for each lead for a single dot spin filter, plotted with respect to pumping frequency ω. For slower frequencies, the probability amplitudes of the states approach the equilibrium distribution, which favors the lower energy $(0,\downarrow)$ state over $(\uparrow,0)$; consequently, more spin down electrons contribute to current than spin up electrons. At higher frequencies, the excited states are able to participate in transport, and spin up and spin down electrons are pumped with roughly equal probability. Scaling corresponds to $\Delta\epsilon = 1$ meV, $E_c = 1.5$ meV, $k_B T = 10^{-2}$ meV, $\Delta E_Z = 0.05$ meV, and $\hbar\Gamma = 5 \times 10^{-3}$ meV.

Figure 4.16: Spin Transferred Between Leads for a Single Dot Turnstile

4.2.2 Double Dots

The easiest method of determining the bounds of the parameterizing functions is by visual inspection of the stability diagram. An appropriate choice of gate voltages should result in zero net charge current at the end of one complete cycle; when a magnetic field is applied, a non-zero net spin current should also be generated. Any cycle resulting in zero charge current would be centered at the intersection of four charge states in V_{g1}, V_{g2} phase space, as illustrated in Fig. 4.17, although the only cycles capable of generating a non-zero spin current lie off the main diagonal of $V_{g1} = V_{g2}$.[2] The direction of the spin

---

[2]For instance, consider path F in Fig. 4.17. Moving from state (00,00) to (01,00) adds one spin down electron from the left lead to dot one. Moving to (01,01) adds one spin down electron to dot two. (00,01) removes the electron from dot one, and returning to (00,00) removes the other spin down electron from dot two. No matter what parameterization is chosen, no spin up electrons are involved in the pump cycle; this would be acceptable if we were only looking to generate spin *polarized* current, but not if we want pure spin current.

current depends on the order of the $\Gamma(t)$ pulses. We also impose that QPCs controlling the dot-reservoir coupling should be pulsed such that only one lead is open at a time in order to limit cotunneling events.
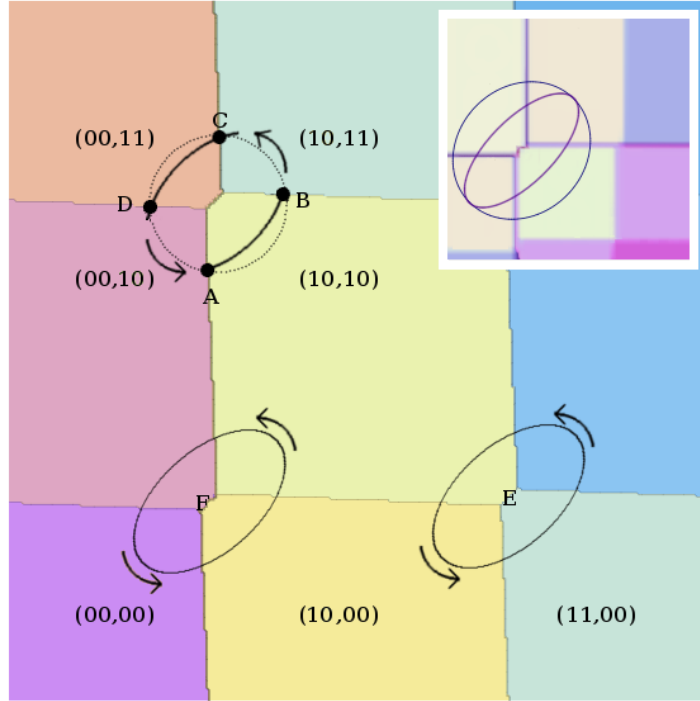
Each ellipse represents a parameterization for V_{g1} and V_{g2} which would result in zero net charge transfer between the reservoirs over the course of one complete cycle. Path $\{ABCD\}$ is the general path used for numerical calculations, while path E represents a parameterization which would result in a spin transfer opposite to that of $\{ABCD\}$. Path F would not transfer either charge or spin between the reservoirs. The inset shows the equilibrium probability distribution of the system in the region of path $\{ABCD\}$.

Figure 4.17: Possible Gate Voltage Parameterizations

Referring to Fig. 4.17, the points A, B, C, and D indicate where a transition occurs in the system. The specific events are sketched in Fig. 4.18, showing the spin of the electron being moved and the changes in both charge and spin for the reservoirs, for each step.
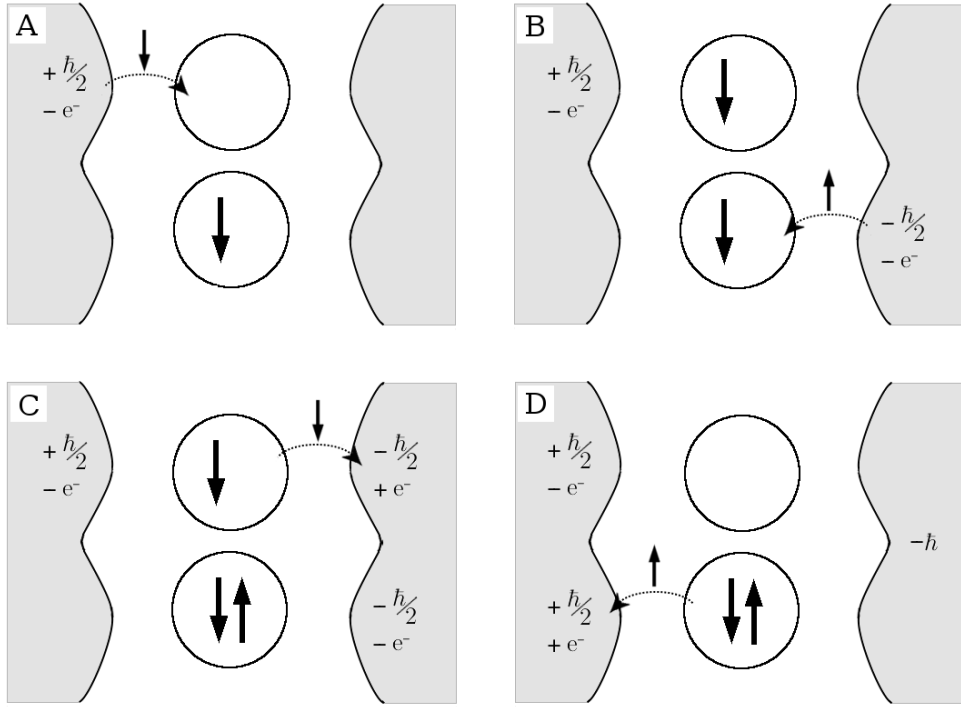
Events corresponding to points A, B, C and D in Fig. 4.17 are shown. For each transition, the total change in charge and spin of each reservoirs is shown as $\pm e^-$ and $\pm \hbar/2$.

Figure 4.18: Schematic of the Proposed Spin Pump Cycle

We first considered two single-level dots with very small electrostatic coupling, with no magnetic field present. Gate voltages were parameterized to form an ellipse in $V_{g1} - V_{g2}$ phase space, following the general form

$$V_{g1}(t) = h + a\cos(\omega t - \pi)\cos(\pi/4) - b\sin(\omega t - \pi)\sin(\pi/4) \qquad (4.13)$$

$$V_{g2}(t) = k + b\sin(\omega t - \pi)\cos(\pi/4) + a\cos(\omega t - \pi)\sin(\pi/4), \qquad (4.14)$$

where the additional phase of π is to ensure there are no immediate transitions from the $(0,0)$ state. Variables a and b are the major and minor axes of the ellipse, respectively, and (h, k) is the center of the ellipse. The leads were timed to coincide with conductance maxima, taking the form

$$\Gamma(t) = \Gamma + \delta\Gamma \text{sgn}(\cos(\omega t - t_0) - 1/\sqrt{2}). \qquad (4.15)$$

In Eq. (4.15), the value for t_0 depends on where in the cycle the particular dot-reservoir coupling should be increased, with $t_{0,A} < t_{0,B} < t_{0,C} < t_{0,D}$. The values for each t_0 were calculated numerically by substituting the gate voltages given by Eqs. (4.13-4.14) into Eq. (2.15).

The average charge pumped per cycle by both dots, $\langle Q \rangle = \langle Q_1 \rangle + \langle Q_2 \rangle$, was calculated for a range of frequencies and path eccentricities $\varepsilon = 0.5$ and $\varepsilon = 0.9$, and is shown in Figure 4.19. Paths with larger eccentricity admit more charge per cycle than circular paths, which can be attributed to the increased time spent in states $(1, 1)$ and $(0, 0)$, which are less energetically stable than the degenerate $(1, 0)$ and $(0, 1)$ states. As before, the average charge pumped per cycle increases with decreasing pumping frequency. When ω becomes too large or if the parameterizations for $\Gamma(t)$ are poorly chosen, charge accumulates on the dots and the system eventually saturates; after saturation no more charge can be pumped unless the system is allowed to discharge.
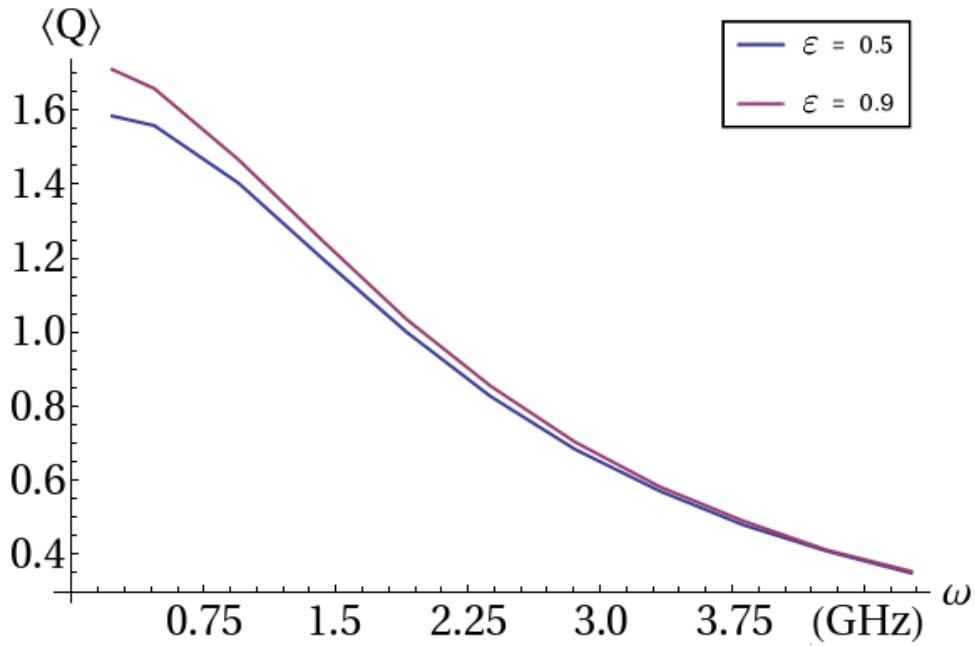
Average charge pumped per cycle is shown with respect to frequency. Each line corresponds to a different path eccentricity: $\varepsilon = 0.5$ in plotted in blue, and 0.9 in purple. More eccentric paths increase the total charge pumped, presumably since more time is spent in the less energetically stable $(0,0)$ and $(1,1)$ states. Scaling corresponds to $\Delta\epsilon = 1.2$ meV, $E_c = 1.237$ meV, $k_B T = 10^{-2}$ meV, and $\hbar\Gamma = 5 \times 10^{-3}$ meV, with $\hbar\delta\Gamma = 2 \times 10^{-3}$ meV. Average charge is in units of electrons.

Figure 4.19: Average Charge Pumped Per Cycle for Both Dots

The nondegenerate case is treated in a similar manner. It is useful to consider the equilibrium probability distribution of states in $V_{g1} - V_{g2}$ phase space (Fig. 4.11 and the inset in Fig. 4.17), in addition to the stability diagram, since the equilibrium probability distribution has several degenerate regions. These overlapping areas allow unwanted states to contribute to current, especially for slow pumping frequencies, making the choice of δV_g and eccentricity especially important.
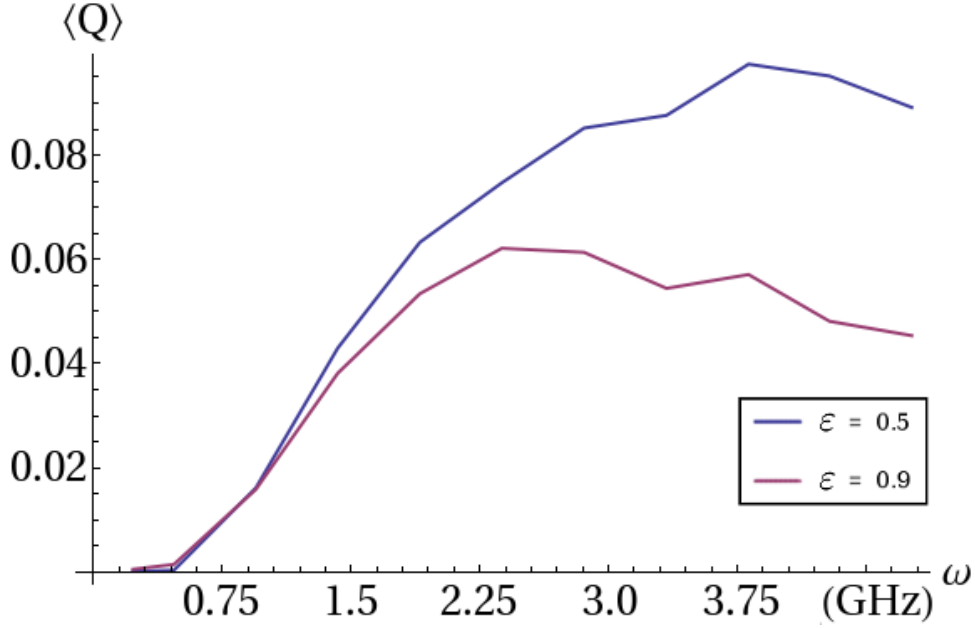
The total charge transferred between reservoirs per cycle in the nondegenerate system, plotted with respect to pumping frequency ω, for path eccentricities $\varepsilon = 0.5$ and 0.9, shown in blue and purple respectively. At higher pump frequencies, the system is not allowed to fully relax, allowing unwanted states to contribute to current. As before, the path with larger eccentricity permits more time to be spent in the less stable (00,10) and (10,11) states, mitigating (though not completely resolving) the problem of charge accumulation on the dots at higher frequencies. Scaling corresponds to $\Delta\epsilon = 1.2$ meV, $E_c = 1.237$ meV, $\Delta E_Z = 0.05$ meV, $k_B T = 10^{-2}$ meV, and $\hbar\Gamma = 5 \times 10^{-3}$ meV, with $\hbar\delta\Gamma = 2 \times 10^{-3}$ meV. Charge is in units of electrons.

Figure 4.20: Charge Pumped Per Cycle

In Figure 4.20, the charge pumped between reservoirs per cycle is plotted with respect to pumping frequency for path eccentricities $\varepsilon = 0.5$ (blue line) and $\varepsilon = 0.9$ (purple line). For sufficiently slow frequencies and well chosen $\Gamma(t)$, charge does not accumulate on the dot. Higher frequencies do not allow the states to relax, increasing the probability that an electron will either become trapped in the dots or contribute to a small, non-zero charge current. As in the nondegenerate case, the path with larger eccentricity permits more time to be spent in the less stable (00,10) and (10,11) states, mitigating (though not completely resolving) the problem of charge accumulation on the dots at higher frequencies. We illustrate this further in Fig. 4.21 by plotting the charge accumulated on dot 1 (dashed lines) and charge pumped by dot 1(solid lines) with respect to frequency, for eccentricities $\varepsilon = 0.5$ (blue data) and 0.9 (purple data). Charge pumped was found

by integrating the current through the right lead with respect to time over one cycle, and charge accumulated was calculated using Eq. (3.22). For $\varepsilon = 0.5$, the accumulated charge appears to overtake the pumped charge around $\omega = 22$ GHz; here, we can infer that the left lead has a larger current than the right lead, owing to the persistence of state (10,10) when approaching the transition (10,11)→(00,11) and the suppression of cotunneling events.
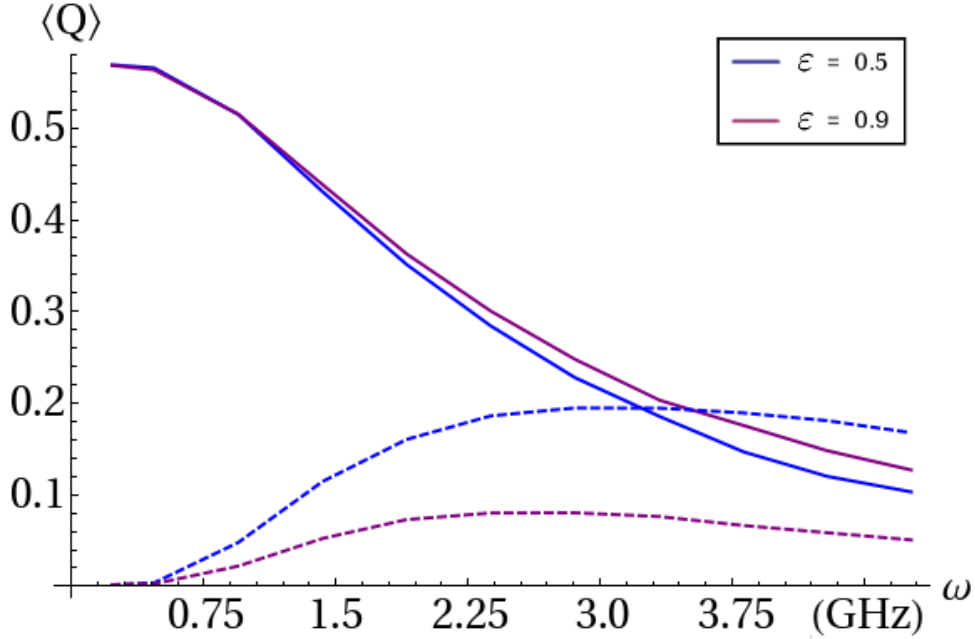
The charge pumped by and accumulated in dot 1 per cycle with respect to pumping frequency ω for path eccentricities $\varepsilon = 0.5$ and 0.9 (blue and purple lines, respectively). At lower frequencies there is no appreciable difference between the choice of parameterizations, though with increasing ω, $\varepsilon = 0.9$ again appears to be the better choice. Solid lines show the charge pumped by dot 1, and dashed lines show the charge accumulated on dot 1. Scaling corresponds to $\Delta\epsilon = 1.2$ meV, $E_c = 1.237$ meV, $\Delta E_Z = 0.05$ meV, $k_B T = 10^{-2}$ meV, and $\hbar\Gamma = 5 \times 10^{-3}$ meV, with $\hbar\delta\Gamma = 2 \times 10^{-3}$ meV. Charge is in units of electrons.

Figure 4.21: Accumulated Charge Per Cycle
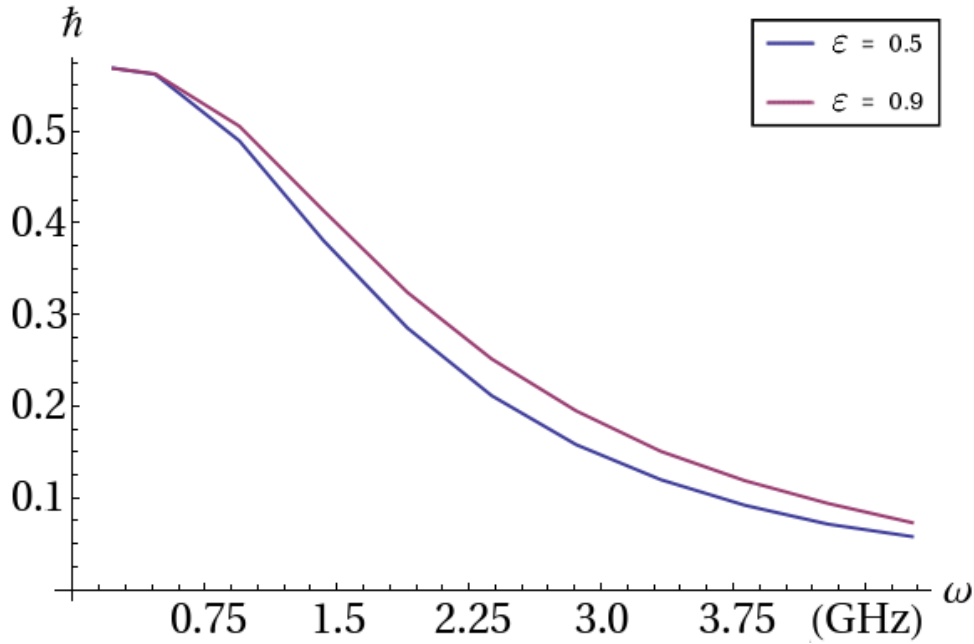
The average change in angular momentum per cycle between the two reservoirs with respect to pumping frequency ω, for $\varepsilon = 0.5$ (blue) and 0.9 (purple). Scaling corresponds to $\Delta\epsilon = 1.2$ meV, $E_c = 1.237$ meV, $\Delta E_Z = 0.05$ meV, $k_B T = 10^{-2}$ meV, and $\hbar\Gamma = 5 \times 10^{-3}$ meV, with $\hbar\delta\Gamma = 2 \times 10^{-3}$ meV.

Figure 4.22: Change in Angular Momentum Per Cycle

In Figure 4.22, the average spin transferred from the left to the right reservoir per cycle is shown with respect to pump frequency. The same mechanisms which prevent quantized charge pumping in the degenerate system also prevent quantized spin pumping here. At sufficiently slow frequencies, the differences in spin transferred arising from the specific parameterization of $V_{g1}(t)$ and $V_{g2}(t)$ are resolved, with both resulting in about 0.56 $\hbar$ per cycle with zero charge transfer.

4.3   Chapter Summary

In this Chapter, the equilibrium probability distributions for single and double quantum dot systems were obtained, and plotted in $V_{g1} - V_{g2}$ phase space. First, the probabilities, current and conductance for a single quantum dot with one available energy level were calculated both analytically and numerically in the stationary regime to evaluate

the accuracy of the numerical method used. The rate equations were then used to find probabilities, current, and conductance for double quantum dot systems in the stationary regime, with and without an applied magnetic field. A degenerate region between equivalent charge states, created by overlapping probabilities, was found when the equilibrium probability distribution was plotted in phase space. Conductance maxima were found to lie along the boundaries of the states' probabilities, not just the regions indicated in the stability diagram for the system.

The degenerate region was used to examine the limitations of the rate equation approach. Gate voltage was parameterized to follow $V_{g2}(t) = -V_{g1}(t)$, and the evolution of the probabilities for states $(0,1)$ and $(1,0)$ were plotted. The hysteretic nature of the system was apparent when the rate of change of the gate voltage, Δt^{-1} exceeded the relaxation rate of the dots, proportional to Γ. In this limit, the method breaks down, as the coarse graining used in deriving the rate equations is no longer valid.

The dynamic behavior of single and double quantum dot systems was then analyzed. For single dots with one available energy level, several different parameterizations of gate voltage and dot-reservoir coupling coefficients were used to calculate the charge and spin pumped over the course of ten cycles for a set pumping frequency, $\omega = 1.5$ GHz. The average charge and spin per cycle was calculated for a range of frequencies as well. The best signal was obtained for slow frequencies, when $\Gamma^l(t)$ and $\Gamma^r(t)$ were out of phase by $\pi/2$, and were timed to coincide with conductance maxima. A completely spin polarized current was generated when the gate voltage was allowed to oscillate about the requisite tunneling energy for a spin down electron; however, when the variation in V_g exceeded the Zeeman energy, it became possible for spin up electrons to contribute to current as well.

We suggested that the non-equilibrium behavior of the dot could be exploited in creating a single dot "spin turnstile, which acts as a scaled down version of the double quantum dot spin pump. By pumping the dot too fast for the system to equilibrate,

the spin up energy level can be used as a second conduction channel. A specific set of parameterizations for the left and right QPCs would allow spin polarized current to be generated in one direction only; i.e. spin down electrons can only move from the left to the right reservoir, and spin up electrons move from the right to the left reservoir. However, a more rigorous theoretical treatment is necessary to characterize the system, since by definition, the adiabatic approximation used here is inappropriate.

Finally, charge and spin transport were investigated for double quantum dot systems. Average charge pumped per cycle was plotted for a range of frequencies and for two different parameterizations of $V_{g1}(t)$ and $V_{g2}(t)$, where all $\Gamma(t)$ maxima were timed to coincide with the appropriate conductance maxima. Lower frequencies were again found to increase the average charge pumped per dot per cycle, as did more eccentric gate voltage parameterizations. The charge pumped per cycle for a system with an applied magnetic field was comparable to the case without an applied magnetic field. In both cases, as $\omega \to 0$, there was no net charge transfer between reservoirs, and a pure spin current was generated, although it was not quantized.

CHAPTER FIVE:
CONCLUDING REMARKS

We have simulated charge and spin pumping in single and double quantum dots in the linear response regime.

In Chapter 2, the construction of lateral quantum dots is reviewed, followed by a discussion of the Constant Interaction model. In this model, electron interactions are characterized by a constant capacitance C, which may be found using classical electrostatics. We then calculate the electrostatic charging energy of single and double quantum dot systems, E_c, and account for quantization by including a term to describe energy levels inside the dots. The "stability diagram" is introduced, showing the most stable charge configuration for a double quantum dot for any given set of gate voltages, V_{g1} and V_{g2}. Finally, we introduce the Zeeman effect, providing a mechanism with which to select electrons by their spin.

In Chapter 3, a quantum mechanical description of dot systems was given. Hamiltonians for both subsystems and their interaction were written in terms of creation and annihilation operators, followed by a calculation of transition rates using Fermi's golden rule in the wide band approximation. We then provided the general form of the rate equations, describing the time evolution of the probability amplitudes for the possible configurations of the dot system. Finally, expressions for current and conductance were given.

Chapter 4 contains the results of simulations based on the models presented in Chapters 2 and 3. First, stationary results for several different dot systems were presented.

For a one-dot, one-level system, analytic and numerical solutions to the rate equations were compared and found to agree, both with each other and with existing research.

Numerical calculations for more complex systems reveal that configurations with equivalent charge are equally probable for a certain range of gate voltages. The area of the probability overlap in $V_{g1} - V_{g2}$ phase space is dictated by the magnitude of the electrostatic coupling between dots. Switching behavior in the dots was investigated by varying the gate voltages to force transitions between states $(1, 0)$ and $(0, 1)$ only. For dots in series, switching represents a real tunneling event between dots. However, when considering parallel dots without a direct conduction channel, the hysteretic behavior indicates a second order tunneling event. By varying the rate at which gate voltage is changed, we found that the rate equations were not appropriate when the rate change of the gate voltage is on the order of the inverse dwell time of electrons in the dot. At this point, apparent memory effects influence the probability distribution of the states. Stationary current was calculated for all configurations, and conductance maxima were found to coincide with the boundaries between state probabilities in phase space, as opposed to the boundaries between configurations in the stability diagram. In addition, the electrostatic coupling between dots was found to suppress conduction in dot 1(2) when transport occurs in dot 2(1).

Determining the parameters of the degenerate region in the phase space of gate voltages could be advantageous when designing logic gates for use in nanoelectronics, for instance quantum dot cellular automata (QCA). A QCA cell is composed of capacitively coupled quantum dots whose charge configuration determines the polarization of the cell, ultimately representing binary 1 or 0. Interaction with neighboring cells is strictly Coulombic, with the polarization of one cell directly influencing the polarization of adjacent cells [80, 81]. Adiabatic switching allows for minimal energy dissipation in the system [82], potentially making QCA an attractive architecture for next generation electronic devices. Mapping the equilibrium probabilities of the cell (or set of cells) in phase space would be helpful in determining the gate voltages necessary to completely polarize

each cell. In addition, the time it takes to sweep the gate voltage (and thus ensure the state of the cell) could be estimated by the sweep rate and magnitude of dot coupling, which would prove enormously helpful in designing QCA latches (see, eg. Ref. [83]). The same concepts hold for other proposed devices, such as in QDs used as spin qubits [84], and could help explain unexpected features of charging as in Refs. [68, 69].

Dynamic results were then presented. First, charge pumping in a single, weakly coupled quantum dot was investigated. It was found that the parameterizations for gate voltage and left and right contacts significantly affected the amount of charge pumped between reservoirs per cycle. The amount of charge pumped generally increased with decreasing frequency, although with a particularly poor choice of parameterizations the opposite may occur: from Table 4.1, at 1.5 GHz, the set of parameterizations C led to an average current of 82.7 pA, whereas set A resulted in 59.8 pA per cycle. By comparison, pumping current in open quantum dots tended to be proportional to ω, where the charge pumped per cycle is independent of frequency [74]. This is since the dwell time of electrons in open dots is very short, making transport adiabatic for all but the fastest pumping frequencies. Using the same parameterizations and an in-plane magnetic field, completely spin polarized current of comparable magnitude was generated. However, when the variation in gate voltage was larger than ΔE_Z, completely polarized current was only generated when $\omega < \Gamma$; otherwise, excited states were able to contribute to the current using spin-up electrons.

The nonequilibrium behavior of a dot with Zeeman splitting was examined in the context of a single-dot "spin turnstile, acting as a scaled down version of a double quantum dot spin pump. Similar proposals exist for single dot spin pumps, using various combinations of parameterizations [23, 85, 86]. The effect was most pronounced when the pumping frequency was too fast for the system to relax. In this limit, the higher energy state $(\uparrow, 0)$ does not have time to decay, allowing current due to spin up electrons to roughly equal current due to spin down electrons. Our calculations show that almost zero charge current and small but non-zero spin current was produced at sufficiently high

frequencies. For a frequency of 253 MHz, we calculate the change in spin of the left reservoir to be -0.0005 $\hbar$, with an average of 0.0078 electrons accumulating on the dot per cycle. At 678 MHz, the change in spin for the left reservoir was 0.053 $\hbar$ with an average accumulation of 0.0065 electrons per cycle. As before, the spin pumped per cycle was subject to the choice of $V_g(t)$, $\Gamma^L(t)$, and $\Gamma^R(t)$. However, we caution that the approximations used in deriving the rate equations are not suitable for describing systems with rapidly varying coefficients.

Charge pumping in double quantum dot systems was then examined. A general form of parameterizations for each QPC and gate voltage was presented in Eqs. (4.13) and (4.15). The maxima of each Γ were timed to coincide with the cell boundaries of the stability diagram. The effect of the eccentricity of the ellipse formed by the gate voltages in $V_{g1} - V_{g2}$ phase space was examined by making calculations using $\varepsilon = 0.5$ and 0.9. The total charge pumped per cycle increased at low frequency and with larger eccentricity: at 478 MHz, for $\varepsilon = 0.5$, average current through the left lead of the top dot was 122 pA; for $\varepsilon = 0.9$, $\langle I_{L1} \rangle = 130.8$ pA. For larger eccentricities, more time was spent sweeping the less stable (0,0) and (1,1) states than the bistable (1,0) and (0,1) states, allowing more time for the system to relax.

When level degeneracy was broken with an applied magnetic field, the number of configurations with overlapping probabilities increased. The states' probabilities in phase space no longer directly corresponded to the regions in the stability diagram, limiting the choices of parameterizations for gate voltage and dot-reservoir coupling. The dimensions of the closed contour in phase space were chosen carefully to prevent the unnecessary inclusion of other stable charge states in the pumping cycle. The total charge pumped per cycle was similar to the results of the degenerate case: at 478 MHz, for both $\varepsilon = 0.5$ and 0.9, each dot transferred 0.59 electrons per cycle, with no accumulated charge. Both cases had zero total charge transfer between reservoirs per cycle. The spin transferred was comparable, at 0.59 $\hbar$ per cycle.

Ultimately, we were unable to generate either quantized charge or spin current, but do not attribute this to any particular failings of the model. Rather, it seems the energy scales required to stay in the linear, incoherent, sequential tunneling regime run close together, making it difficult for any one mechanism to dominate transport. Our results were similar to those already found in the literature (for instance, [24, 25, 70, 77]), even when more sophisticated approaches were used, suggesting that noise is inherent in the system. Our calculations were made at $T = 100$ mK, with finite dwell times, and less than perfect transmission through barriers. The issues of shot noise, thermal noise, rectification, and other sources of noise are addressed at length elsewhere [13, 87, 88, 89, 90, 91, 92, 93, 94]. It should be noted that schemes resulting in quantized current tend do so in the limit $T \to 0$ [23, 95, 96], although the signal can be improved by careful choice of pumping parameters [95, 96, 97, 98, 99, 100]. Given the encouraging results at very low frequency, future work should focus on frequencies less than 500 MHz.

APPENDIX A:
ELECTROSTATIC ENERGY

We consider the dot configuration as a system of N conductors. Classically, there exists a capacitance c_{ij} between conductors i and j, which has stored charge q_{ij},

$$q_{ij} = c_{ij}(v_i - v_j), \tag{A.1}$$

so that the total charge Q_i on i is just the sum of all the charges on all the capacitors connected to i:

$$Q_i = \sum_{j=1}^{N} q_{ij} = \sum_{j=1}^{N} c_{ij}(v_i - v_j). \tag{A.2}$$

Voltage sources - gates and reservoirs - are treated as nodes with large capacitance and charge. For the entire system, Eq. (A.2) generalizes to

$$\vec{Q} = \mathbf{C}\vec{V}, \tag{A.3}$$

with elements of the capacitance matrix $\mathbf{C}$ given by

$$
\begin{aligned}
\mathrm{C}_{ii} &= \sum_{j=0, j \neq i} c_{ij} \\
\mathrm{C}_{ij} &= c_{ji} = -c_{ij}.
\end{aligned}
\tag{A.4}
$$

The matrix form of Eq. (A.3) is then

$$
\begin{pmatrix} \vec{Q}_c \\ \vec{Q}_v \end{pmatrix} = \begin{pmatrix} \mathrm{C}_{cc} & \mathrm{C}_{cv} \\ \mathrm{C}_{vc} & \mathrm{C}_{vv} \end{pmatrix} \begin{pmatrix} \vec{V}_c \\ \vec{V}_v \end{pmatrix}, \tag{A.5}
$$

where the subscript c indicates the node of a charge source and v indicates the node of a voltage source. It follows that voltage on a charge node is found by

$$\vec{V}_c = \mathrm{C}_{cc}^{-1}(Q_c - \mathrm{C}_{cv}\vec{V}_v). \tag{A.6}$$

Electrostatic energy may be found as usual by

$$U = \frac{1}{2}\vec{V}\mathbf{C}\vec{V} = \frac{1}{2}\vec{V}\vec{Q} = \frac{1}{2}\vec{Q}\mathbf{C}^{-1}\vec{Q}. \tag{A.7}$$

A.1 Calculations for Single Quantum Dots
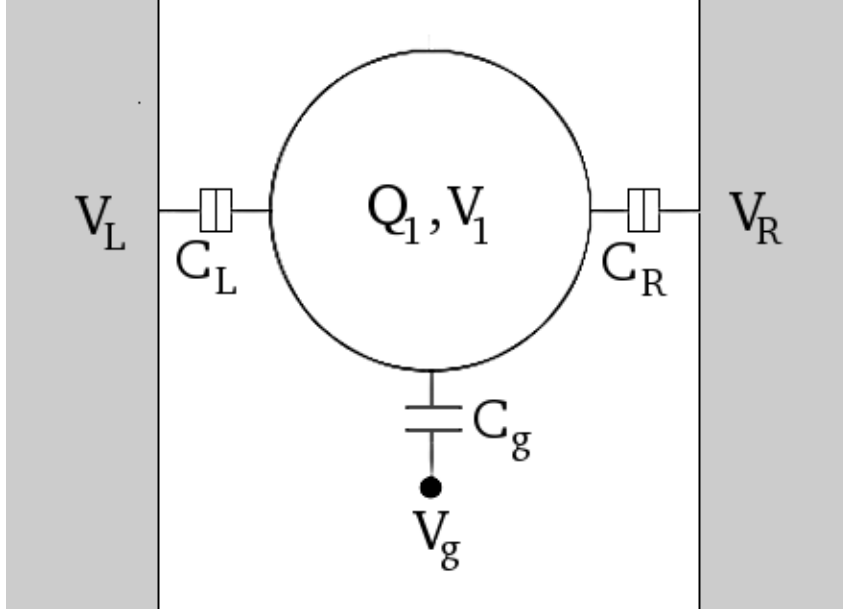
A schematic illustration of a quantum dot as a system of capacitors, charges, and voltages. "Nodes" are the points at which the dot is connected to external voltages sources. In this example, the nodes are between the dot and the right and left reservoirs, and between the dot and the gate voltage.

Figure A.1: The QD as a System of Conductors

Let Q_c represent the total charge on the dot, and Q_1 represent charge from just the electrons on the dot. Referring to Fig. A.1 and using Eq. (A.3),

$$\begin{aligned} Q_c &= C_1 V_1 \\ &= Q_1 + C_L V_L + C_R V_R + C_g V_g. \end{aligned} \tag{A.8}$$

$\mathbf{C}$ has just one element, C_1, where

$$C_1 = C_L + C_R + C_g. \tag{A.9}$$

By substitution, the charge of the electrons on the dot can be found as

$$Q_1 = C_L(V_1 - V_L) + C_R(V_1 - V_R) + C_g(V_1 - V_g). \tag{A.10}$$

Using Eq. (A.10) in Eq. (A.7), and letting $Q_1 = -N|e|$, where e is individual electron charge and N the number of electrons on the dot,

$$
\begin{aligned}
U &= \frac{1}{2}\vec{Q}\mathbf{C}^{-1}\vec{Q} \\
&= \frac{(Q_1 + C_L V_L + C_R V_R + C_g V_g)^2}{2\mathbf{C}}
\end{aligned} \tag{A.11}
$$

We make the substitution $Q_1 = -N_1|e|$, and set $V_L = V_R = 0$ with respect to V_1. Hence the above can be simplified as

$$U = \frac{N_1^2|e|^2}{2C} - \frac{N_1|e|C_g V_g}{C} + \frac{C_g^2 V_g^2}{2C}. \tag{A.12}$$

The charging energy can be obtained as in Sec. 2.2:

$$
\begin{aligned}
E_c &= \frac{(N_1+1)^2|e|^2}{2C} - \frac{(N_1+1)|e|C_g V_g}{C} + \frac{C_g^2 V_g^2}{2C} \\
&\quad \frac{N_1^2|e|^2}{2C} - \frac{N_1|e|C_g V_g}{C} + \frac{C_g^2 V_g^2}{2C} \\
&= \left(N + \frac{1}{2}\right)\frac{|e|^2}{C} - \frac{|e|C_g V_g}{C}.
\end{aligned} \tag{A.13}
$$

A.2   Calculations for Parallel DQDs

We start by designating the total charge on the top dot $Q_{c1} = C_1 V_1$ and the total charge on the bottom dot $Q_{c2} = C_2 V_2$. Referring to Fig. 2.2, the total capacitances for each dot

are

$$C_{1(2)} = C_L + C_R + C_{g1(2)} + C_m, \tag{A.14}$$

so that the total charge on each dot is

$$Q_{c1(2)} = Q_{1(2)} + C_{L1(2)}V_L + C_{R1(2)}V_R + C_{g1(2)}V_{g1(2)} + C_m V_{2(1)}. \tag{A.15}$$

The above can be simplified by setting $V_L = V_R = 0$, which is the case when there is no applied bias. Electron charge on each dot is then

$$Q_{1(2)} = C_{L1(2)}V_{1(2)} + C_{R1(2)}V_{1(2)} + C_{g1(2)}(V_{1(2)} - V_{g1(2)}) + C_m(V_{1(2)} - V_{2(1)}). \tag{A.16}$$

With some algebra V_1 and V_2 can be found:

$$\begin{pmatrix} V_1 \\ V_2 \end{pmatrix} = \frac{1}{C_1 C_2 - C_m^2} \begin{pmatrix} C_2 & C_m \\ C_m & C_1 \end{pmatrix} \begin{pmatrix} Q_1 + C_{g1}V_{g1} \\ Q_2 + C_{g2}V_{g2} \end{pmatrix}. \tag{A.17}$$

Multiplying the above out and using the definitions of electrostatic charging energy,

$$E_{c1(2)} = |e|^2 \frac{C_{2(1)}}{C_1 C_2 - C_m^2} \qquad E_{cm} = |e|^2 \frac{C_m}{C_1 C_2 - C_m^2}, \tag{A.18}$$

the voltages are

$$V_{1(2)} = -\frac{1}{|e|} \left[E_{c1(2)} \left(N_{1(2)} - \frac{C_{g1(2)}V_{g1(2)}}{|e|} \right) + E_{cm} \left(N_{2(1)} - \frac{C_{g2(1)}V_{g2(1)}}{|e|} \right) \right]. \tag{A.19}$$

Finally, from Eq. (A.7),

$$\begin{aligned} U &= \frac{E_{c1}}{2} \left(N_1^2 - \frac{N_1 C_{g1}V_{g1}}{|e|} \right) + \frac{E_{c2}}{2} \left(N_2^2 - \frac{N_2 C_{g2}V_{g2}}{|e|} \right) \\ &+ \frac{E_{cm}}{2} \left[2N_1 N_2 - \frac{1}{|e|}(N_1 C_{g2}V_{g2} + N_2 C_{g1}V_{g1}) \right]. \end{aligned} \tag{A.20}$$

APPENDIX B:
NUMERICAL INTEGRATION ALGORITHMS

The rate equations given by Eq. (3.11) form a set of stiff differential equations; solutions do not vary at a uniform rate and hence no single integration time scale is adequate. For instance, in Fig. 4.1, the numerical step size prior to $V_g = 2.44$ can be relatively large and still generate an accurate solution, but must be small between $V_g = 2.44$ to 2.56 to maintain stability. Rather than sacrificing either accuracy or stability, one may choose an algorithm which adjusts the step size with each iteration.

The probabilities and currents of various QD systems were found numerically using Mathematica's differential equation solving package, `NDSolve`. Unless otherwise specified by the user, `NDSolve` uses the LSODA routine, which is a combination of predictor-corrector and backwards differentiation methods [101]. In this technique, the "stiffness" of the equations is evaluated and step size is adjusted accordingly, thereby reducing total computation time while still returning useful solutions.

B.1 Adams-Bashforth-Moulton Algorithm

A more detailed discussion of the algorithms used may be found in Ref. [102].

In general, solutions to differential equations can be approximated by a polynomial function $y(x)$,

$$y(x) = y_n + \int_{x_n}^{x} f(x', y)dx',$$
(B.1)

in which the $(n + 1)^{th}$ numerical value is generated by assuming that $y(x)$ also passes through several previous points $x_n, x_{n-1}, ...$ Evaluation at $x = x_{n+1}$ is given by

$$y_{n+1} = y_n + h(\beta_0 y'_{n+1} + \beta_1 y'_n + \beta_2 y'_{n-1} + \beta_3 y'_{n-2} + ...)$$
(B.2)

where $y'_n = f(x_n, y_n)$, and β_0 is non-zero for implicit methods.

Accurate solutions can be found explicitly for small step size h; for larger h stability is sacrificed. Alternatively, y can be found implicitly, so that the algorithm is stable for

all h, albeit with some loss of accuracy with increasing h . The rate equations generated with Eq. (3.11) are unquestionably stiff, so that the size of h must vary from one iteration to the next. Hence stability can only be assured if an implicit method is used.

To generate solutions, a guess is made for the value of y_{n+1}, which is inserted into the right-hand side of Eq. (B.2) to generate the next value of y_{n+1}. The new value is reinserted into the equation, and the process is repeated until the maximum allowed number of steps has been reached. The initial guess – generated with a predictor step – is based on an explicit form of y_{n+1}, and subsequent iterations comprise corrector steps.

In the Adams-Bashforth-Moulton algorithm (ABM), values for y_{n+1} are generated with the Adams-Bashforth predictor,

$$y_{n+1} = y_n + \frac{h}{12}(23y'_n - 16y'_{n-1} + 5y'_{n-2}) + O(h^4), \tag{B.3}$$

and the Adams-Moulton corrector,

$$y_{n+1} = y_n + \frac{h}{12}(5y'_{n+1} + 8y'_n - 5y'_{n-1}) + O(h^4). \tag{B.4}$$

Both Eqs. (B.3) and (B.4) are given to third order. The step size h is appropriate if

$$\mid h\,\frac{\partial f(x,y)}{\partial y}\mid < 1 \tag{B.5}$$

over the integration region.

APPENDIX C:
FORMULATION OF THE RATE EQUATIONS

In this appendix, we derive a set of rate equations for the system illustrated in Fig. 2.2, where each dot has one available energy level. In this case, the dot Hamiltonian [Eq. (3.3)] may be written as

$$H_D = U(N_1, N_2) + \epsilon_1 a_1^\dagger a_1 + \epsilon_2 a_2^\dagger a_2, \tag{C.1}$$

the reservoir Hamiltonian, from Eq. (3.2) is

$$H_R = \sum_k (\xi_{kl} c_{kl}^\dagger c_{kl} + \xi_{kr} c_{kr}^\dagger c_{kr}), \tag{C.2}$$

and the interaction term, from Eq. (3.4) is

$$H_I = T \sum_k \{(c_{kl}^\dagger a_1 + c.c.) + (c_{kl}^\dagger a_2 + c.c.) + (c_{kr}^\dagger a_1 + c.c.) + (c_{kr}^\dagger a_2 + c.c.)\}. \tag{C.3}$$

We define

$$\nu = \sum_k (c_{kl} + c_{kr}) \qquad \nu^\dagger = \sum_k (c_{kl}^\dagger + c_{kr}^\dagger). \tag{C.4}$$

In the subspace of the dot, let

$$H = H_D + H_I. \tag{C.5}$$

The Hamiltonian can alternatively be expressed in matrix form

$$H_D = \begin{pmatrix} 0 & 0 & 0 & 0 \\ 0 & E_{10} & 0 & 0 \\ 0 & 0 & E_{01} & 0 \\ 0 & 0 & 0 & E_{11} \end{pmatrix}. \tag{C.6}$$

In the above, $E_{10} = \epsilon_1 + U(1,0)$, $E_{01} = \epsilon_2 + U(0,1)$, and $E_{11} = \epsilon_1 + \epsilon_2 + U(1,1)$.

$$H_I = \begin{pmatrix} 0 & V_{12} & V_{13} & 0 \\ V_{21} & 0 & 0 & U_{24} \\ V_{31} & 0 & 0 & U_{34} \\ 0 & U_{42} & U_{43} & 0 \end{pmatrix}. \tag{C.7}$$

Here,

$$\begin{aligned}
V_{12} &= \mathrm{T} \sum_k (c_{kl}^\dagger + c_{kr}^\dagger) a_1 & V_{13} &= \mathrm{T} \sum_k (c_{kl}^\dagger + c_{kr}^\dagger) a_2 \\
V_{21} &= \mathrm{T} \sum_k (c_{kl} + c_{kr}) a_1^\dagger & V_{31} &= \mathrm{T} \sum_k (c_{kl} + c_{kr}) a_2^\dagger \\
U_{24} &= \mathrm{T} \sum_k (c_{kl}^\dagger + c_{kr}^\dagger) a_2 & U_{34} &= \mathrm{T} \sum_k (c_{kl}^\dagger + c_{kr}^\dagger) a_1 \\
U_{42} &= \mathrm{T} \sum_k (c_{kl} + c_{kr}) a_2^\dagger & U_{43} &= \mathrm{T} \sum_k (c_{kl} + c_{kr}) a_1^\dagger.
\end{aligned} \tag{C.8}$$

In the wide band approximation, T is a coefficient describing the magnitude of the dot-reservoir interaction, and can be taken as a small constant. We define

$$\tilde{E}_1 = \begin{pmatrix} E_{10} & 0 \\ 0 & E_{01} \end{pmatrix} \tag{C.9}$$

such that Eqs.(C.6) and (C.7) may take the form

$$H_D = \begin{pmatrix} 0 & 0 & 0 \\ 0 & \tilde{E}_1 & 0 \\ 0 & 0 & E_{11} \end{pmatrix} \tag{C.10}$$

and

$$H_I = \begin{pmatrix} 0 & V^\dagger & 0 \\ V & 0 & U^\dagger \\ 0 & U & 0 \end{pmatrix}. \tag{C.11}$$

In H_D we have rewritten V_{12} and V_{13} together as $V^\dagger$, and similarly for $U^\dagger$, U, and V.

To obtain the master equations, we first define the basis of the reservoir subsystem, $\{|r\rangle\}$ and those of the dot subsystem, $\{|n_1, n_2\rangle = \{|00\rangle, |10\rangle, |01\rangle, |11\rangle\}\}$, or alternately $\{|n_1, n_2\rangle = \{|1\rangle, |2\rangle, |3\rangle, |4\rangle\}\}$. The full density operator in the interaction picture is

$$\rho_I(t) = \sum e^{i(H_D + H_R)t/\hbar} |n_1, n_2; r\rangle \langle n_1, n_2; r| e^{-i(H_D + H_R)t/\hbar}. \tag{C.12}$$

Time evolution is governed by the von Neumann equation,

$$i\hbar\dot{\rho}_I(t) = [V(t)_I, \rho_I(t)], \tag{C.13}$$

or in integral form,

$$\rho_I(t) = \rho_I(0) - \frac{i}{\hbar} \int_0^t [V(t')_I, \rho_I(t')]dt'. \tag{C.14}$$

By back substitution, we find the useful general form

$$\dot{\rho}_I(t) = \frac{i}{\hbar}[V(t)_I, \rho_I(0)] - \frac{1}{\hbar^2} \int_0^t [V(t)_I, [V(t')_I, \rho_I(t')]]dt'. \tag{C.15}$$

Here we introduce the reduced density operator, which allows us to neglect the unobserved reservoir subsystem in subsequent calculations:

$$\rho_I(R, t) = \text{tr}_R \rho_I(t). \tag{C.16}$$

Here, tr_R indicates a trace over the reservoir states. In terms of the reduced system, Eq. (C.15) now reads

$$\dot{\rho}_I(R, t) = \frac{i}{\hbar}[V(t)_I, \rho_I(0)] - \frac{1}{\hbar^2} \int_0^t \text{tr}_R[V(t)_I, [V(t')_I, \rho_I(t')]]dt'. \tag{C.17}$$

Calculations can be further simplified by replacing $\rho_{RI}(t)$ with $\rho_{RI}(0)$ in the expression for $\rho_I(t)$. This assumes the "condition of irreversibly holds, i.e., that the reservoir subsystem will remain in thermal equilibrium regardless of any interaction with the dot subsystem, since any change to the reservoir will dissipate very quickly. In what is known as the Markov approximation, the evolution of the dot subsystem is also independent of past behavior for time intervals longer than the characteristic relaxation time of the dot.

We define the transition rate from dot state m to dot state n as

$$W_{mn} = \frac{2\pi}{\hbar} \sum_{kk'} |\langle mk|V|nk'\rangle|^2 \langle k'|\rho(0)_R|k'\rangle \delta(\xi_{k'} - \xi_k - \hbar\omega_{mn}). \tag{C.18}$$

The thermal average over the reservoir takes the form

$$
\begin{aligned}
\langle \nu\nu^\dagger \rangle &= \sum_{k,k'} \langle (c_{kl} + c_{kr})(c_{kl}^\dagger + c_{kr}^\dagger) \rangle \\
&= \sum_{k,k'} [\langle c_{kl} c_{kl}^\dagger \rangle + \langle c_{kr} c_{kr}^\dagger \rangle] \\
&= (1 - f(\xi_{kl}))\delta_{k,k'} + (1 - f(\xi_{kr}))\delta_{k,k'} \tag{C.19} \\
\langle \nu^\dagger\nu \rangle &= \sum_{k,k'} \langle (c_{kl}^\dagger + c_{kr}^\dagger)(c_{kl} + c_{kr}) \rangle \\
&= \sum_{k,k'} [\langle c_{kl}^\dagger c_{kl} \rangle + \langle c_{kr}^\dagger c_{kr} \rangle] \\
&= f(\xi_{kl})\delta_{k,k'} + f(\xi_{kr})\delta_{k,k'}. \tag{C.20}
\end{aligned}
$$

For an unbiased system, we may let $f(\xi_{kl}) = f(\xi_{kr})$ so that

$$\langle \nu\nu^\dagger \rangle = 2(1 - f(\xi_k))\delta_{k,k'} \tag{C.21}$$

$$\langle \nu^\dagger\nu \rangle = 2f(\xi_k)\delta_{k,k'}. \tag{C.22}$$

The rate equations may be written as a set of coupled equations,

$$\frac{\partial \rho_i(t)}{\partial t}\bigg|_{mm} = \sum_{n \neq m} \rho(t)_{nn} W_{mn} - \sum_{n \neq m} \rho(t)_{mm} W_{nm}. \tag{C.23}$$

88

As an example, $\dot{\rho}(t)_{11}$ is

$$\dot{\rho}(t)_{11} = \rho(t)_{22}W_{12} + \rho(t)_{33}W_{12} + \rho(t)_{44}W_{14} - \rho(t)_{11}(W_{21} + W_{31} + W_{41}). \qquad \text{(C.24)}$$

The coefficients in Eq. (C.24) are calculated by substituting Eq. (C.21) into Eq. (C.18), and taking $\hbar\omega_{mn} = \epsilon_m + U(N_m) - (\epsilon_n + U(N_n)) = \Delta\epsilon + E_c$:

$$
\begin{aligned}
W_{12} &= \frac{2\pi T^2}{\hbar}\sum_{kk'}|\langle 1|a_1|2\rangle\langle k|\nu^\dagger|k'\rangle|^2\langle k'|\rho(0)_R|k'\rangle\delta(\xi_k - \{\epsilon_1 + U(1,0) - U(0,0)\}) \\
&= \frac{2\pi T^2}{\hbar}(2f(\epsilon_1 + U(1,0) - U(0,0))) \\
W_{21} &= \frac{2\pi T^2}{\hbar}(2\{1 - f(\epsilon_1 + U(1,0) - U(0,0))\}) \qquad\qquad\text{(C.25)} \\
W_{13} &= \frac{2\pi T^2}{\hbar}\sum_{kk'}|\langle 1|a_2|3\rangle\langle k|\nu^\dagger|k'\rangle|^2\langle k'|\rho(0)_R|k'\rangle\delta(\xi_k - \{\epsilon_2 + U(0,1) - U(0,0)\}) \\
&= \frac{2\pi T^2}{\hbar}(2f(\epsilon_2 + U(0,1) - U(0,0))) \\
W_{31} &= \frac{2\pi T^2}{\hbar}(2\{1 - f(\epsilon_2 + U(0,1) - U(0,0))\} \qquad\qquad\text{(C.26)} \\
W_{14} &= \frac{2\pi T^2}{\hbar}\sum_{kk'}|\langle 1|0|4\rangle\langle k|0|k'\rangle|^2\langle k'|\rho(0)_R|k'\rangle\delta(\xi_k - \{\epsilon_2 + \epsilon_1 + U(1,1) - U(0,0)\}) \\
&= 0 \\
W_{41} &= 0. \qquad\qquad\qquad\qquad\qquad\qquad\qquad\qquad\qquad\qquad\text{(C.27)}
\end{aligned}
$$

$$\text{(C.28)}$$

We replace the term $2\pi T^2/\hbar$ with Γ, so that Eq. (C.24) becomes

$$
\begin{aligned}
\dot{\rho}(t)_{11} &= \rho(t)_{22}[2\Gamma f(\epsilon_1 + U(1,0) - U(0,0))] \\
&\quad + \rho(t)_{33}[2\Gamma f(\epsilon_2 + U(0,2) - U(0,0))] \\
&\quad - \rho(t)_{11}[2\Gamma\{(1 - f(\epsilon_1 + U(1,0) - U(0,0)) \\
&\qquad\qquad + (1 - f(\epsilon_2 + U(0,1) - U(0,0)))\}]. \qquad\text{(C.29)}
\end{aligned}
$$

The probability of each state is found using the projection operator and taking the trace over the density matrix. For example,

$$P(0,0) = \text{tr}(\mathbb{P}_{00}\rho(t)), \tag{C.30}$$

where

$$\mathbb{P}_{00} = \begin{pmatrix} 1 & 0 & 0 & 0 \\ 0 & 0 & 0 & 0 \\ 0 & 0 & 0 & 0 \\ 0 & 0 & 0 & 0 \end{pmatrix}. \tag{C.31}$$

C.1 Second Order Interactions

When the dots are not weakly coupled to the reservoirs, it is necessary to include second order terms in the rate equations to account for cotunneling events. To do this, we could continue the perturbative expansion in Eq. (C.15), or alternatively, construct a Hamiltonian describing only higher order phenomena. This can be accomplished using the Schrieffer-Wolff similarity transform,

$$\begin{aligned} H' &= e^{-S}He^{S} \\ &= H + [H,S] - \frac{1}{2}[S,[H,S]] + O(\text{T}^3). \end{aligned} \tag{C.32}$$

where S is on the order of T, $S = -S^{\dagger}$, and takes the form

$$S = \begin{pmatrix} 0 & A & B \\ -A^{\dagger} & 0 & C \\ -B^{\dagger} & -C^{\dagger} & 0 \end{pmatrix}. \tag{C.33}$$

Setting $H_I = [S, H_D]$ in Eq. (C.32), the transformed Hamiltonian is

$$H' = H_D + \frac{1}{2} \begin{pmatrix} -V^\dagger A^\dagger - AV & 0 & V^\dagger C - AU^\dagger \\ 0 & VA - U^\dagger C^\dagger + A^\dagger V^\dagger - CU & 0 \\ -UA^\dagger + C^\dagger V & 0 & UC + C^\dagger U^\dagger \end{pmatrix}, \quad \text{(C.34)}$$

where the elements of S were found to be

$$B^\dagger = 0 \qquad B = 0$$

$$A^\dagger = \tilde{E}_1^{-1} V \qquad A = V^\dagger \tilde{E}_1^{-1}$$

$$C^\dagger = U(E_{11} - \tilde{E}_1)^{-1} \qquad C = (E_{11} - \tilde{E}_1)^{-1} U^\dagger. \quad \text{(C.35)}$$

With a bit of algebra, the Hamiltonian may be written as shown in Fig. C.1. Each term in the transformed Hamiltonian describes a cotunneling event. States $|1\rangle$ and $|4\rangle$ are decoupled from states $|2\rangle$ and $|3\rangle$, It remains only to calculate the coefficients from Eq. (C.18) and apply the results to Eq. (C.23).

$$H = \begin{pmatrix} -T^2\nu^\dagger\nu\left(\frac{a_1 a_1^\dagger}{E_{10}} + \frac{a_2 a_2^\dagger}{E_{01}}\right) & 0 & 0 & \frac{1}{2}T^2\nu^\dagger\nu^\dagger\left(\frac{(2E_{10}-E_{11})}{E_{10}(E_{11}-E_{10})}a_1 a_2 + \frac{(2E_{01}-E_{11})}{E_{01}(E_{11}-E_{01})}a_2 a_1\right) \\[2ex] 0 & E_{10} + T^2\nu\nu^\dagger\left(\frac{a_1^\dagger a_1}{E_{10}}\right) - T^2\nu^\dagger\nu\left(\frac{a_2 a_2^\dagger}{E_{11}-E_{10}}\right) & T^2\nu\nu^\dagger a_1^\dagger a_2\left(\frac{E_{10}+E_{01}}{2E_{10}E_{01}}\right) - T^2\nu^\dagger\nu a_2 a_1^\dagger\left(\frac{2E_{11}-E_{10}-E_{01}}{2(E_{11}-E_{10})(E_{11}-E_{01})}\right) & 0 \\[2ex] 0 & T^2\nu\nu^\dagger\left(a_2^\dagger a_1 \frac{E_{10}+E_{01}}{2E_{10}E_{01}}\right) - T^2\nu^\dagger\nu\left(a_1 a_2^\dagger \frac{2E_{11}-E_{10}-E_{01}}{2(E_{11}-E_{10})(E_{11}-E_{01})}\right) & E_{01} + T^2\nu\nu^\dagger\left(\frac{a_2^\dagger a_2}{E_{01}}\right) - T^2\nu^\dagger\nu\left(\frac{a_1 a_1^\dagger}{E_{11}-E_{01}}\right) & 0 \\[2ex] \frac{1}{2}T^2\nu^2\left(\frac{(2E_{10}-E_{11})}{E_{10}(E_{11}-E_{10})}a_2^\dagger a_1^\dagger + \frac{(2E_{01}-E_{11})}{E_{01}(E_{11}-E_{01})}a_1^\dagger a_2^\dagger\right) & 0 & 0 & E_{11} - T^2\nu\nu^\dagger\left(\frac{a_2^\dagger a_2}{E_{11}-E_{10}} + \frac{a_1^\dagger a_1}{E_{11}-E_{01}}\right) \end{pmatrix}$$

The transformed Hamiltonian describing the dot subsystem and second order interactions with the reservoir subsystem. Each term describes a cotunneling event.

Figure C.1: The Transformed Hamiltonian

APPENDIX D:
MATHEMATICA CODE

The results presented in Chapter 3.5 are not the product of a single, massive program, but rather a set of smaller programs which evolved over time. Section D.1 contains a program which generates the coefficients in the rate equations, allowing some to depend on time, gate voltage, or even dot charge. Section D.2 contains the module `SolutionCode[]`, which generates the set of state probabilities for a system, sets up the system of coupled differential equations, performs the numerical integration, and returns a list of state probabilities. Finally, Section D.3 uses the list of probabilities found in `SolutionCode[]` to calculate current through each lead.

$$\underline{\text{D.1} \quad \text{Automated Coefficient Matrix Generation}}$$

It was mentioned in Sec. 3.2.2 that the number of coupled differential equations is 2^s, where s is the product of the number of dots, the number of energy levels per dot, and the degeneracy of the system. That being said, the number of coefficients for the set of rate equations is 2^{2s}; even for very simple systems, it is impractical to manually enter the rate equations.

To address this problem, the equations found using Eq. (3.11) can be rewritten as a linear system,

$$\begin{pmatrix} \dot{P}(00...0)(t) \\ \dot{P}(00...1)(t) \\ \vdots \\ \dot{P}(11...1)(t) \end{pmatrix} = \begin{pmatrix} c_{11} & c_{12} & \cdots & c_{1p} \\ c_{21} & c22 & \cdots & c_{2p} \\ \vdots & \vdots & \ddots & \vdots \\ c_{p1} & c_{p2} & \cdots & c_{pp} \end{pmatrix} \begin{pmatrix} P(00...0)(t) \\ P(00...1)(t) \\ \vdots \\ P(11...1)(t) \end{pmatrix}. \tag{D.1}$$

The short program given in this section generates the elements of the coefficient matrix for a specified system size, then writes the matrix to an external, non-executable file. The generated elements are purely symbolic, so that numerical values may be substituted in the appropriate place when called by the module `SolutionCode[]` (see Appendix D.2).

```
ndots = 2;

nlevels = 2;

num = ndots*nlevels;

nstates = 2^num;


(*perm generates a list of the possible combinations of filled and \
unfilled levels.*)


perm = Permutations[Join[Table[0, {num}], Table[1, {num}]], {num}];


(*We use the indices of perm to find total charge and spin for a \
given configuration. Odd slots are spin up, even slots are spin down.*)


up = Table[
   Total[Table[perm[[j, i]], {i, 1, num, 2}]], {j, 1, Length[perm]}];
down = Table[
   Total[Table[perm[[j, i]], {i, 2, num, 2}]], {j, 1, Length[perm]}];
netspin = up - down;
netcharge = up + down;


(*Coeff generates an empty array for the coefficient matrix for the \
rate equations.*)


Coeff = Table[Table[0*i*j, {i, 1, nstates}], {j, 1, nstates}];


tally[i2_, j2_] := Module[{q = i2, p = j2},
  \!\(
\*UnderoverscriptBox[\(\[Sum]\), \(k = 1\), \(num\)]\((1 -
      KroneckerDelta[perm\[LeftDoubleBracket]\(q, k\)\[RightDoubleBracket],
```

```
      perm[\(\[\)\(p, k\)\(]\)]])\)\)]


(*This cell generates the nstates x nstates coefficient matrix, \
Coeff.*)
Do[
 Do[
  m = netcharge[[i]];
  n = netcharge[[j]];
  If[tally[i, j] > 1,
   Coeff[[i, j]] = 0,
   If[i == j,
    Do[
     If[tally[i, l] > 1,
      Coeff[[i, j]] += 0,
      If[i < l,
       Coeff[[i, j]] -= \!\(
\*UnderoverscriptBox[\(\[Sum]\), \(k =
          1\), \(num\)]\((\(\[CapitalGamma][i, l]*f[i, l]*
          KroneckerDelta[perm[\(\[\)\(i, k\)\(]\)],
           0]*\((1 -
            KroneckerDelta[perm[\(\[\)\(i, k\)\(]\)],
             perm[\(\[\)\(l, k\)\(]\)]])\)\) + \[CapitalGamma][i,
           l]*\((1 - f[i, l])\)*
          KroneckerDelta[perm[\(\[\)\(i, k\)\(]\)],
           1]*\((1 -
            KroneckerDelta[perm[\(\[\)\(i, k\)\(]\)],
             perm[\(\[\)\(l, k\)\(]\)]])\))\)\),
       Coeff[[i, j]] -= \!\(
\*UnderoverscriptBox[\(\[Sum]\), \(k =
```
96

```
     1\), \(num\)]\((\[CapitalGamma][i, l]*f[l, i]*

       KroneckerDelta[perm\(\([\)\(i, k\)\(]\)],

         0]*\((1 -

           KroneckerDelta[perm\(\([\)\(i, k\)\(]\)],

            perm\(\([\)\(l, k\)\(]\)]])\) + \[CapitalGamma][i,

          l]*\((1 - f[l, i])\)*

       KroneckerDelta[perm\(\([\)\(i, k\)\(]\)],

         1]*\((1 -

           KroneckerDelta[perm\(\([\)\(i, k\)\(]\)],

            perm\(\([\)\(l, k\)\(]\)]])\)\)\)\)]],

     {l, nstates}],

    If[n - m == 1,

     If[i < j,

      Coeff[[i, j]] = \!\(

\*UnderoverscriptBox[\(\[Sum]\), \(k =

        1\), \(num\)]\((\[CapitalGamma][i,

        j]*\((1 - f[i, j])\)*\((1 -

          KroneckerDelta[perm\(\([\)\(i, k\)\(]\)],

           perm\(\([\)\(j, k\)\(]\)]])\)\)\)\),

      Coeff[[i, j]] = \!\(

\*UnderoverscriptBox[\(\[Sum]\), \(k =

        1\), \(num\)]\((\[CapitalGamma][i,

        j]*\((1 - f[j, i])\)*\((1 -

          KroneckerDelta[perm\(\([\)\(i, k\)\(]\)],

           perm\(\([\)\(j, k\)\(]\)]])\)\)\)\)],

     If[i < j,

      Coeff[[i, j]] = \!\(

\*UnderoverscriptBox[\(\[Sum]\), \(k =

        1\), \(num\)]\((\[CapitalGamma][i, j]*
```

```
        f[i, j]*\((1 -

          KroneckerDelta[perm[\([\)\(i, k\)\(]\)],

            perm[\([\)\(j, k\)\(]\)]])\))\))\)\),

      Coeff[[i, j]] = \!\(

\*UnderoverscriptBox[\(\[Sum]\), \(k =

        1\), \(num\)]\((\(\[CapitalGamma][i, j]*

        f[j, i]*\((1 -

          KroneckerDelta[perm[\([\)\(i, k\)\(]\)],

            perm[\([\)\(j, k\)\(]\)]])\))\))\)\)]]

    ]],

  {j, nstates}],

 {i, nstates}]


file = OpenWrite["/home/sabine/Documents/Dots/mat1.txt"]
Write[file, Coeff]
Close[file]
OutputStream["/home/sabine/Documents/Dots/mat1.txt", 26]
```

D.2   Numerical Integration of the Rate Equations

In Appendix D.1, the code that generates the coefficient matrix for an arbitrarily large QD system was presented. The module below is designed to import the coefficient matrix, substitute the appropriate numerical values for each element, then use the result to generate the set of coupled differential equations obtained using Eq. (3.11). Finally, SolutionCode[] calls Mathematica's NDSolve utility (see Appendix A.2) to generate solutions to the rate equations.

98

```
(*SolutionCode[] solves the rate equations.
 st[] is a list of state probabilities, used as initial conditions.
 vgt is the gate voltage of the top dot.
 vgb is the gate voltage of the bottom dot.
 gra, grb, gla, glb are the gammas for the top (a) or bottom (b) dot,
    on the right (r) or left (l) side.


 NDSolve[] solves the 2^N coupled differential equations for one time
 step (although there are many iterations per step) and returns a list of
 the new state probabilities. The size of the step directly relates to the
 speed of pumping;
 if the interval between values of gate voltage is large,
 the pump speed is large. The new probabilities are appended to a list,
 but also used as the next set of initial conditions.*)


matz = Import[" home sabine Documents Dots mat1.txt"];
   (*Import the coefficient matrix.*)


 SolutionCode[st_, vgt_, vgb_, gra_, grb_, gla_, glb_] :=
 Module[{St = st, Vgt = vgt,
   Vgb = vgb, \[CapitalGamma]ra = gra, \[CapitalGamma]rb =
    grb, \[CapitalGamma]la = gla, \[CapitalGamma]lb = glb},


  (*the module f[i,j] is used
to generate the fermi function for a particular i and j \
in Coeff. It is generalized for two energy levels per dot,
  so define all ea1,2, as the same if nlevels=1. Define a de.*)


  f[i_, j_] := Module[{u = i, v = j},
```

```
slot =
 Flatten[Position[
    Table[1 - KroneckerDelta[perm[[u, k]], perm[[v, k]]], {k, 1,
      num}], 1]][[1]];
U[Nt_, Nb_] = .5*Nt^2*Ect + .5*Nb^2*Ecb +
  Nt*Nb*Ecm - (Cgt*Vgt (Nt*Ect + Nb*Ecm) +
    Cgb*Vgb (Nt*Ecm + Nb*Ecb)) + fv - Nt*Vgt - Nb*Vgb;
fv = .5 Cgt^2*Vgt^2*Ect + .5 Cgb^2*Vgb^2*Ecb +
  Cgt*Vgt*Cgb*Vgb*Ecm;
NA2 = Total[Table[perm[[v, k]], {k, 1, num/2}]];
NB2 = Total[Table[perm[[v, k]], {k, num/2 + 1, num}]];
NA1 = Total[Table[perm[[u, k]], {k, 1, num/2}]];
NB1 = Total[Table[perm[[u, k]], {k, num/2 + 1, num}]];
If[slot < (num/2 + 1),
 (*Transition occurs in dot A*)
 If[slot < (num/4 + 1),
  (*If transition is to the 1st available level*)


  If[appfield,
   (*If there is an applied magnetic field*)


   If[EvenQ[slot],
    energy = \[Epsilon]a1 + d\[Epsilon] + U[NA2, NB2] -
      U[NA1, NB1], (*If slot number for the transition is even,
     it is a spin down electron.*)


    energy = \[Epsilon]a1 - d\[Epsilon] + U[NA2, NB2] -
      U[NA1, NB1]],(*Else,
    if slot number for the transition is odd,
```

```
    it is a spin up electron.*)
   (*Else, there is no field.*)


         energy = \[Epsilon]a1 + U[NA2, NB2] - U[NA1, NB1]],
  (*Else, transition is to level 2 of dot A.*)
  If[appfield,
   (*If there is an applied magnetic field*)


   If[EvenQ[slot],
    energy = \[Epsilon]a2 + d\[Epsilon] + U[NA2, NB2] -
      U[NA1, NB1], (*If slot number for the transition is even,
     it is a spin down electron.*)


    energy = \[Epsilon]a2 - d\[Epsilon] + U[NA2, NB2] -
      U[NA1, NB1]],(*Else,
    if slot number for the transition is odd,
    it is a spin up electron.*)
   (*Else, there is no field.*)


         energy = \[Epsilon]a2 + U[NA2, NB2] - U[NA1, NB1]]],


(*Else, it occurs in dot B*)
If[slot < (3 num/4 + 1),
 (*If transition is to the 1st available level*)


 If[appfield,
  (*If there is an applied magnetic field*)


  If[EvenQ[slot],
```

```
   energy = \[Epsilon]b1 + d\[Epsilon] + U[NA2, NB2] -
     U[NA1, NB1], (*If slot number for the transition is even,
    it is a spin down electron.*)


   energy = \[Epsilon]b1 - d\[Epsilon] + U[NA2, NB2] -
     U[NA1, NB1]],(*Else,
   if slot number for the transition is odd,
   it is a spin up electron.*)
   (*Else, there is no field.*)


        energy = \[Epsilon]b1 + U[NA2, NB2] - U[NA1, NB1]],
  (*Else, transition is to level 2 of dot A.*)
  If[appfield,
   (*If there is an applied magnetic field*)


   If[EvenQ[slot],
    energy = \[Epsilon]b2 + d\[Epsilon] + U[NA2, NB2] -
      U[NA1, NB1], (*If slot number for the transition is even,
     it is a spin down electron.*)


    energy = \[Epsilon]b2 - d\[Epsilon] + U[NA2, NB2] -
      U[NA1, NB1]],(*Else,
   if slot number for the transition is odd,
   it is a spin up electron.*)
   (*Else, there is no field.*)


        energy = \[Epsilon]b2 + U[NA2, NB2] - U[NA1, NB1]]];
1/(Exp[energy/kbT] + 1)];
```

```
(*The module for gamma reads in time-
dependent values from a list and inserts them into the coefficient \
matrix.*)
  \[CapitalGamma][n_, m_] := Module[{nn = n, mm = m},
    (*This module selects the gamma for a four state system.*)


    slot1 = Flatten[
        Position[
          Table[1 - KroneckerDelta[perm[[nn, k]], perm[[mm, k]]], {k, 1,
             num}], 1]][[1]];
    If[slot1 == 1,
      (\[CapitalGamma]la + \[CapitalGamma]ra),
      (\[CapitalGamma]lb + \[CapitalGamma]rb)]];


ProbEq = ToExpression[matz];
SysEq[t_] = {p1[t], p2[t], p3[t], p4[t], p5[t], p6[t], p7[t], p8[t],
    p9[t], p10[t], p11[t], p12[t], p13[t], p14[t], p15[t], p16[t]};
MethSol = MapThread[#1 == #2 &, {SysEq'[t], ProbEq.SysEq[t]}];
Sol = NDSolve[{MethSol, p1[0] == St[[1]], p2[0] == St[[2]],
    p3[0] == St[[3]], p4[0] == St[[4]], p5[0] == St[[5]],
    p6[0] == St[[6]], p7[0] == St[[7]], p8[0] == St[[8]],
    p9[0] == St[[9]], p10[0] == St[[10]], p11[0] == St[[11]],
    p12[0] == St[[12]], p13[0] == St[[13]], p14[0] == St[[14]],
    p15[0] == St[[15]], p16[0] == St[[16]]}, {p1, p2, p3, p4, p5, p6,
     p7, p8, p9, p10, p11, p12, p13, p14, p15, p16}, {t, 0, 10}(*,
   Method->{EventLocator,"Event"->p1[t]-.0001}*)];
{P1, P2, P3, P4, P5, P6, P7, P8, P9, P10, P11, P12, P13, P14, P15,
   P16} = Flatten[{p1[t], p2[t], p3[t], p4[t], p5[t], p6[t], p7[t],
     p8[t], p9[t], p10[t], p11[t], p12[t], p13[t], p14[t], p15[t],
```

```
        p16[t]} /. Sol];
   Block[{t = 1},
    Chop[Evaluate[{P1, P2, P3, P4, P5, P6, P7, P8, P9, P10, P11, P12,
        P13, P14, P15, P16}]]]]
   ]
```

After the probabilities have been generated for a given set of gate voltages, it is relatively
simple to calculate current. The module shown here, `Current[]`, generates expressions for
the current through each node using Eq. (3.19), takes values for gate voltages, tunneling
rates, and a list of state probabilities, and returns values as a list. Like `SolutionCode[]`,
`Current` takes one set of values at a time, so the module must be invoked as many times
as there are voltage steps.

   The output is then used to calculate quantities such as the total current through the
top (or bottom) dot and net spin. Over many cycles, data may be used to find average
per-cycle quantities, such as average total charge and spin transferred per cycle.

```
Current[vga_, vgb_, in_, gammatopl_, gammabottoml_, gammatopr_,
  gammabottomr_] :=
 Module[{vvgt = vga, vvgb = vgb, pr = in, gla = gammatopl,
   glb = gammabottoml, gra = gammatopr, grb = gammabottomr},


  F[pe_, qu_] := Module[{eu = pe, ev = qu},
    sslot =
     Flatten[Position[
        Table[1 - KroneckerDelta[perm[[eu, k]], perm[[ev, k]]], {k, 1,
          num}], 1]][[1]];
```

104

```
UU[Nt_, Nb_] = .5*Nt^2*Ect + .5*Nb^2*Ecb +

  Nt*Nb*Ecm - (Cgt*vvgt (Nt*Ect + Nb*Ecm) +

    Cgb*vvgb (Nt*Ecm + Nb*Ecb)) + Fv - Nt*vvgt - Nb*vvgb;

Fv = .5 Cgt^2*vvgt^2*Ect + .5 Cgb^2*vvgb^2*Ecb +

  Cgt*vvgt*Cgb*vvgb*Ecm;

NA2 = Total[Table[perm[[ev, k]], {k, 1, num/2}]];

NB2 = Total[Table[perm[[ev, k]], {k, num/2 + 1, num}]];

NA1 = Total[Table[perm[[eu, k]], {k, 1, num/2}]];

NB1 = Total[Table[perm[[eu, k]], {k, num/2 + 1, num}]];

If[sslot < (num/2 + 1),

 (*Transition occurs in dot A*)

 If[sslot < (num/4 + 1),

  (*If transition is to the 1st available level*)


  If[appfield,

   (*If there is an applied magnetic field*)


   If[EvenQ[sslot],

    energy = \[Epsilon]a1 + d\[Epsilon] + UU[NA2, NB2] -

      UU[NA1, NB1], (*If slot number for the transition is even,

    it is a spin down electron.*)


    energy = \[Epsilon]a1 - d\[Epsilon] + UU[NA2, NB2] -

      UU[NA1, NB1]],(*Else,

   if slot number for the transition is odd,

   it is a spin up electron.*)

   (*Else, there is no field.*)


        energy = \[Epsilon]a1 + UU[NA2, NB2] - UU[NA1, NB1]],
```

```
 (*Else, transition is to level 2 of dot A.*)
If[appfield,
  (*If there is an applied magnetic field*)


 If[EvenQ[sslot],
  energy = \[Epsilon]a2 + d\[Epsilon] + UU[NA2, NB2] -
    UU[NA1, NB1], (*If slot number for the transition is even,
   it is a spin down electron.*)


  energy = \[Epsilon]a2 - d\[Epsilon] + UU[NA2, NB2] -
    UU[NA1, NB1]],(*Else,
   if slot number for the transition is odd,
   it is a spin up electron.*)
  (*Else, there is no field.*)


       energy = \[Epsilon]a2 + UU[NA2, NB2] - UU[NA1, NB1]]],


(*Else, it occurs in dot B*)
If[sslot < (3 num/4 + 1),
 (*If transition is to the 1st available level*)


 If[appfield,
  (*If there is an applied magnetic field*)


 If[EvenQ[sslot],
  energy = \[Epsilon]b1 + d\[Epsilon] + UU[NA2, NB2] -
    UU[NA1, NB1], (*If slot number for the transition is even,
   it is a spin down electron.*)
```

```
       energy = \[Epsilon]b1 - d\[Epsilon] + UU[NA2, NB2] -
          UU[NA1, NB1]],(*Else,
      if slot number for the transition is odd,
      it is a spin up electron.*)
      (*Else, there is no field.*)


          energy = \[Epsilon]b1 + UU[NA2, NB2] - UU[NA1, NB1]],
     (*Else, transition is to level 2 of dot A.*)
     If[appfield,
      (*If there is an applied magnetic field*)


      If[EvenQ[sslot],
       energy = \[Epsilon]b2 + d\[Epsilon] + UU[NA2, NB2] -
          UU[NA1, NB1], (*If slot number for the transition is even,
       it is a spin down electron.*)


       energy = \[Epsilon]b2 - d\[Epsilon] + UU[NA2, NB2] -
          UU[NA1, NB1]],(*Else,
      if slot number for the transition is odd,
      it is a spin up electron.*)
      (*Else, there is no field.*)


          energy = \[Epsilon]b2 + UU[NA2, NB2] - UU[NA1, NB1]]]];
    1/(Exp[energy/kbT] + 1)];
  cj = {0, 0, 0, 0};
(*This part figures out which states contribute to a specific
 current, and calculates the currents for one time step.*)
  For[i = 1, i < Length[perm] + 1, i++,
   For[j = 1, j < Length[perm] + 1, j++,
```
107

```
      fn = perm[[i]] - perm[[j]];
      For[k = 1, k < 5, k++,
       If[Total[Abs[fn]] == 1,
        If[fn[[k]] == 1,
         cj[[k]] += F[j, i]*pr[[j]],
         If[fn[[k]] == -1,
          cj[[k]] += (1 - F[i, j])*pr[[j]]]]]]]];
{gla*cj[[1]], gla*cj[[2]], gra*cj[[1]], grb*cj[[2]], glb*cj[[3]],
 glb*cj[[4]], grb*cj[[3]], grb*cj[[4]]}
]
```

REFERENCES

[1] M. Lundstrom, "Moore's Law Forever?," *Science*, vol. 299, no. 5604, pp. 210-211, Jan. 2003.

[2] S. A. Wolf *et al.*, "Spintronics: A Spin-Based Electronics Vision for the Future," *Science*, vol. 294, no. 5546, pp. 1488-1495, Nov. 2001.

[3] I. Zutic *et al.*, "Spintronics: Fundamentals and applications," *Rev. Mod. Phys.*, vol. 76, no. 2, pp. 323-410, 2004.

[4] D. Awschalomi and M. Flatté, "Challenges for semiconductor spintronics," *Nature Physics*, vol. 3, pp. 153-159, 2007.

[5] Q. Sun and X. C. Xie, "Spontaneous spin-polarized current in a nonuniform Rashba interaction system," *Phys. Rev. B*, vol. 71, no. 15, pp. 155321-155327, 2005.

[6] G. Schmidt *et al.*, "Fundamental obstacle for electrical spin injection from a ferromagnetic metal into a diffusive semiconductor," *Phys. Rev. B*, vol. 62, no. 8, pp. R4790-R4793, 2000.

[7] O. M. J. van 't Erve *et al.*, "Information Processing with Pure Spin Currents in Silicon: Spin Injection, Extraction, Manipulation and Detection," *IEEE Trans. Electron Devices*, vol. 56, no. 10, pp. 2343-2347, Oct. 2009.

[8] K. C. Hall, M. E. Flatté, "Performance of a spin-based insulated gate field effect transistor," *Appl. Phys. Lett.*, vol. 88, no. 16, pp. 162503-162506, 2006.

[9] S. Sanvito, "Filtering spins with molecules," *Nature Materials*, vol. 10, pp. 484-485, Jun. 2011.

[10] W. Gong *et al.*, "Tunable pure spin currents in a triple-quantum-dot ring," *Appl. Phys. Lett.*, vol. 92, no. 4, pp. 042104-042107, 2008.

[11] J. Peng and Z. Chen, "A single molecule spin pump," *Phys. Lett. A*, vol. 365, no. 56, pp. 505-509, Jun 2007.

[12] S. Cho *et al.*, "Gate-tunable graphene spin valve," *Appl. Phys. Lett.*, vol. 91, no. 12, pp. 123105-123108, 2007.

[13] B. Braunecker *et al.*, "Spin current and rectification in one-dimensional electronic systems," *Phys. Rev. B*, vol. 76, no. 8, pp. 085119-085130, 2007.

[14] P. Zhang *et al.*, "Spin Current through a Quantum Dot in the Presence of an Oscillating Magnetic Field," *Phys. Rev. Lett.*, vol. 91, no. 19, pp. 196602-196606, 2003.

[15] M. Busl and G. Platero, "Spin-polarized currents in double and triple quantum dots driven by ac magnetic fields," *Phys. Rev. B*, vol. 82, no. 20, pp. 205304-205311, 2010.

[16] D. J. Thouless, "Quantization of particle transport," *Phys. Rev. B*, vol. 27, no. 10, pp.6083-6087, 1983.

[17] L. P. Kouwenhoven *et al.*, "Photon-assisted tunneling through a quantum dot," *Phys. Rev. B*, vol. 50, no. 3, pp. 2019-2022, 1994.

[18] L. P. Kouwenhoven *et al.*, "Observation of photon-assisted tunneling through a quantum dot," *Phys. Rev. Lett.*, vol. 73, no. 25, pp. 3443-3446, 1994.

[19] B. L. Hazelzet *et al.*, "Coherent and incoherent pumping of electrons in double quantum dots," *Phys. Rev. B*, vol. 63, no. 16, pp. 165313-165323, 2001.

[20] M. Braun and G. Burkard, "Non-adiabatic two-parameter charge and spin pumping in a quantum dot," *Phys. Rev. Lett.*, vol. 101, no. 3, pp. 036802-036806, 2008.

[21] P. Sharma and P. W. Brouwer, "Mesoscopic effects in adiabatic spin pumping," *Phys. Rev. Lett.*, vol. 91, no. 16, pp. 166801, Oct. 2003.

[22] E. R. Mucciolo *et al.*, "Adiabatic Quantum Pump of Spin-Polarized Current," *Phys. Rev. Lett.*, vol. 89, no. 14, pp. 146802-146806, 2002.

[23] T. Aono, "Adiabatic spin pumping through a quantum dot with a single orbital level," *Phys. Rev. B*, vol. 67, no. 15, pp. 155303-155307, 2003.

[24] E. Cota *et al.*, "AC-driven double quantum dots as spin pumps and spin filters," *Phys. Rev. Lett.*, vol. 94, no. 10, pp. 107202-107206, 2005.

[25] B. Dong *et al.*, "Pumped spin-current and shot noise spectra in a single quantum dot," *Phys. Rev. Lett.*, vol. 94, no. 6, pp. 066601-066606, 2005.

[26] L. Fu and C. L. Kane, "Time Reversal Polarization and a Z_2 Adiabatic Spin Pump," *Phys. Rev. B*, vol. 74, no. 19, pp. 195312-195325, 2006.

[27] S. M. Frolov *et al.*, "Electrical generation of pure spin currents in a two-dimensional electron gas," *Phys. Rev. Lett.*, vol. 102, no. 11, pp. 116802-116806, 2009.

[28] R. Sánchez *et al.*, "Spin filtering through excited states in double quantum dot pumps," *Phys. Rev. B*, vol. 74, no. 3, pp. 035326-035334, 2006.

[29] R. D. R. Bhat and J. E. Sipe, "Optically Injected Spin Currents in Semiconductors," *Phys. Rev. Lett.*, vol. 85, no. 25, pp. 5432-5435, 2000.

[30] S. Ju *et al.*, "Electrically controllable spin filtering and switching in multiferroic tunneling junctions," *Phys. Rev. B*, vol. 75, no. 6, pp. 064419-064424, 2007.

[31] A. Fert and H. Jaffrès ,"Conditions for efficient spin injection from a ferromagnetic metal into a semiconductor," *Phys. Rev. B*, vol. 64, no. 18, pp. 184420-184429, 2001.

[32] J. E. Hirsch, "Spin Hall Effect," *Phys. Rev. Lett.*, vol. 83, no. 9, pp. 1834-1837, 1999.

[33] V. Sih *et al.*, "Generating Spin Currents in Semiconductors with the Spin Hall Effect," *Phys. Rev. Lett.*, vol. 97, no. 9, pp. 096605-096609, 2006.

[34] E. Saitoh *et al.*, "Conversion of spin current into charge current at room temperature: Inverse spin-Hall effect," *Appl. Phys. Lett.*, vol. 88, no. 18, pp. 182509-182512, 2006.

[35] D. Culcer *et al.*, "Semiclassical Spin Transport in Spin-Orbit-Coupled Bands," *Phys. Rev. Lett.*, vol. 93, no. 4, pp. 046602-046606, 2004.

[36] J. Shi *et al.*, "Proper Definition of Spin Current in Spin-Orbit Coupled Systems," *Phys. Rev. Lett.*, vol. 96, no. 7, pp. 076604-076608, 2006.

[37] B. K. Nikolić *et al.*, "Spin currents in semiconductor nanostructures: A nonequilibrium Green-function approach," in *The Oxford Handbook on Nanoscience and Technology: Frontiers and Advances*, vol. 1, A. V. Narlikar and Y. Y. Fu, Eds. Oxford: Oxford University Press, 2010, pp. 814-866.

[38] M. A. Kastner, "Artificial Atoms," *Physics Today*, vol. 46, no. 1, pp. 24-31, 1993.

[39] W. G. van der Wiel *et al.*, "Electron transport through double quantum dots," *Rev. Mod. Phys.*, vol. 75, no. 1, pp. 1-22, 2002.

[40] I. H. Chan *et al.*, "Few-electron double quantum dots," *Nanotech.*, vol. 15, no. 5, p. 609, 2004.

[41] K. A. Matveev *et al.*, "Coulomb blockade of tunneling through a double quantum dot," *Phys. Rev. B*, vol. 54, no. 8, pp. 5637-5646, 1996.

[42] U. Hartmann and F. K. Wilhelm, "Decoherence of Charge States in Double Quantum Dots Due to Cotunneling," *Phys. Stat. Solidi (b)*, vol. 233, no. 3, pp. 385-390, Oct. 2002.

[43] T. Hayashi *et al.*, "Coherent Manipulation of Electronic States in a Double Quantum Dot," *Phys. Rev. Lett.*, vol. 91, no. 22, pp. 226804-226808, 2003.

[44] F. Mireles *et al.*, "Spin Filter Effect in a Parallel Double Quantum Dot," *J. Supercond.: Incorporating Novel Magnetism*, vol. 18, no. 2, pp. 233-239, 2005.

[45] A. S. Adourian *et al.*, "Evolution of Coulomb blockade spectra in parallel coupled quantum dots," *Appl. Phys. Lett.*, vol. 75, no. 3, pp. 424-427, 1999.

[46] L. P. Kouwenhoven *et al.*, "Electron Transport in Quantum Dots. Nato ASI conference proceedings, Ed. L. P. Kouwenhoven, G. Schön, and L. L. Sohn (Kluwer, Dordrecht, 1997), pp. 105-214.

[47] I. L. Aleiner *et al.*, "Quantum effects in Coulomb blockade," *Phys. Rep.*, vol. 358, no. 5-6, pp. 309-440, Mar. 2002.

[48] C. W. J. Beenakker, "Theory of Coulomb-blockade oscillations in the conductance of a quantum dot," *Phys. Rev. B*, vol. 44, no. 4, pp. 1646-1656, 1991.

[49] *Single Charge Tunneling: Coulomb Blockade Phenomena in Nanostructures*, H. Grabert and M. H. Devoret, Eds. New York, NY: Plenum Press, 1992.

[50] R. C. Ashoori *et al.*, "N-Electron Ground State Energies of a Quantum Dot in Magnetic Field," *Phys. Rev. Lett.*, vol. 71, no. 4, pp. 613-616, 1993.

[51] O. Klein *et al.*, "Exchange Effects in an Artificial Atom at High Magnetic Fields," *Phys. Rev. Lett.*, vol. 74, no. 5, pp. 785-788, 1995.

[52] P. L. McEuen *et al.*, "Transport Spectroscopy of a Coulomb Island in the Quantum Hall Regime," *Phys. Rev. Lett.*, vol. 66, no. 14, pp. 1926-1929, 1991.

[53] M. Pustilnik *et al.*, "Magnetic field-induced Kondo effects in Coulomb blockade systems," *Lecture Notes in Physics*, vol. 579, 2001.

[54] M. Pustilnik and L. I. Glazman, "Low-Temperature Conduction of a Quantum Dot," in *Quantum Dots: A Doorway to Nanoscale Physics*, W. D. Heiss, Ed. Berlin / Heidelberg: Springer, 2005.

[55] H. Jeong *et al.*, "The Kondo Effect in an Artificial Quantum Dot Molecule," *Science*, vol. 21, pp. 2221-2223, Sep. 2001.

[56] S. Datta, *Electronic Transport in Mesoscopic Systems.* Cambridge: Cambridge University Press, 1995.

[57] A. Fuhrer *et al.*, "Transport properties of quantum dots with steep walls," *Phys. Rev. B*, vol. 63, no. 12, pp. 125309-125317, 2001.

[58] S. Tarucha *et al.*, "Shell Filling and Spin Effects in a Few Electron Quantum Dot," *Phys. Rev. Lett.*, vol. 77, no. 17, pp. 3613-3616, 1996.

[59] D. S. Duncan *et al.*, "Coulomb blockade spectroscopy on a small quantum dot in a parallel magnetic field," *Appl. Phys. Lett.*, vol. 77, no. 14, pp. 2183-2186, 2000.

[60] B. I. Halperin *et al.*, "Spin-Orbit Effects in a GaAs Quantum Dot in a Parallel Magnetic Field," *Phys. Rev. Lett.*, vol. 86, no. 10, pp. 2106-2109, 2001.

[61] A. P. Jauho *et al.*, "Time-dependent transport in interacting and non-interacting resonant-tunneling systems," *Phys. Rev. B*, vol. 50, no. 8, pp. 5528-5544, 1994.

[62] D. V. Averin *et al.*, "Theory of single-electron charging of quantum wells and dots," *Phys. Rev. B*, vol. 44, no. 12, pp. 6199-6211, 1991.

[63] S. A. Gurvitz and Y. S. Prager, "Microscopic derivation of rate equations for quantum transport," *Phys. Rev. B*, vol. 53, no. 23, pp. 15932-15943, 1996.

[64] U. Harbola *et al.*, "Quantum master equation for electron transport through quantum dots and single molecules," *Phys. Rev. B*, vol. 74, no. 23, pp. 235309-235322, 2006.

[65] M. H. Devoret *et al.*, "Course 11: Single electron phenomena in metallic nanostructures", in *Les Houches Session LXI*, E. Akkermans, G. Montambaux, J.-L. Pichard, and J. Zinn-Justin, Eds. Amsterdam: Elsevier, 1994.

[66] Y. Meir and N. S. Wingreen, "Landauer Formula for the Current through an Interacting Electron Region," *Phys. Rev. Lett.*, vol. 68, no. 16, pp. 2512-2515, 1992.

[67] T. Fujisawa *et al.*, "Electrical pulse measurement, inelastic relaxation, and non-equilibrium transport in a quantum dot," *J. Phys.: Cond. Matt.*, vol. 15, no. 33, p. R1395, 2003.

[68] C. I. Duruöz *et al.*, "Conduction Threshold, Switching, and Hysteresis in Quantum Dot Arrays," *Phys. Rev. Lett.*, vol. 74, no. 16, pp. 3237-3240, 1995.

[69] A. D. Greentree *et al.*, "Coherent electronic transfer in quantum dot systems using adiabatic passage," *Phys. Rev. B*, vol. 70, no. 23, pp. 235317-235323, 2004.

[70] A. R. Hernandez *et al.*, "Adiabatic Charge Pumping through Quantum Dots in the Coulomb Blockade Regime," *Phys. Rev. B*, vol. 80, no. 11, pp. 115311-115321, 2009.

[71] E. R. Mucciolo and C. H. Lewenkopf, "Spin pumping with quantum dots," *Int. J. Nanotech.*, vol. 4, pp. 482-495, 2007.

[72] S. K. Watson *et al.*, "Experimental Realization of a Quantum Spin Pump," *Phys. Rev. Lett.*, vol. 91, no. 25, pp. 258301-258305, 2003.

[73] F. Zhou *et al.*, "Mesoscopic Mechanism of Adiabatic Charge Transport," *Phys. Rev. Lett.*, vol. 82, no. 3, pp. 608-611, 1999.

[74] M. Switkes *et al.*, "An Adiabatic Quantum Electron Pump," *Science*, vol. 283, no. 5409, pp. 1905-1908, Mar. 1999.

[75] F. H. L. Koppens *et al.*, "Driven coherent oscillations of a single electron spin in a quantum dot," *Nature*, vol. 442, pp. 766-771, Aug. 2006.

[76] J. R. Petta *et al.*, "Coherent Manipulation of Coupled Electron Spins in Semiconductor Quantum Dots," *Science*, vol. 309, no. 5744, pp. 2180-2184, Sep. 2005.

[77] T. Fujisawa *et al.*, "Time-dependent single-electron transport through quantum dots," *Rep. Prog. Phys.*, vol. 69, no. 3, pp. 759-796, 2006.

[78] I. L. Aleiner and A. V. Andreev, "Adiabatic Charge Pumping in Almost Open Dots," *Phys. Rev. Lett.*, vol. 81, no. 6, pp. 1286-1289, 1998.

[79] T. A. Shutenko *et al.*, "Mesoscopic Fluctuations of Adiabatic Charge Pumping in Quantum Dots," *Phys. Rev. B*, vol. 61, no. 15, pp. 10366-10375, 2000.

[80] I. Amlani *et al.*, "Demonstration of a six-dot quantum cellular automata system," *Appl. Phys. Lett.*, vol. 72, no. 17, pp. 2179-2181,

[81] C. S. Lent *et al.*, "Bistable saturation in coupled quantum dots for quantum cellular automata," *Appl. Phys. Lett.*, vol. 62, no. 7, pp. 714-716, Feb. 1993.

[82] J. Timler and C. S. Lent, "Maxwell's demon and quantum-dot cellular automata," *J. Appl. Phys.*, vol. 94, no. 2, pp. 1050-1061, 2003.

[83] R. K. Kummamuru *et al.*, "Operation of a Quantum-Dot Cellular Automata (QCA) Shift Register and Analysis of Errors," *IEEE Trans. Electron Devices*, vol. 50, no. 9, pp. 1906-1913, Sep. 2003.

[84] C. López-Monís *et al.*, "Dynamical nuclear spin polarization induced by electronic current through double quantum dots," *New J. Phys.*, vol. 13, p. 053010, May 2011.

[85] M. Blaauboer and C. M. L. Fricot, "A spin pump turnstile: parametric pumping of a spin-polarized current through a nearly-closed quantum dot," *Phys. Rev. B*, vol. 71, no. 4, pp. 041303(R)-041307(R), 2005.

[86] M. M. Mahmoodian and M. V. Entin, "Theory of one-dimensional double-barrier quantum pump in two-frequency signal regime," *Europhys. Lett.*, vol. 77, no. 6, pp. 67002, 2007.

[87] C. Beenakker and C. Schönenberger, "Quantum Shot Noise," *Physics Today*, vol. 56, no. 5, pp. 37-42, May 2003.

[88] B. Hiltscher *et al.*, "Interference and interaction effects in adiabatic pumping through quantum dots," *Phys. Rev. B*, vol. 81, no. 8, pp. 085302-085311, 2010.

[89] M. L. Polianski *et al.*, "Noise through quantum pumps," *Phys. Rev. B*, vol. 65, no. 24, pp. 245314-245323, 2002.

[90] R. Hanson *et al.*, "Spins in few-electron quantum dots," *Rev. Mod. Phys.*, vol. 79, no. 4, pp. 1217-1265, 2007.

[91] A. Andreev and A. Kamenev, "Counting Statistics of an Adiabatic Pump," *Phys. Rev. Lett.*, vol. 85, no. 6, pp. 1294-1297, 2000.

[92] G. Kießlich *et al.*, "Shot noise of coupled semiconductor quantum dots," *Phys. Rev. B*, vol. 68, no. 12, pp. 125320-125328, 2003.

[93] A. Thielmann *et al.*, "Shot noise in tunneling transport through molecules and quantum dots," *Phys. Rev. B*, vol.68, no. 11, pp. 115105-115112, 2003.

[94] A. Thielmann *et al.*, "Super-Poissonian noise, negative differential conductance, and relaxation effects in transport through molecules, quantum dots, and nanotubes," *Phys. Rev. B*, vol. 71, no. 4, pp. 045341-045349, 2005.

[95] O. Entin-Wohlman and A. Aharony, "Quantized adiabatic charge pumping and resonant transmission," *Phys. Rev. B*, vol. 66, no. 3, pp. 035329-035335, 2002.

[96] Y. Levinson *et al.*, "Pumping at resonant transmission and transferred charge quantization," *Physica A: Stat. Mech. Applicat.*, vol. 302, no. 1-4, pp. 335-344, Dec. 2001.

[97] O. Entin-Wohlman *et al.*, "Adiabatic transport in nanostructures," *Phys. Rev. B*, vol. 65, no. 19, pp. 195411-195419, 2002.

[98] M. G. Vavilov and V. Ambegaokar, "Charge pumping and photovoltaic effect in open quantum dots," *Phys. Rev. B*, vol. 63, no. 19, pp. 195313-195325, 2001.

[99] Y. Wei *et al.*, "Resonance-assisted parametric electron pump," *Phys. Rev. B*, vol. 62, no. 15, pp. 9947-9950, 2000.

[100] A. Fubini *et al.*, "Robustness of adiabatic passage through a quantum phase transition," *New J. Phys.*, vol. 9, p. 134, May 2007.

[101] E. W. Weisstein. *Adams' Method* [Online]. Available: http://mathworld.wolfram.com/AdamsMethod.html

[102] W. H. Press *et al.*, *Numerical Recipes in C: The Art of Scientific Computing*, 2nd ed. New York, NY: Cambridge University Press, 1992.